RICE UNIVERSITY

Catalytic processes simulated at nano-scale: Growth of graphitic structures and functionalized graphene explained

by

Morgana de Avila Ribas

A Thesis Submitted
in Partial Fulfillment of the
Requirements for the Degree

Doctor of Philosophy

Approved, Thesis Committee:

Boris I. Yakobson, Chair
Professor of Mechanical and Materials
Science Engineering, and Chemistry

Robert Vajtai
Faculty Fellow of Mechanical and
Materials Science Engineering

Anatoly B. Kolomeisky
Associate Professor of Chemistry, and
Chemical and Biomolecular Engineering

Houston, Texas

March, 2011

ABSTRACT

Catalytic processes simulated at nano-scale: Growth of graphitic structures and functionalized graphene explained

by

Morgana de Avila Ribas

Key dynamic processes at nano-scale, such as graphene hydrogenation and fluorination, and carbon nanotube (CNT) growth, cannot be observed *in situ* in real time. Nevertheless, such processes can be studied through complementary computational methods. This work simulates three important catalytic processes representing the growth of graphitic structures and functionalized graphene. The spillover phenomenon, which has been considered promising for efficient hydrogen storage, includes transfer of H from a metal catalyst to a graphitic receptor, to finally form a graphane island. Although, the spillover is energetically unfavorable to occur on pristine graphene, catalyst saturation provides a way for hydrogen adsorption on the receptor. *Ab initio* calculations show that the H chemical potential can be increased to a spillover favorable range. Unlike in graphane, upon graphene fluorination different stoichiometric phases form without a nucleation barrier, with the complete CF phase being thermodynamically most stable. After fluorination, graphene electronic properties are transformed from metallic to semiconducting. First-principles and tight-binding methods are used to investigate the patterning of nanoroads and quantum dots on these phases, combining metallic and semiconducting properties on the same sheet. In catalyzed CNT growth the metallic catalyst plays a funda-

mental role in cap nucleation. Such a mechanism cannot be seen in experiment, nor can it be simulated by first-principles due to its time-scale, yet it can be simulated through molecular dynamics. Tuning the metal-C interaction controls the condition for growth or encapsulation: Surface carbon-diffusion limits the growth below 600 K, and at higher temperatures they depend on cap lift-off. Such tuning can be done through catalyst alloying, as shown through *ab initio* simulations for Ni-Fe and Cu-Fe bimetallic catalysts. Catalyst shape also plays an important role in CNT growth. The minimization of the Ni surface energy defines the equilibrium crystal shape. Catalyst reshaping is analyzed through C adsorption by first-principles and reactive force fields. The Wulff-construction suggests a significant reduction of the surface energy anisotropy upon C adsorption, based on which a continuum phenomenological model that considers catalyst reshaping in CNT nucleation is formulated. This thesis explains the growth of graphitic structures and functionalized graphene at nano-scale through computational simulations.

Acknowledgments

My sincere thanks to my supervisor Dr. Boris I. Yakobson. I am indebted and grateful for having his constant guidance, invaluable suggestions, and continuous support. I am uttermost thankful for his understanding and accommodation of my family obligations. I would like also to thank very much the thesis committee members, Dr. Robert Vajtai and Dr. Anatoly B. Kolomeisky, for spending their precious time reading this work and participating in its discussion, with valuable suggestions and comments.

I would like to thank my collaborators Dr. Abhishek K. Singh, Dr. Feng Ding, Dr. Evgeni S. Penev, Dr. Enrique Munõz, Dr. Pavel B. Sorokin, Dr. Perla B. Balbuena, Dr. Avetik R. Harutyunyan, Dr. Elena Pigos, Dr. Renu Sharma, Dr. Salomeh Tabatabaei, Dr. Ashavani Kumar, Dr. Pulickel M. Ajayan, and Ksenia Bets. Their contribution, invaluable comments and suggestions, and fruitful discussions helped to make this thesis a reality.

Thanks to all past and present group members of our lab, Dr. Kun Jiao, Dr. Yu Lin, Dr. Arta Sadrzadeh, Dr. Zhiping Xu, Dr. Vasilii Artyukhov, Dr. Alexander Dobrinsky, Dr. Somnath Bhowmick, Dr. Ke Zhao, Dr. Hoonkyung Lee, Ming Hua, Morteza Bankehsaz, Yuanyue Liu, Jianxin Lu, Fangbo Xu, Ming Luo, and Mingjie Liu. It was great to count on your support through out these years. I will miss our group meetings!

My sincere thanks to the faculty and staff of the Department of Mechanical and Materials Science Engineering, specially to Judith Farhat, Aya Ossowski, and Sherry Vanderslice. A big hug to Maria Maldonado! I am also grateful for the continuous support from the Research Computing Support, Office of International Students and

Scholars, and Dr. Jan Hewitt, among others, at Rice University. The computations showed in this work were performed at the Shared Computing Resources at Rice University and through allocation TG-DMR100029 on Kraken, at the National Institute for Computational Sciences, and are gratefully acknowledged.

I would like to express my sincere thanks to the Roberto Rocca Educational Program and their sponsors, Tenaris, Ternium and Techint, for their generous financial support. Many thanks to the RREP director, Mr. Daniel Krishock, and staff. It was very important and a great personal and professional experience to participate in such pioneer program.

Without the continuous support and comprehension of my family I could not have done the work shown here. Thank you so much Aashka, Anusha, and Abhishek! A special thanks to my in-laws Meena and Anand, for their support when I needed the most. I could not forget to thank my parents, Maria Celina and Vilson, long gone but never forgotten.

Contents

Illustrations

Tables

Chapter 1

Introduction

1.1 Thesis outline and motivation

Key dynamic processes at nano-scale, such as graphene hydrogenation and fluorination, and carbon nanotube (CNT) growth, cannot be observed *in situ* in real time. Nevertheless, such processes can be studied through complementary computational methods. This work simulates three important catalytic processes representing the growth of graphitic structures and functionalized graphene.

This first chapter offers an overview on graphitic materials and hydrogen storage via spillover, graphene fluorination, and catalytic CNT growth at nano-scale. Whereas some processes are suitable to be studied at a reduced scale, as is the case of hydrogen spillover, others, as patterning of fluorinated graphene, require the use of multi-scale methods. The complexity of the phenomenon to be investigated may require combining different computational methods, as in CNT growth. Chapter 2 conveys the necessary theoretical background on the different computational methods and models used here.

The spillover phenomenon has been considered promising for efficient hydrogen storage. It essentially involves transfer of H from a metal catalyst to a graphitic receptor, to finally form a graphane island. An open question about spillover mechanism is how an H atom binds to graphene instead of forming the thermodynamically preferred H_2. Using *ab initio* calculations, it is shown in chapter 3 that the catalyst

saturation provides a way for adsorption of hydrogen on the receptor by increasing the hydrogen chemical potential to a spillover favorable range [1]. Although the spillover is energetically unfavorable to occur on a pristine graphene surface, the presence of a phase of hydrogenated graphene facilitates the spillover by significantly improving the C-H binding. Hence, thermodynamically spillover can occur, both from the free standing and from the receptor supported clusters. Further, the computed energy barrier of the motion of an H from the catalyst to the hydrogenated graphene is small (0.68 eV) and can be overcome at operational temperatures.

Like graphane phase, which is formed after hydrogen chemisorption, the sp^3 fluorinated graphene phase is semiconducting. Through patterning of the chemically functionalized graphene, both semiconducting and metallic elements can be combined on the same graphene sheet for use in electronic applications. *Ab initio* methods are used to investigate the fluorination of graphene, chapter 4. Unlike in graphane, upon graphene fluorination, different stoichiometric phases form without a nucleation barrier, with the complete "2D-Teflon" CF phase being thermodynamically most stable [2]. As the fluorinated graphene is an insulator, it turns out to be a perfect matrix-host for patterning nanoroads and quantum dots of pristine graphene. The electronic and magnetic properties of the nanoroads can be tuned by varying the edge orientation and width of the CF [3]. Tight-binding methods are used to explore large edge-specific quantum dots. The energy gaps between the highest occupied and lowest unoccupied molecular orbitals (HOMO–LUMO) of quantum dots are size-dependent and show a confinement typical of Dirac fermions. Furthermore, the effect of different basic coverage of F on graphene (with stoichiometries CF and C_4F) on the band gaps is studied, revealing the suitability of these materials to host quantum dots of graphene with unique electronic properties [2].

In catalyzed CNT growth the metallic catalyst plays a fundamental role in the cap nucleation, additional to acting in the feedstock decomposition and providing adequate support for the tube. However, the factors and forces, which decide if the gathering sp^2-network of atoms will adhere to the catalyst particle and fully cover it, or the graphitic cap will liberate itself to extend into a hollow filament, remain a challenge for theory. Indeed, such a mechanism cannot be seen in experiment, nor can it be simulated by first-principles due to its time-scale, yet it can be simulated through comprehensive molecular dynamics. In chapter 5, the adhesion strength (W_{ad}) of the graphitic cap to the catalyst and temperature T (and C diffusion rate) are systematically varied. A statistically representative map of CNT nucleation is build through observations, making possible to define the conditions for growth or metal encapsulation in a fullerene-shell (catalyst poisoning) [4]. It shows clearly that weak W_{ad}, sufficient thermal kinetic energy (high T), or fast C diffusion favors the CNT nucleation. In particular, below 600 K carbon-diffusion on the catalyst surface limits the growth, but at higher T it fully depends on cap lift-off. An informed choice of parameters allows the obtention of the longest simulated nanotube structures. In this way, a means of designing the catalyst for better CNT synthesis, potentially at desirably low temperatures, is revealed.

The catalyst type and shape have an important role during CNT growth, chapter 6: (i) Controllable catalytic CNT growth can be achieved by precisely tuning metal catalyst properties through alloying and (ii) CNT cap nucleation mechanism originates from catalyst reshaping. Bimetallic nanocatalysts are obtained by alloying different metals at nano-scale, resulting into synergistic effects and new desirable properties [5]. M_xFe_y nanocatalysts, where M = Ni and Cu, $x = 0.23$ and 0.77, and $y = 1 - x$, are analyzed here through *ab initio* calculations to investigate the use of

catalyst-tube work of adhesion for chirality selective CNT growth. Among the pristine metals analyzed, Fe has the strongest binding energy to either armchair (AC) or zigzag (ZZ) CNT, followed by Ni and Cu. The binding energy of Ni_xFe_y to the CNT is chirality selective (AC or ZZ), whereas the catalyst-CNT binding can be fine tuned through the inverse relation between E_b and Cu atomic fraction for Cu_xFe_y. Molecular dynamics simulations provide a good qualitative picture of the CNT growth, including catalyst reshaping and incipient double-wall formation. However, after the C atoms start depositing on the catalyst, the different facets are indistinguishable. One way to overcome this limitation is to model the deposition of C on each of its individual surfaces. The surface relaxation and energy of low-index {111}, {100}, and {110}, and high-index {211}, {210}, {311}, and {320} Ni surfaces are studied by first-principles for various slab thicknesses [6]. Although the low-index surface properties converge for slabs $>$ 6 Å, the high-index surfaces require slabs $>$ 12 Å. The Ni(111) has the lowest surface energy, being also the dominant facet on the resulting Ni equilibrium crystal shape. Other visible facets are (100), (110), (210), and (311). The effect of C adsorption on these same facets is studied by first-principles and a reactive force field. The resulting equilibrium crystal shape suggests a significant reduction of the surface energy anisotropy. Based on such evidence, a continuum phenomenological model describing the effect of the catalyst reshaping upon C adsorption is formulated [7]. It is suggested that the CNT growth follows an oscillatory mechanism: (1) After lift-off the metal catalyst retracts from within the cap, which is followed by elongation of the tube (2). The cycle starts over as a new cap nucleates inside the previous tube (3). Thus, (1)$\rightarrow$ (2) $\rightarrow$ (3) $\rightarrow$ (2)$\cdots$(3) progress until the catalyst becomes inactive.

1.2 Introduction

Due to the large pool of methods to choose from, the selection of an adequate theoretical method to solve a specific problem in materials science may seem a daunting task at first. However, instead of competing with each other, these methods can actually be seen as complementary. The scale of the problem to be modeled, the computational effort involved, and the necessary precision of the results have all to be taken into account in order to provide the most efficient solution. At nano-scale, the problem being modeled invariably involves atomic and molecular properties. Such properties are related to the motion and interactions of electrons and nuclei, which, in turn, can be simplified to a higher or lesser degree.

Semi-empirical methods are based on experimental parameters to represent the properties of the materials and, in general, are computationally less demanding. However, given the difficulties to measure the properties of nanomaterials, most of the parameters refer to the properties of bulk materials. Thus, *ab inito* methods are fundamental to study the basic properties of nanomaterials. The relevant theoretical background behind the computational methods used in this work is discussed next.

1.3 Graphitic materials at nano-scale

Until the discovery of the C_{60} (or Buckminsterfullerene) by a team of researchers of Rice University in collaboration with Kroto in 1985 [8], there were only three known allotropic forms of carbon: graphite, diamond, and amorphous carbon. The discovery of the C_{60} and the subsequent ever increasing interest on graphitic materials at nano-scale brought up the start of a new era of scientific and technological discoveries and possibilities. The family of synthetic carbon allotropes (Fig. 1.1) has quickly grown to

include carbon nanotubes (CNT) and graphene, and current research indicates that more may follow [9].

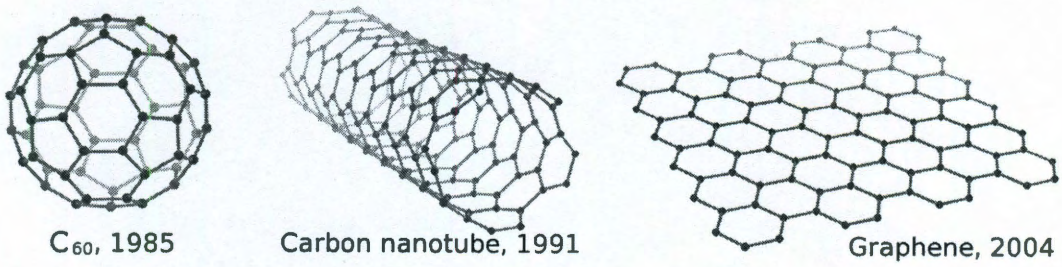

Figure 1.1 : Timeline and schematic structure of synthetic carbon allotropes.

1.3.1 Buckminsterfullerene

The suggested structure of the C_{60} molecule consisted of a truncated icosahedral with 60 equivalent vertices and 32 faces, where a C atom is positioned at each vertex, forming 12 pentagons and 20 hexagonal faces, satisfying the sp^2 valences [8]. This also satisfies Euler's theorem for polyhedra, $f + v = e + 2$, where f, v, and e are the number of faces, vertices, and edges, respectively. In fact, the Buckminsterfullerene structure of the synthesized C_{60} was later confirmed by infrared spectra and X-ray diffraction [10]. Other C_n cage molecules, each composed of 12 pentagons and h hexagons, can also be easily derived, their degree of stability being directly related with the presence of strain-related instabilities due to fused pentagons [11]. The next highly stable cage molecule after the C_{60} is the C_{70}, which also follow the isolated pentagon rule.

1.3.2 Carbon nanotubes

The one-dimensional tubular structure of the carbon nanotubes (CNT) were identified for the first time by Iijima, in 1991 [12]. In fact, one could argue that CNTs were part of the fullerene family as a the smallest CNT cap has at least six pentagons and ten hexagonal faces, i.e., half a C_{60}, being elongated by additional hexagons in an helical arrangement. The unfolding of a CNT into a two-dimensional graphene sheet shows a set of characteristic parameters that are directly related with their fundamental properties. The rolling of this sheet into a tube, Fig. 1.2(a), shows that a chiral vector C_h specifies the tube diameter. The C_h is specified by the basis vectors $\mathbf{a}_1$ and $\mathbf{a}_2$ of the graphene sheet, along $\mathbf{a}_1$ and $\mathbf{a}_2$, and a set of (n, m) integers, so $C_h = n\mathbf{a}_1 + m\mathbf{a}_2 \equiv (n, m)$. The set of (n, m) integers results in a specific tube diameter d and chiral angle θ, where $0 \leq |m| \leq |n|$. For armchair and zigzag tubes, $n = m$ (where $\theta = 30$), and $m = 0$ (where $\theta = 0°$), respectively, whereas for all arbitrary (n, m) chiral tubes $0 \leq \theta \leq 30°$. In the example shown in Fig. 1.2(a), the tube chirality is determined by counting n along $\mathbf{a}_1$ and m along $\mathbf{a}_2$, following the dashed lines, resulting in a (4,2) tube.

The electronic properties of CNTs vary according to their diameter and helicity [13]. Tubes for which $2n + m = 3q$, where q is an integer, are metallic, i.e., all armchair tubes are metallic. Among all zigzag and chiral tubes, about a third is metallic and the rest is semiconducting. In general, the chiral tubes can be divided in three groups regarding their predicted electronic properties. 1) $n - m \neq 3q$, it comprises the largest group, about 2/3, in which the tubes are semiconducting. 2) $n - m = 3q$ and $n - m = 3rd$, where r is an integer and d is the largest common divisor or n and m, e.g., (7,4). The tubes in this group are metallic and include the armchair (n, n) tubes. 3) $n - m = 3q$ and $n - m \neq 3rd$. In this group fall the zigzag

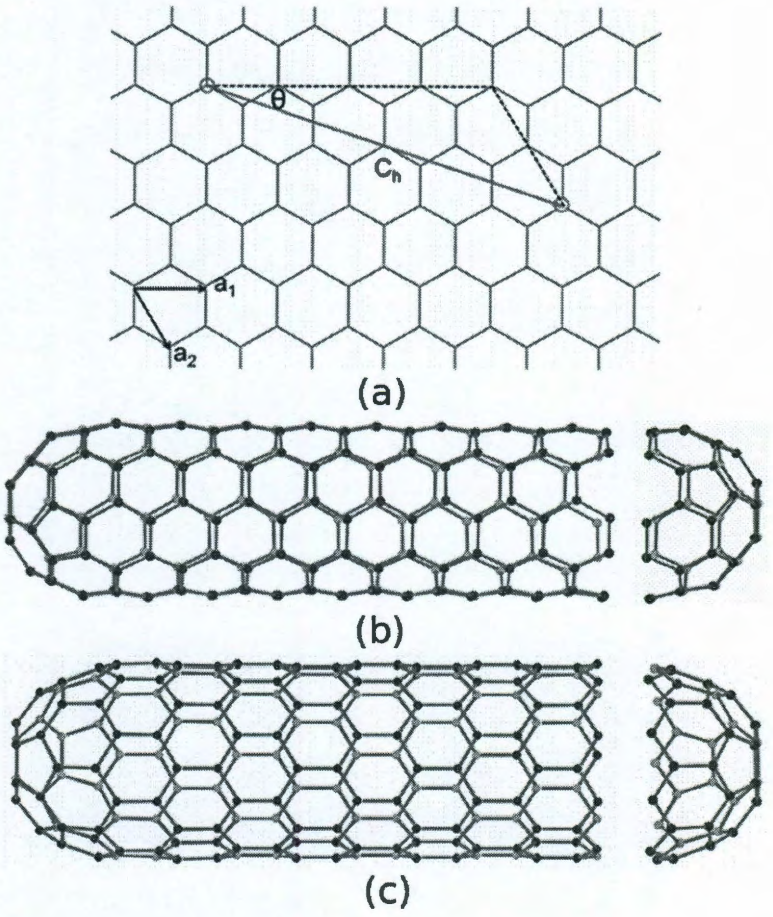

Figure 1.2 : (a) The carbon nanotube unfold as a 2-D graphene sheet. The chiral vector corresponding to a set of (n, m) defines the tube diameter. (b) Example of armchair (5,5) and (c) zigzag (9,0) tubes.

$(0,3q)$ tubes, and all are metallic [14].

1.3.3 Graphene

Graphite has been know for its high in-plane electrical and thermal conductivities and is largely used in iron and steel making, e.g., in electrodes for electric arc furnaces. Its structure of highly oriented stacks of individual graphitic layers has been used for decades to model other graphitic structures as fullerenes and CNTs (Fig. 1.3, reprinted from [15]). There were early reports on the attempts to obtain a monolayer of graphite [16, 17], i.e., graphene, but none was successful until the breakthrough work of Novoselov et al. in 2004 [18].

Several factors contribute to the increasing interest on graphene, among others, the exceptional properties of this material, its newly available production methods, and the search for alternative bottom-up assembly to support the electronics industry fast growth. Graphene has a zero band gap, its electrons behaving as zero rest-mass Dirac Fermions, and it has a nearly ballistic mechanism for charge and energy transport [19].

One of the main limitations of the use of graphene in electronics devices is related with the difficulties of its obtention. The scotch-tape method [18] introduced an easily accessible method to produce monolayer graphene samples to be tested experimentally and was quickly adopted by research groups all around the world. Although efficient and low-cost, the scotch-tape method can be used only for basic research and proof-of-concept devices. Other mass production methods are necessary in order to produce real graphene applications. Epitaxial growth of graphene [20,21] is a technique that is very similar to those used for chip-making and, in the same fashion, can be scaled up for mass production. In epitaxial grow, the monolayer of graphene can be transferred to other substrates, which multiplies further the number of possible applications (e.g.,

flexible opto-electronics devices [20]).

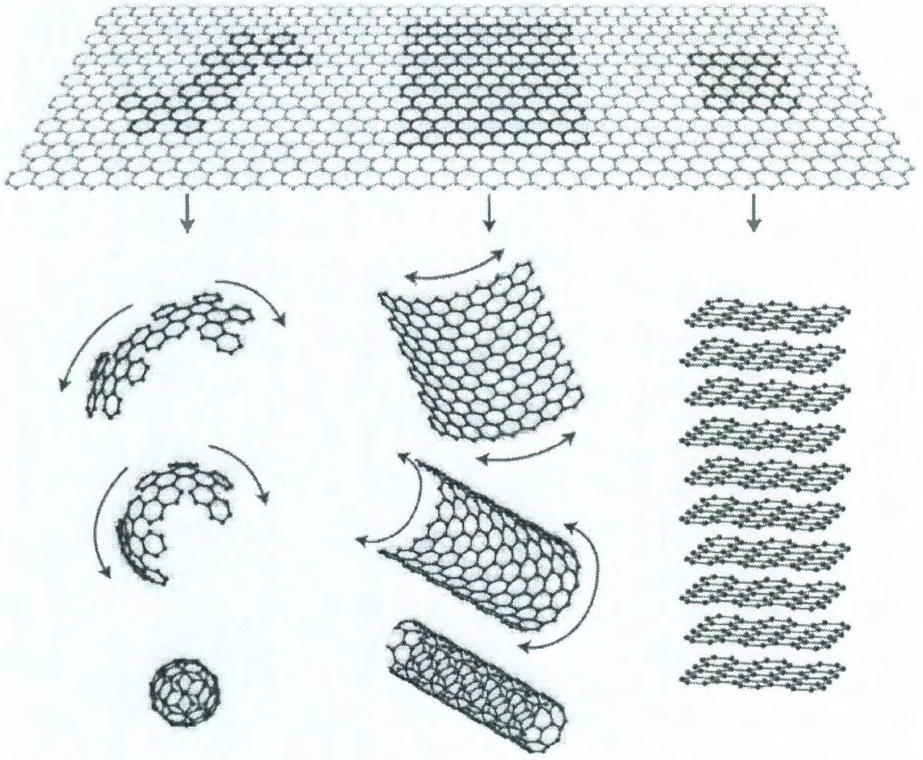

Figure 1.3 : Graphene 2-D sheets building blocks for 0-D buckyballs, 1-D nanotubes and 3-D graphite. Reprinted by permission from Macmillan Publishers Ltd: Nature Materials [15], copyright 2007.

1.4 Processes at nano-scale

1.4.1 Catalyzed growth of carbon nanotubes

One of the main factors hindering the widespread use of CNT for various applications is related with the difficulties in producing tubes with selective chirality. Roughly, CNTs can be produced by either laser ablation, arc-discharge, or chemical vapor deposition (CVD), all using some type of metal, specially transition metals, to catalyze

the process.

Initially, the arc-discharge was the standard method to produce CNTs, but it was only in 1992 that significative amounts of CNTs (on the order of grams) could be produced [22]. In it, two graphite rods are used as electrodes that are placed in inert gas under controlled pressure (typically $\sim$ 500 torr). As a potential is applied and the rods are brought close to each other, a discharge occurs and the carbon atoms are vaporized into a plasma, at very high temperatures (¿3000 °C). The result is a mixture of nanotubes bundles (mostly multi-wall tubes), nanoparticles, fullerenes, and amorphous carbon. Larger amounts of single-wall nanotubes (SWNT) could be synthesized when a mixture of graphite and metal catalyst (e.g., Ni and Co) is introduced inside the anode [23]. Not only the yield of SWNT is driven by the kinetics, but it strongly depends on the temperature (and the temperature gradient) and mixture of metal catalyst.

The laser ablation (or vaporization) technique was introduced in 1995 [24] with the intention to obtain larger amounts of SWNTs. In this method, a laser beam is used against a carbon-metal target, forming a condensing vapor which will flow through the heated tube furnace ($\sim$ 1200 °C). Without the presence of metal particles, the same technique would produce small fullerenes. Thus, the SWNTs production is extremely dependent on the presence of a metallic catalyst, as it will be further discussed in chapter 5. Although this method yields CNT in a narrower diameter (1–2 nm) range, its high cost makes difficult scaling up its production.

The CVD process was already used to produce vapor grown carbon fibers when Endo et al. introduced it as a cheaper alternative to produce SWNT [25]. Basically, it consists of a preliminary step of catalyst deposition on a substrate, to form metallic nanoclusters, followed by the CNT synthesis, in which the carbon precursor gas flows

on the catalyst. The decomposition and activation of solid carbon can be done by plasma or thermal CVD. In plasma-enhanced CVD, the catalyst is generally placed on a substrate by means of a solution or by sputtering process, followed by chemical etching or thermal annealing. The reactive gas then flows towards the catalyst nanoparticles on the substrate, where the CNT will grow at temperatures between 800 and 1500 °C. A flow reactor in a heated furnace, typically at $\sim$ 1000 °C, is generally used in thermal CVD. The catalyst can be supported or unsupported, or just inserted inside the reactor with the feeding gas [26]. The CVD methods are clearly the most suitable for scaling up the process, yielding CNTs with less impurities and in larger amounts.

The separation of CNT from other materials like amorphous carbon and residual nanoparticles can be done through purification methods. However, it is no easy task to actually separate the tubes according with their structural and electronic properties. Initially, the synthesis methods focused on obtaining more uniform diameter distributions of CNT [27–30]. More recent works have showed promising results to sort CNTs, for example using tailored nonlinear density-gradient ultracentrifugation, for post-growth processing to obtain enriched fractions of (n, m) CNT [31], or modifying the growth conditions, to produce a high yield of metallic tubes [32]. Though obtaining controlled growth of a (n, m) CNT is still wishful thinking, further steps towards this goal can be greatly advanced by the theoretical modeling of fundamental catalyzed CNT growth, which is discussed here in chapters 5 and 6.

1.4.2 Catalyzed hydrogen spillover

Given the environmental pressure, limited availability, and consequent increasing prices, of fossil fuels, the United States government launched the Hydrogen Fuel

Initiative in 2003. It aimed at "research, develop and validate hydrogen production, delivery, storage and fuel cell technologies so that hydrogen from diverse domestic resources can be used in a clean, safe, reliable and affordable manner in hydrogen fuel cell vehicles and stationary power applications" [33].

Most of the research being done focus on production of hydrogen, from natural gas by steam methane reforming, coal along with electricity generation, heat generated from nuclear power plants, and natural resources (e.g., electrolysis and thermochemical conversion of biomass). After being produced, the hydrogen has to be transported to points of use, which involves intensive logistics and safety issues due to it volatility and relatively low volumetric energy density. Hence the need to design new materials to store hydrogen in a safe and cost-effective way. The research on hydrogen storage has been intense in recent years, spanning metal hydrides [34, 35], metal organic frameworks [36, 37], and graphitic sorption nanomaterials [38, 39].

The spillover process involves the transport of an active species (e.g., H) formed on a catalyst (mostly transition metals) onto a receptor that does not sorb the species under identical conditions [40]. Besides being fundamental to the spillover process, metallic catalysts have an important role in hydrogen production. Thus, part of the research efforts are focusing on the search for metal catalysts, and their alloys, with improved activity and selectivity for hydrogen production or efficient storage [34, 41–44]. For the first time, through *ab initio* calculations, the mechanism of the hydrogen spillover is presented here, in chapter 3.

1.5 Fluorination of graphene

One of the main issues impeding the use of graphene as a transistor is its lack of a semiconducting counterpart. Conventional semiconductors with band gaps > 0.5 eV

can be used to build microelectronic devices (e.g., Si CMOS) with current on/off ratios appropriate for digital switches [19]. Since graphene is a gapless material the question is: how to open the band gap of graphene?

An alternative is to cut narrow ribbons of graphene, which confine the electronic state of these 1-D structures like in a quantum box. There has been extensive research on graphene nanoribbons (GNRs) fabrication, but the problem on how to cut and assemble these into operational devices persists. Lithographic techniques are used to manipulate atoms at nano-scale. However the dexterity required to produce very narrow GRNs (2–3 nm), which are needed to obtain band gaps > 0.5 eV, cannot be currently obtained by lithographic techniques (see section 4.1 for more details).

The use of lithography to alter the potential of one of the C atoms in the unit cell is also not possible because they are just 0.14 nm apart [19]. However, a recently proposed alternative to overcome these difficulties proposes to use hydrogenated graphene (i.e., graphane [45]) as a matrix-host for geometrical patterning of nanoroads [46] or quantum dots [42].

A comparative analysis of the electronic spectra of graphene, graphane, and fluorinated graphene shows that the carbon hydrogenation or fluorination transforms the system into a semiconductor similar to sp^3 diamond. Their calculated band structures (Fig. 1.4) show that hydrogenation and fluorination open a direct band gap at Γ-point of 3.48 eV and 3.12 eV, respectively [3]. This transition from metal to a wide band gap semiconductor offers a new perspective on how to incorporate graphene into devices. Although, the structure of fluorinated graphene was suggested several years ago [47], there has been no information if fluorinated graphene could be formed. This is done here, through a theoretical investigation about the feasibility of fluorinating graphene and using it as a matrix-host for geometrical patterning of nanoroads and

quantum dots (see chapter 4 for more details).

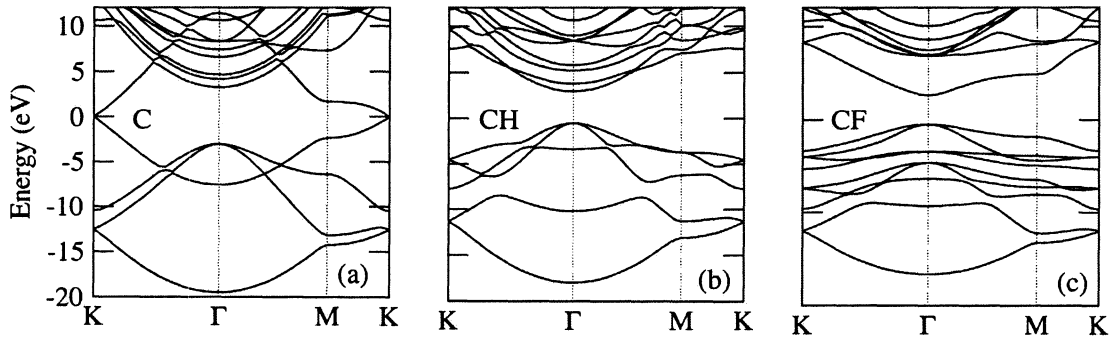

Figure 1.4 : The calculated band structures of (a) graphene, (b) graphane (CH), and (c) fluorinated graphene (CF).

Chapter 2

Theoretical background

2.1 Potential energy surface

The properties of materials can be calculated using different theoretical models based on the relation between their geometrical structure and energy. As illustrated by the simplified potential energy surface (PES) diagram shown in Fig. 2.1(a), the equilibrium structures of reactants and products are obtained at the minima of the curve, whereas the transition state is at its maximum. The difference between the energies of reactants (E_r) and products (E_p) describes their thermodynamical stability. If $E_r < E_p$ the reaction is endothermic, whereas if $E_r > E_p$ it is exothermic. The "kinetics" of the reaction, i.e., the rate at which it will occur, is given by the activation energy or energy barrier between reactants and the transition state. A less idealized chemical reaction may occur in several steps and have more than one transition state, as exemplified by the PES and resulting conformers in the inversion of the cyclohexane (Fig. 2.1(b), adapted from [48]).

2.2 The Schrödinger equation and the Born-Oppenheimer approximation

In 1926, E. Schrödinger presented a new form of quantum theory [49], based on de Broglie's earlier findings on particles with wavelike properties, in a series of six papers originally published in German. At the center of his theory was what later became

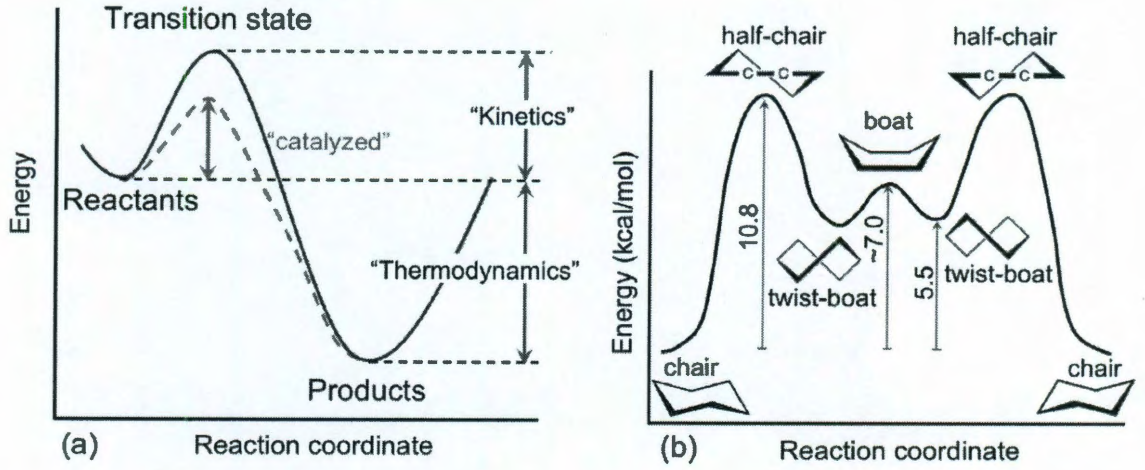

Figure 2.1 : (a) Schematic diagram of the energetic states involved in a chemical reaction. (b) Potential energy surface of the conformational changes during the inversion of cyclohexane. The (b) is adapted with permission from [48]. Copyright 2010 American Chemical Society.

known as the Schrödinger equation (Eq. 2.1).

$$H\,\Psi = E\Psi, \tag{2.1}$$

where H is the Hamiltonian, which is a differential operator representing the total energy, E is the energy of the state in which nuclei and electrons are infinitely separated and at rest, and Ψ is the wavefunction.

By solving Eq. 2.1 for the hydrogen atom, Schrödinger obtained exact values for the energy and the electron density and reproduced the results of the Bohr theory. However, Schrödinger's equation is yet to be solved exactly for a many-electron system due to the complexity of the mathematical problem involved.

One way to solve Schrödinger's equation for a many-electron system is to use the Born-Oppenheimer approximation, in which the wavefunction is approximated as a

product of its nuclear and electronic parts (Eq. 2.2).

$$\Psi(\mathbf{X},\mathbf{x}) = \Psi_{\mathrm{n}}(\mathbf{X}) \cdot \Psi_{\mathrm{e}}(\mathbf{x}), \tag{2.2}$$

where $\mathbf{X}$ represents the nuclear coordinates and $\mathbf{x}$ the electronic coordinates.

Since the mass of a nucleus is much larger than the one of an electron, it can be assumed that the nucleus is going to move much slower than the electron. Based on this assumption, the insertion of Eq. 2.2 into Eq. 2.1, leads to Schrödinger's equation for a many-electron system (Eq. 2.3).

$$\left(H_{\mathrm{k,e}} + H_{\mathrm{p,e\text{-}e}} + H_{\mathrm{p,n\text{-}e}}\right) \Psi_{\mathrm{e}}(\mathbf{X},\mathbf{x}) = E_{\mathrm{e}}(\mathbf{X})\Psi_{\mathrm{e}}(\mathbf{X},\mathbf{x}), \tag{2.3}$$

where $H_{\mathrm{k,e}}$, $H_{\mathrm{p,e\text{-}e}}$, and $H_{\mathrm{p,n\text{-}e}}$ are the kinetic energy operator for the electrons, the potential energy operator for the electron-electron interaction, and the potential energy operator of the nucleus-electron interaction, respectively [50]. So Ψ_{e} is a N electron wavefunction which depends on $3\,N$ space coordinates and N spin variables.

The solution of Schrödinger's equation can determine the energy and other properties of the stationary state of a molecule using the values of just a few physical constants. This non-empirical approach is said to be from first-principles, i.e., *ab initio*.

2.3 Density functional theory

2.3.1 Thomas-Fermi theory

Shortly after Schrödinger's theory was presented, Thomas and Fermi suggested that for very large systems, i.e., very large N, the system could be treated statistically. According with their proposal, an equation to determine the electron density $\rho(\mathbf{r})$ is used, instead of solving Schrödinger's equation for Ψ_{e}. Thus the total energy according with Thomas-Fermi theory (E_{T-F}) is given by the sum of the kinetic energy, an

external potential generated by the nuclei (V_{ext}), and the electron-electron interactions, as shown in Eq. 2.4 [50].

$$E_{\text{T-F}}[\rho(\mathbf{r})] = \frac{3}{10}(3\pi^2)^{\frac{2}{3}} \int \rho^{\frac{5}{3}}(\mathbf{r})\, d\mathbf{r} + \int V_{ext}(\mathbf{r})\rho(\mathbf{r})\, d\mathbf{r} + \frac{1}{2}\iint \frac{\rho(\mathbf{r}_1)\,\rho(\mathbf{r}_2)}{|\mathbf{r}_1 - \mathbf{r}_2|}\, d\mathbf{r}_1 d\mathbf{r}_2. \tag{2.4}$$

The E_{T-F} may be minimized with respect to the electronic density, $\delta(E - \mu N) = 0$, considering that the total number of electrons N is given by

$$\int \rho(\mathbf{r})\, \mathrm{d}\mathbf{r} \;=\; N, \tag{2.5}$$

and using the chemical potential μ as a Lagrange multiplier for the constrain, results in Eq. 2.6 ,which can be solved self-consistently.

$$\mu = \frac{1}{2}\Big\{3\pi^2\rho(\mathbf{r})\Big\}^{\frac{2}{3}} - V(\mathbf{r}) + \int \frac{\rho(\mathbf{r}_1)}{|\mathbf{r}_1 - \mathbf{r}_2|} d\mathbf{r}_2. \tag{2.6}$$

However, the results given by Eq. 2.6 are just a rough estimate and are quite inaccurate. Additionally, the Thomas-Fermi theory does not justify why to use the electron density as the fundamental variable. So, as W. Kohn commented in his Nobel lecture [51], the T-F theory "received only modest attention".

2.3.2 Hohenberg-Kohn theorems

Several decades passed and many important contributions to theoretical chemistry were made by trying to find approximate mathematical methods to solve Schrödinger's equation. The breakthrough for what is known today as density functional theory (DFT) came only in 1964 with the Hohenberg-Kohn (H-K) theorems [52]. As in the T-F theory, it considers that N electrons are subject to an external electrical field ($V_{\text{ext}}(\mathbf{r})$) and electrostatic interactions. As the non-degenerated ground state Ψ

electronic density is a functional of $V(\mathbf{r})$, so

$$\rho(\mathbf{r}) \equiv \langle \Psi | \psi^*(\mathbf{r}) \psi(\mathbf{r}) | \Psi \rangle. \tag{2.7}$$

The first H-K theorem proves that $V(\mathbf{r})$ is a unique functional of $\rho(\mathbf{r})$ by *reductio ad absurdum*, i.e., showing that the opposite would be impossible. Assuming that another external potential $V'(\mathbf{r})$ on ground state Ψ' has the same $\rho(\mathbf{r})$, since Ψ' cannot be equal to Ψ, then $V'(\mathbf{r}) - V(\mathbf{r}) = \text{const}$. Thus,

$$E' = \langle \Psi' | H' | \Psi' \rangle < \langle \Psi | H' | \Psi \rangle = \langle \Psi | H + V' - V | \Psi \rangle \tag{2.8}$$

and, consequently,

$$E' < E + \int \Big[V'(\mathbf{r}) - V(\mathbf{r}) \Big] \rho(\mathbf{r}) d\mathbf{r}. \tag{2.9}$$

Since it is assumed that both states have the same $\rho(\mathbf{r})$, then

$$E < E' + \int \Big[V(\mathbf{r}) - V'(\mathbf{r}) \Big] \rho(\mathbf{r}) d\mathbf{r}. \tag{2.10}$$

The absurd of this assumption is seen by adding 2.9 and 2.10, which leads to the contradiction

$$E + E' < E + E'. \tag{2.11}$$

Thus, for the first time, it was showed that the energy ground state could be represented exactly by the electronic density $\rho(\mathbf{r})$, which was one of the weaknesses of the T-F theory. The kinetic and interaction energies are clearly functionals of $\rho(\mathbf{r})$, and for a given potential V,

$$E_{\mathrm{V}}[\rho] = T_{\mathrm{k,e}}[\rho] + U_{\mathrm{p,e\text{-}e}}[\rho] + U_{\mathrm{p,n\text{-}e}}[\rho] = \int \rho(\mathbf{r})\, V(\mathbf{r})\, d\mathbf{r} + F_{\mathrm{H\text{-}K}}[\rho(\mathbf{r})], \tag{2.12}$$

where the subscripts correspond to those shown in Eq. 2.3 and $F_{\text{H-K}}[\rho]$ is " a universal functional, valid for any number of particles and any external potential" [52] defined as

$$F_{\text{H-K}}[\rho] = T_{\text{k,e}} + U_{\text{p,e-e}}. \tag{2.13}$$

In their second theorem, Hohemberg and Kohn applied the energy variational principle to Eq. 2.12, such that $\tilde{\rho}[\mathbf{r}] \geqslant 0$ and $N[\rho] \equiv \int \tilde{\rho}(\mathbf{r})\, d\mathbf{r} = N$, for a trial density $\tilde{\rho}$. Thus,

$$E_0 \leqslant E_{\text{V}}[\tilde{\rho}]. \tag{2.14}$$

Analogous to the variational principal for wavefunctions, $E_{\text{V}}[\tilde{\rho}]$ is the energy functional of Eq. 2.12 [53].

As proved by their first theorem, each ρ will determine a unique Ψ and H. Thus the energy functional of Ψ' is

$$\xi_V[\Psi'] \equiv \langle \Psi' | H | \Psi' \rangle = \int V(\mathbf{r})\, \rho'(\mathbf{r}) d\mathbf{r} + F_{\text{H-K}}[\rho'] \tag{2.15}$$

$$> \xi_V[\Psi] = \int V(\mathbf{r})\, \rho(\mathbf{r}) d\mathbf{r} + F_{\text{H-K}}[\rho] \tag{2.16}$$

According with Eq. 2.14, the ground state density should satisfy the stationary principle. Thus,

$$\delta \left\{ E_{\text{V}}[\rho] - \mu \left[\int \rho(\mathbf{r})\, d\mathbf{r} - N \right] \right\} = 0, \tag{2.17}$$

which results in the Euler-Lagrange equation

$$\mu = \frac{\delta E_{\text{V}}[\rho]}{\delta \rho(\mathbf{r})} = V(\mathbf{r}) + \frac{\delta\, F_{\text{H-K}}[\rho]}{\delta \rho(\mathbf{r})}. \tag{2.18}$$

By removing the classical long range interaction Coulomb energy from $F[\rho]$ in 2.12, another universal functional $G[\rho]$ is defined,

$$G[\rho] = F_{\text{H-K}}[\rho] - \frac{1}{2} \iint \frac{\rho(\mathbf{r})\, \rho(\mathbf{r}')}{|\mathbf{r} - \mathbf{r}'|} d\mathbf{r} d\mathbf{r}'. \tag{2.19}$$

So, the total energy $E_V[\rho]$ becomes

$$E_V[\rho] = \int V(\mathbf{r})\,\rho(\mathbf{r})\,d\mathbf{r} + \frac{1}{2}\iint \frac{\rho(\mathbf{r})\,\rho(\mathbf{r}')}{|\mathbf{r}-\mathbf{r}'|} d\mathbf{r}d\mathbf{r}' + G[\rho]. \tag{2.20}$$

In summary, the H-K theorems showed that the ground state energy can be determined if $F_{\text{H-K}}[\rho]$ is known. However, further information on how to determine this functional was achieved later, in 1965, through the derivation of the Kohn-Sham equations.

2.3.3 Kohn-Sham equations

The Kohn-Sham (K-S) method [54] consists of a set of self-consistent equations to solve the one-particle Schrödinger equation, where only the true chemical potential $\mu(\rho)$ of a homogeneous interacting electron gas needs to be known. It introduced a set of normalized orthogonal orbitals ψ_i which permitted the kinetic energy and the total electron density to be written in a much simpler way.

For a wavefunction describing N non-interacting electrons, the kinetic energy can be written as

$$T_s[\rho] = \sum_i^N \langle\psi_i| -\frac{1}{2}\nabla^2|\psi_i\rangle. \tag{2.21}$$

The total energy, as given in Eq. 2.20, is minimized at the correct density function $\rho(\mathbf{r})$ and $G[\rho]$ can be approximated as the sum of the exact kinetic energy $T_{\text{k,e}}[\rho]$ of a system of non-interacting electrons and a small residual correction,

$$G[\rho] \equiv T_{\text{k,e}}[\rho] + E_{\text{xc}}[\rho], \tag{2.22}$$

where $E_{\text{xc}}[\rho]$ is the exchange and correlation energy of an interacting system.

From the stationary principle, shown in Eq. 2.20,

$$\int \delta\rho(\mathbf{r})\Big\{\frac{T_{\text{s}}[\rho]}{\rho(\mathbf{r})} + V_{\text{eff}}\Big\}\,d\mathbf{r} = 0, \tag{2.23}$$

where

$$V_{\text{eff}}(\mathbf{r}) = V(\mathbf{r}) + \int \frac{\rho(\mathbf{r}')}{|\mathbf{r} - \mathbf{r}'|} d\mathbf{r}' + V_{\text{xc}}(\rho). \tag{2.24}$$

The $V_{\text{eff}}(\mathbf{r})$ is an effective potential, in which V_{xc} is the exchange and correlation contribution to the chemical potential of a uniform gas of density ρ. Considering that the gradient of V_{xc} results in forces on the electronic fluid, it can be considered as an additional effective potential, which is called the exchange-correlation potential [53].

Thus, at a given $V_{\text{eff}}(\mathbf{r})$, $\rho(\mathbf{r})$, can be obtained by solving the one-particle Schrödinger equation

$$\left[-\frac{1}{2}\nabla^2 + V_{\text{eff}}(\mathbf{r}) \right] \psi_{\text{i}}(\mathbf{r}) = \epsilon_{\text{i}} \psi_{\text{i}}(\mathbf{r}), \tag{2.25}$$

and setting the total electronic density as

$$\rho(\mathbf{r}) = \sum_{i}^{N} \sum_{s} |\psi_i(\mathbf{r}, s)|^2. \tag{2.26}$$

The set of K-S equations (Eq. 2.24 to Eq. 2.26) can be solve self-consistently, and the electron density can be calculated quite accurately. Thereafter, DFT has became one of the most useful theories in theoretical chemistry and materials science, and it is now largely applied to solve *ab initio* many-body problems of molecular motion and interaction.

It is important to note that DFT applicability depends greatly on how much precise and easily calculated the exchange-correlation energy functional $E_{\text{xc}}(\rho)$ is, which is discussed next.

2.3.4 Functionals for the exchange and correlation

Much of the "modern" development of the DFT involves the search for more direct ways to determine the exchange and correlation part of the potential. Among

them, the two most relevant functionals are the local density approximation (LDA) and the generalized-gradient approximation (GGA), which are also used in the DFT calculations shown in this work.

The LDA approximation was proposed by Kohn and Sham [54] and it shows the simplest way to calculate $E_{\rm xc}[\rho]$. It proposes that since the non-interacting kinetic energy and the long range Hartree terms are separated, for a sufficient slow variation of $\rho(\mathbf{r})$, $E_{\rm xc}[\rho]$ can be reasonably approximated as a local or near local functional of the density, so the K-S method assumes that

$$E_{\rm xc}^{\rm LDA}[\rho] \;=\; \int \rho(\mathbf{r})\, \epsilon_{\rm xc}^{\rm hom}\left(\rho(\mathbf{r})\right)\, d\mathbf{r}, \tag{2.27}$$

where $E_{\rm xc}^{\rm LDA}$ is the LDA for exchange and correlation energy and $\epsilon_{\rm xc}(\rho)$ is the exchange and correlation energy per electron of a uniform electron gas density ρ.

Thus, the corresponding exchange and correlation potential of Eq. 2.24 is

$$V_{\rm xc}^{\rm LDA}(\mathbf{r}) \;=\; \frac{\delta E_{\rm xc}^{\rm LDA}}{\delta\rho(\mathbf{r})} \;=\; \epsilon_{\rm xc}^{\rm hom}(\rho(\mathbf{r})) \;+\; \rho(\mathbf{r})\frac{\delta\epsilon_{\rm xc}^{\rm hom}(\rho)}{\delta\rho}, \tag{2.28}$$

so the K-S equation is

$$\left[-\frac{1}{2}\nabla^2 \;+\; V(\mathbf{r}) \;+\; \int \frac{\rho(\mathbf{r}')}{|\mathbf{r}-\mathbf{r}'|}\, d\mathbf{r}' \;+\; V_{\rm xc}^{\rm LDA}\right]\psi_i \;=\; \epsilon_i\psi_i, \tag{2.29}$$

which can be solved self-consistently. Note that the local spin density approximation (LSDA) is given by substituting $\rho(\mathbf{r}) = \rho\uparrow(\mathbf{r}) + \rho\downarrow(\mathbf{r})$. Thus,

$$E_{\rm xc}^{\rm LSDA}(\rho\uparrow,\rho\downarrow) \;=\; \int \rho(\mathbf{r})\, \epsilon_{\rm xc}^{\rm hom}\left(\rho\uparrow,\rho\downarrow\right)\, d\mathbf{r}. \tag{2.30}$$

For the GGA,

$$E_{\rm xc}^{\rm GGA}(\rho\uparrow,\rho\downarrow) \;=\; \int f\left(\rho\uparrow,\rho\downarrow,\nabla\rho\uparrow,\nabla\rho\downarrow\right)\, d\mathbf{r}, \tag{2.31}$$

where f, like ϵ_{xc}, must be a parametrized analytic function. Among the different forms of GGA, the one by Perdew, Burke and Ernzerhof [55] has shown very good accuracy and transferability and is the one discussed here.

The GGA-PBE functional is such that "all parameters (other than those in $\epsilon_c^{hom}(\rho\uparrow, \rho\downarrow)$) are fundamental constants" [55]. For the correlation,

$$E_c^{GGA-PBE}[\rho\uparrow, \rho\downarrow] = \int \rho[\epsilon_c^{hom}(r_s, \zeta) + H(r_s, \zeta, t)]d\mathbf{r}, \tag{2.32}$$

where r_s is the local Seitz radius, $\zeta(= (\rho\uparrow - \rho\downarrow)/\rho)$ is the relative polarization, and t is a dimensionless density gradient [56].

The gradient contribution H is given by

$$H = (\frac{e^2}{a_0})\gamma\phi^3 \times ln\Big\{1 + \frac{\beta}{\gamma}t^2\Big[\frac{1 + At^2}{1 + At^2 + A^2t^4}\Big]\Big\}, \tag{2.33}$$

where

$$A = \frac{\beta}{\gamma}\Big[exp\{-\epsilon_c^{hom}/(\gamma\phi^3 e^2/a_0)\Big\} - 1\Big]^{-1}. \tag{2.34}$$

The exchange and correlation is given by

$$E_{xc}^{\text{GGA-PBE}}[\rho\uparrow, \rho\downarrow] = \int \rho\epsilon_x^{hom}(\rho)F_x(r_s, \zeta, s)d\mathbf{r} \tag{2.35}$$

where the enhancement factor F_x is

$$F_x(s) = 1 + \kappa - \kappa/(1 + \mu s^2/\kappa). \tag{2.36}$$

A complete description of the GGA-PBE, including all derivation and parametrization, is available in Ref. [55,56].

2.4 Other theorems and schemes

2.4.1 Bloch theorem

Due to the translational symmetry of crystals, in periodic boundary conditions the eigenfunctions of the one-electron K-S equations can be written as the product of a periodic function $u_{n\mathbf{k}}$, viz., the Bloch function, and a plane wave function [50, 57]. Thus,

$$\psi_{n\mathbf{k}}(\mathbf{r}) = u_{n\mathbf{k}}(\mathbf{r})e^{i\mathbf{k}\cdot\mathbf{r}}. \tag{2.37}$$

The electronic band structure is given by the n energy bands associated with the solution of the Schrödinger equation for the wave vector $\mathbf{k}$, which is constrained to the first Brillouin zone of the reciprocal lattice.

Operating the translational vector $\mathbf{r}$ on the wavefunction, so $\mathbf{R} = \sum_{i=1}^{3} m_i \mathbf{a_i}$, gives the periodic Bloch function,

$$u_{n\mathbf{k}}(\mathbf{r}) = u_{n\mathbf{k}}(\mathbf{r} + \mathbf{R}) \tag{2.38}$$

where $\mathbf{a_i}$ are the primitive lattice vectors, and m_i are integers.

In reciprocal space, the respective energy eigenvalues are given by

$$\epsilon_n(\mathbf{k}) = \epsilon_n(\mathbf{k} + \mathbf{K}), \tag{2.39}$$

where $\mathbf{K} = \sum_{i=1}^{3} m_i \mathbf{b_i}$, and b_i are the reciprocal lattice vectors.

2.4.2 Plane waves

Delocalized plane waves can be used as basis functions to construct the one-electron wavefunctions and the K-S equations in periodic boundary conditions. The periodic

Bloch function can be expanded in a finite set of Fourier components, i.e., plane waves basis functions, so the eigenfunction can be written as

$$\psi_{n\mathbf{k}}(\mathbf{r}) = \frac{q}{\sqrt{\Omega}} \sum_{\mathbf{K}} C_{\mathbf{K}n\mathbf{k}}\, e^{i(\mathbf{k}+\mathbf{K})\cdot\mathbf{r}} \equiv \sum_{\mathbf{K}} C_{\mathbf{K}n\mathbf{k}} |\mathbf{k}+\mathbf{K}\rangle, \tag{2.40}$$

where $C_{\mathbf{K}n\mathbf{k}}$ are the expansion coefficients of the wavefunction in an orthonormal basis. Other periodic cell quantities, as the K-S equations can also be expanded in plane waves basis functions,

$$\langle \mathbf{k}+\mathbf{K}| \, -\frac{1}{2}\nabla + V|\psi_{n\mathbf{k}}\rangle = \epsilon_{n\mathbf{k}} \langle \mathbf{k}+\mathbf{K}|\psi n\mathbf{k}\rangle. \tag{2.41}$$

The kinetic energy contribution can also be calculated in reciprocal space,

$$\langle \mathbf{k}+\mathbf{K}| \, -\frac{1}{2}\nabla|\psi_{n\mathbf{k}}\rangle = -\frac{1}{2}|\mathbf{k}+\mathbf{K}|^2 \, C_{\mathbf{K}n\mathbf{k}}. \tag{2.42}$$

In the same way, the local potential can also be calculated as a sum of Fourier components. However, it is more conveniently calculated in real space,

$$\langle \mathbf{k}+\mathbf{K}| \, V|\psi_{n\mathbf{k}}\rangle = \frac{1}{N_{\mathrm{FFT}}} \sum_{\mathbf{r}} V_{\mathbf{r}} C_{\mathbf{r}n\mathbf{k}} e^{-i\mathbf{K}\cdot\mathbf{r}} \tag{2.43}$$

for $V(\mathbf{r}) = \sum_{i=1}^{3} n_i \mathbf{a}_i / N_i$. The Coulomb part of the local potential, $V_{C,\mathbf{K}}$ can be calculated by solving the Poisson equation in reciprocal space, whereas the exchange and correlation part can be obtained by calculating the charge density in real space. Through a fast Fourier transform (FFT), $V_{\mathrm{xc},\mathbf{r}}$ is calculated in reciprocal space. The external part of the potential is substituted by a pseudopotential, as it will be showed in section 2.4.3. Through another FFT, the local potential is transformed from reciprocal space to real space, yielding

$$-\frac{1}{2}|\mathbf{k}+\mathbf{K}|^2 C_{\mathbf{K}n\mathbf{k}} + \frac{1}{N_{\mathrm{FFT}}} \sum_{\mathbf{r}} V_{\mathbf{r}} C_{\mathbf{r}n\mathbf{k}} e^{-i\mathbf{K}\cdot\mathbf{r}} = \epsilon_{n\mathbf{k}} \, C_{\mathbf{K}n\mathbf{k}}. \tag{2.44}$$

2.4.3 Pseudopotentials

The use of plane waves as basis functions, as described above, can be computationally prohibitive as the number of necessary plane waves increases with the size of the system. However, the frozen core and pseudopotential approximations can be used to reduce the computational effort. In the first, since most physical properties of the atoms are determined mainly by their valence electrons, the electronic wavefunctions of the core electrons can be pre-calculated and kept invariable during the subsequent steps of the calculation. In the second approximation, the ionic potential due to the nuclear charges is substituted by an effective pseudopotential, which can then be represented by a plane waves basis set (as shown in section 2.4.2).

The concept behind the pseudopotential is that since the core electrons screen the charge of the nuclei, the valence electrons can be consider to be moving in a pseudopotential of the true potential screened by the core electrons. The idea to calculate the wavefunctions and energies by using orthogonalized plane waves to the core eigenfunctions was first proposed by Herring in 1940 [58]. However, only in 1959, Phillips and Kleinman [59] showed that a combination of screening by the core electrons and the repulsive force due to the Pauli principle diminished the Couloumb potential resulting in a weak pseudopotential. This effect can be seen in the schematic diagram of Fig. 2.2, which shows that above the radius r_c the true and pseudo-potential match perfectly.

Thus, the external potential in reciprocal space $V_{ext,\mathbf{K}}$ is given by

$$V_{\mathrm{ext},\mathbf{K}} = \sum_{\alpha} S_{\alpha,\mathbf{K}} \tilde{V}_{\alpha,\mathbf{K}}, \tag{2.45}$$

where $\tilde{V}_{\alpha,\mathbf{K}}$ is the local ionic pseudopotential in reciprocal space and $S_{\alpha,\mathbf{K}} = \sum_{I} e^{i\mathbf{K}\cdot\mathbf{R}_i}$ is the structure factor of the species α over all lattice sites $\mathbf{R}_I$.

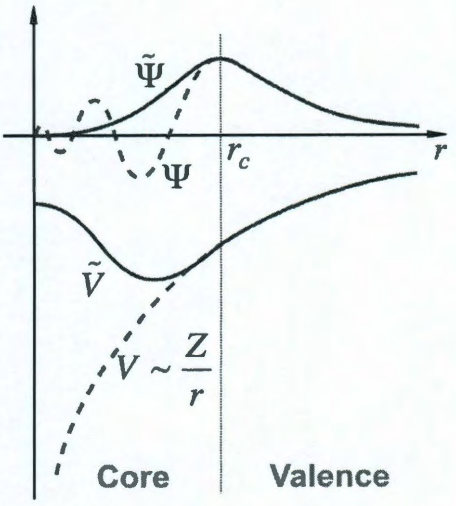

Figure 2.2 : Schematic diagram of the true ionic V and pseudo-potential $\tilde{V}$ and their respective wavefunctions ψ and $\tilde{\psi}$.

There are several ways to obtain the ionic pseudopotential. For example, it can be empirically fitted to experimental results of the electronic band structure or derived by *ab initio* calculations. Additionally, the pseudopotential should be highly transferable among different chemical environments. The discussion here will be restricted only to the two types of *ab initio* approximations which are used for calculations in this work, ultrasoft potentials and projected augmented waves.

2.4.4 Ultrasoft potentials

The Vanderbilt method [60] describes how to directly obtain a non-local smooth pseudopotential with desirable properties, e.g., becomes local and vanishes outside the core, becomes involved in the self-consistent screening, and more than one energy per quantum state is allowed. The construction of the pseudopotential follows tree stages. In the first, a nonlocal Kleinman-Bylander pseudopotential is obtained with avoidance

of the construction of the semi-local potential. For an all-electron wavefunction ψ_i, at an arbitrary energy ϵ_i, which leads to a screened potential V_{AE},

$$(-\frac{1}{2}\nabla + V_{\mathrm{AE}} - \epsilon_i)|\psi_i\rangle = 0. \tag{2.46}$$

A norm-conserving pseudo-wavefunction ϕ_i, smoothly equal to ψ_i at the cut-off radius, can be constructed. The resulting wavefunction is local,

$$|\chi_i\rangle = (\epsilon_i + \frac{1}{2}\nabla - V_{\mathrm{loc}})|\psi_i\rangle, \tag{2.47}$$

so a nonlocal pseudopotential operator is defined,

$$V_{NL} = \frac{|\chi_i\rangle\langle\chi_i|}{\langle\chi_i|\phi_i\rangle}. \tag{2.48}$$

In the second stage, the pseudopotential is generalized for two or more energies, satisfying the norm conservation condition that $Q_{ij} = 0$,

$$Q_{ij} = \langle\psi_i|\psi_j\rangle_{\mathbf{R}} - \langle\phi_i|\phi_j\rangle_{\mathbf{R}}. \tag{2.49}$$

So the local wave functions are defined for the matrix $B_{ij} = \langle\phi_i|\chi_j\rangle$,

$$|\beta_i\rangle = \sum_j (B^{-1})_{ji}|\chi_j\rangle, \tag{2.50}$$

and the local pseudopotential operator V_{NL} is chosen as

$$V_{\mathrm{NL}} = \sum_{i,j} B_{ij}|\beta_i\rangle\langle\beta_j|. \tag{2.51}$$

In the final stage, a nonlocal overlap operator S is defined and the constraint $Q_{ij} = 0$ is relaxed. Thus, the only constraint now is that $\phi(\mathbf{r})$ and $\psi(\mathbf{r})$ should match at the cut-off radius.

$$S = 1 + \sum_{i,j} Q_{ij}|\beta_i\rangle\langle\beta_j| \tag{2.52}$$

So the nonlocal pseudopotential operator is given by

$$V_{\mathrm{NL}} = \sum_{i,j} D_{ij} |\beta_i\rangle\langle\beta_j|, \tag{2.53}$$

where $D_{ij} = B_{ij} + \epsilon_j Q_{ij}$.

Thus, the secular equation becomes

$$\Big(-\frac{1}{2}\nabla^2 + V_{\mathrm{loc}} + V_{\mathrm{NL}} - \epsilon_{n\mathbf{k}} S \Big) |\phi_{n\mathbf{k}}\rangle = 0, \tag{2.54}$$

for

$$V_{H_{\mathrm{xc}}}(\mathbf{r}) = V_H^{[n_v]}(\mathbf{r}) + V_{\mathrm{xc}}^{[n_v+n_c]}(\mathbf{r}) \tag{2.55}$$

and

$$D_{ij}^{H_{\mathrm{xc}}} = \int V_{H_{\mathrm{xc}}} Q_{ij} d^3r. \tag{2.56}$$

2.4.5 Projector-augmented wave method

The projector-augmented wave method [61] performs a linear transformation of the true all-electron wavefunctions $\psi_{n\mathbf{k}}$ (one-electron K-S wavefunction) into pseudo wavefunctions $\tilde{\psi}_{n\mathbf{k}}$, which can be represented as a plane wave expansion. Thus,

$$|\psi_{n\mathbf{k}}\rangle = |\tilde{\psi}_{n\mathbf{k}}\rangle + \sum_i (|\phi_i\rangle - |\tilde{\phi}_i\rangle) \langle\tilde{p}_i|\tilde{\psi}_{n\mathbf{k}}\rangle, \tag{2.57}$$

where ϕ and $\tilde{\phi}$ are the respective partial and pseudo partial waves, which are centered at the atomic sites.

There is one projector function $\langle\tilde{p}_i|$ for each $\tilde{\Psi}$, such that the one-center expansion of the pseudo wavefunction is identical to $\tilde{\Psi}$, so

$$\left\langle \tilde{p}_i | \tilde{\phi}_j \right\rangle = \delta_{ij}. \tag{2.58}$$

The most general form of the projected functions, which are localized in the augmentation region, is given by a linear combination of intermediary functions,

$$\langle \tilde{p}_i| = \sum_j \Big(\langle \tilde{\phi}_i | f_j \rangle \Big)^{-1}_{ij} \langle f_j|, \tag{2.59}$$

where $|f_i\rangle$ form an arbitrary, linear independent set of functions,

$$|f_i\rangle = \Big(\epsilon_i + \frac{1}{2}\nabla - \tilde{V} \Big) |\tilde{\phi}_i\rangle, \tag{2.60}$$

for a $\tilde{V}$ spherical effective atomic pseudopotential.

The K-S eigenvalue equation can be obtained exactly for $\tilde{\phi}$,

$$\Big(-\frac{1}{2}\nabla + \tilde{V} + \sum_{ij} |\tilde{p}_i\rangle \, D_{ij} \langle \tilde{p}_j| \Big) |\tilde{\phi}_k\rangle = \epsilon_k \Big(1 + \sum_{ij} |\tilde{p}_i\rangle \, Q_{ij} \langle \tilde{p}_j| \Big) |\tilde{\phi}_k\rangle, \tag{2.61}$$

for specific compensation charges Q_{ij}, for

$$Q_{ij} = \langle \phi_i | \phi_j \rangle - \langle \tilde{\phi}_i | \tilde{\phi}_j \rangle, \tag{2.62}$$

and one-center strength parameters D_{ij},

$$D_{ij} = \langle \phi_i | -\frac{1}{2}\nabla + V | \phi_j \rangle - \langle \tilde{\phi}_i | -\frac{1}{2}\nabla + \tilde{V} | \tilde{\phi}_j \rangle. \tag{2.63}$$

2.5 Tight-binding density functional theory

The tight-binding density functional theory (DFTB) is an approximation for the Kohn-Sham method. One of the main advantages of this approximation is the ability to simulate larger systems, which would not be possible through *ab initio* methods, without any empirical parametrization as done in molecular dynamics. For simplification, single-electron orbitals ϕ_k can be expanded as a set of basis functions χ_i,

$$\phi_k(\mathbf{x}) = \sum_{i=1}^{N_b} \chi_i(\mathbf{x}) c_{ik}, \tag{2.64}$$

which can in turn be modeled by atomic orbitals as

$$\chi(\mathbf{r}) = R_{nl}(r)Y_{lm}(\theta,\phi), \tag{2.65}$$

i.e., as a linear combination of atomic orbitals (LCAO). So the basis function of an atom has an angular part, the spherical harmonic function Y_{lm}, and a radial part R_{nl}.

For Slater-type orbitals [62],

$$R_{nl}(r) = N\, r^{n-1} e^{-\zeta r}, \tag{2.66}$$

where ζ is a constant related with the nuclear charge and N is a normalizing constant given by

$$N = \frac{(2\zeta)^{n+\frac{1}{2}}}{(2\,n!)^{\frac{1}{2}}}. \tag{2.67}$$

A simplified LCAO method was proposed by Slater and Koster (S-K) [63], in which the Hamiltonian eigenstates are described by an atomic-like basis set and replaced by a parameterized Hamiltonian matrix. As a significant simplification, only two-centers integrals are taken into account and the elements of this matrix depend only on the internuclear distances ($\mathbf{u}$). By considering only s, p, and d angular momenta of the atomic orbitals, the resulting two-center integrals can be written in terms of the S-K parameters, which in many cases simplifies the calculations further.

Based on Löwdin functions ϕ_n symmetry properties being similar to the atomic orbital ψ_n from which they are derived, a set of wavefunctions for the set of atoms i (or j), located at $\mathbf{b}$, can be said to be orthogonal. So

$$\langle \psi_{i\alpha} | \psi_{j\beta} \rangle = \int \psi^*_{i\alpha}(\mathbf{r} - \mathbf{R}_m - \mathbf{b}_i)\psi_{j\beta}(\mathbf{r} - \mathbf{R}_n - \mathbf{b}_j)d\mathbf{r} = \delta_{ij}\delta_{mn}, \tag{2.68}$$

where $\mathbf{R}$ is the lattice vector.

In a periodic system, the crystalline translational symmetries can be utilized by transforming the set of wavefunctions based on atomic orbitals into a Bloch sum,

$$\Psi_{\mathbf{k}i\alpha}(\mathbf{r}) = N^{-1/2} \sum_n e^{i\mathbf{k}\cdot\mathbf{R}_n} \psi_{i\alpha}(\mathbf{r} - \mathbf{R}_n - \mathbf{b}_i), \tag{2.69}$$

where $\mathbf{k}$ is the Bloch wavevector and N is the number of unit cells in the sum.

All the matrix elements of the Hamiltonian between two Bloch sums with different $\mathbf{k}$ are diagonalized. The non-diagonal terms within a block of $\mathbf{k}$ can vanish at special symmetry points of the Brillouin zone, and the matrix elements can be written as

$$H_{i\alpha,j\beta}(\mathbf{k}) = \sum_n e^{i\mathbf{k}\cdot\mathbf{R}_n} \int \psi^*_{i\alpha}(\mathbf{r} - \mathbf{R}_n - \mathbf{b}_i) H \psi_{j\beta}(\mathbf{r} - \mathbf{b}_j) d\mathbf{r}. \tag{2.70}$$

The potential part of the Hamiltonian $V(\mathbf{r})$ is given by a sum of spherical potentials located at each atom V_k, which vanish at some distance away from the atom.

$$V(\mathbf{r}) = \sum_{nk} V_k(\mathbf{r} - \mathbf{R}_n - \mathbf{b}_k). \tag{2.71}$$

Substituting Eq. 2.69 and 2.71 into Eq. 2.70, S-K simplified the resulting integral further by considering that the location of the potential is the same as one of the two wavefunctions, i.e., a two-center integral.

$$H^{ij}_{\alpha\beta}(\mathbf{u}) = \int \psi^*_{i\alpha}(\mathbf{r} - \mathbf{u}) H_{2c} \psi_{j\beta}(\mathbf{r}) d\mathbf{r}. \tag{2.72}$$

where H_{2c} represents the kinetic energy operator and a spherically symmetric potential centered on atoms i or j and is dependent on the orientation of $\mathbf{u}$ and its magnitude (separation between the atoms), and on the angular momenta contained in α and β.

A final simplification is to consider only the orbitals with s, p, and d angular momenta, so Eq. 2.72 can be written in terms of ten S-K parameters. These were originally obtained by *ab initio* band structures calculations at high-symmetry points

and used as interpolation parameters to describe the band structure at the Brillouin zone.

More detailed information about the Slater-Koster method and tight binding approximation can be found elsewhere, including Ref. [64, 65].

2.6 Molecular dynamics

2.6.1 Introduction

Statistical mechanics theory can be used to model the macroscopic properties of larger systems, which cannot be modeled by *ab initio* methods, based on their microscopic properties. Molecular dynamics (MD) simulations can be used to compute the distribution and motion of atoms and molecules in a classical many-body system [66].

The observables are averaged over an ensemble, i.e., the systems have distinct atomic positions and momenta, but identical thermodynamical states. Among the most common ensembles, the microcanonical (NVE) consists of systems of N molecules in a V volume that are completely isolated, i.e., have fixed E energy. The canonical ensemble (NVT) is the most commonly used in statistical mechanics and it is placed in a heat bath at temperature T; though each of the systems is impermeable to the passage of molecules, it has heat conducting walls. Another important ensemble is the grand canonical (μVT) in which the systems walls are permeable to the matter; the ensemble is placed in a large reservoir of molecules reaching a constant μ chemical potential in the equilibrium. Similarly, other ensembles can be constructed by varying the constraints, for example an isobaric-isothermal (NPT) ensemble has N, P, and T fixed.

In practice, the resulting observable averages obtained by MD are averaged over

a time interval. The ergodic hypothesis reconciles both ideas by stating that after a sufficiently long time, the ensemble average of the observable $\langle \rho_i(r) \rangle$ is going to be the same as its time average $\overline{\rho_i(r)}$, so $\overline{\rho_i(r)} = \langle \rho_i(r) \rangle$, independent of the initial conditions. Though, this is not true for all the systems (exceptions include glasses and meta-stable phases [66]), it is fundamental to solve statistical mechanics problems through MD simulations.

The Helmholtz free energy is related to the partition function Q in classical statistical mechanics, which is given by

$$Q = c \int exp[-\mathcal{H}(\mathbf{p}^N, \mathbf{r}^N)/k_B T] d\mathbf{p}^N d\mathbf{r}^N, \tag{2.73}$$

where $\mathbf{r}^N$ are the coordinates and $\mathbf{p}^N$ the momenta of all N particles, $\mathcal{H}(\mathbf{p}^N, \mathbf{r}^N)$ is the Hamiltonian, and c is a constant of proportionality.

For a system $\mathcal{A}$, the ensemble average is

$$\langle \mathcal{A} \rangle = \frac{\int \mathcal{A}(\mathbf{p}^N, \mathbf{r}^N) exp[-\beta \mathcal{H}(\mathbf{p}^N, \mathbf{r}^N)] d\mathbf{p}^N d\mathbf{r}^N}{\int exp[-\beta \mathcal{H}(\mathbf{p}^N, \mathbf{r}^N)] d\mathbf{p}^N d\mathbf{r}^N}, \tag{2.74}$$

where $\beta = 1/k_B T$. The corresponding time average of A is

$$\bar{\mathcal{A}} = \lim_{\tau \to \infty} \frac{1}{\tau} \int_{t=0}^{\tau} \mathcal{A}(\mathbf{p}^N(t), \mathbf{r}^N(t)) dt \approx \frac{1}{M} \sum_{t=1}^{M} \mathcal{A}(\mathbf{p}^N, \mathbf{r}^N), \tag{2.75}$$

for a simulation time t and number of simulation steps M. Thus, observables like potential and energy energies can be calculated using Eq. 2.75.

2.6.2 Forces

The trajectories and velocities of the atoms are calculated by solving an equation derived from Newton's second law $\mathbf{F} = m\mathbf{a}$, so

$$m_i \frac{d^2 \mathbf{r}_i}{dt^2} = \sum_j \mathbf{F}_{ij} + \sum \mathbf{F}_{\text{ext,i}} \quad i = 1, 2, \ldots, N, \tag{2.76}$$

where the atom i, of mass m and position $\mathbf{r}$, interacts with atom j, in a system of N atoms. $\mathbf{F}_{\text{ext}}$ includes any forces due to external fields, whereas $\mathbf{F}_{ij}$ represent the two-body interaction forces. The forces are derived from the gradients of the potential energies with respect to the atomic displacements, $\mathbf{F}_i = -\nabla V(\mathbf{r}^1, \ldots, \mathbf{r}^N)$, whereas the potential energy is given by the sum of the interaction potentials u, so $V(\mathbf{r}^1, \ldots, \mathbf{r}^N) = \sum_i \sum_{j>i} u(|\mathbf{r}_i - \mathbf{r}_j|)$. An important and perennial issue is that the quality of MD simulations depends on the accuracy of the interaction potentials.

2.6.3 Integrating the equations of motion

The Verlet [67] is one of the most common algorithms to integrate the equations of motion. It considers a Taylor expansion around the time t, obtaining expressions for $\mathbf{r}(t + \Delta t)$ and $\mathbf{r}(t - \Delta t)$, where Δt is the time increment. From the sum of these two expressions,

$$\mathbf{r}_i(t + \Delta t) + \mathbf{r}_i(t - \Delta t) = 2\mathbf{r}_i(t) + \frac{\mathbf{f}(t)}{m}\Delta t^2 + \mathcal{O}(\Delta t^4) \tag{2.77}$$

or

$$\mathbf{r}_i(t + \Delta t) \approx 2\mathbf{r}_i(t) - \mathbf{r}_i(t - \Delta t) + \frac{\mathbf{f}(t)}{m}\Delta t^2, \tag{2.78}$$

which is the Verlet algorithm.

An expression for the velocities can be derived as

$$\mathbf{v}(t) = \frac{\mathbf{r}_i(t + \Delta t) - \mathbf{r}_i(t - \Delta t)}{2\,\Delta t} + \mathcal{O}(\Delta t^2). \tag{2.79}$$

From the kinetic energy,

$$E_{\text{kin}} = \sum_{i=1}^{N} \frac{m\mathbf{v}_i^2}{2} = \frac{3\,N\,k_{\text{B}}T}{2}, \tag{2.80}$$

the instantaneous temperature $T(t)$ can be obtained by scaling all velocities with a factor $\sqrt{T/T(t)}$.

A MD simulation code generally includes [66]: (i) Read the initial conditions (temperature, number of particles, integration times steps and other pre-defined parameters), (ii) Initialization of coordinates and velocities of the atoms in the system, (iii) Compute the forces on all particles, (iv) Integrate the equations of motion, and (v) Compute the averages of the desirable quantities and stop. Step (iii) is the most time-consuming and together with step (iv) constitute the core of MD simulation, being executed as a loop for a time long enough to produced the desired quantities.

2.6.4 Interatomic potentials

The quality of the PES model depends on how well the system is described by the interatomic potentials. The main atomic and molecular interactions behind the PES are discussed in this section. The effective force fields developed by the Texas A&M University and used in the MD calculations performed in this work are discussed in more details in section 2.6.5.

There are basically two types of atomic interactions in force fields: bonded, which models the interaction forces between the nuclei in the molecule, and non-bonded, which models the interaction between all nuclei. The bonded interactions are usually bond-streching (2-body), bond-bending (three-body), and dihedral angle (4-body) [68]. The first two bonded interactions can be modeled by a harmonic oscillator potential such that $u_{\mathrm{b}} = kx^2/2$, where x is either the bond-length equilibrium distance or the bond angle equilibrium value. However, a diatomic molecule bonded by a harmonic potential would not dissociate, which exposes one of the weaknesses of this potential. Another option to model a bonded interaction is the Morse

potential [69], $V(x) = D_e(1 - e^{-\alpha x})^2$. It is a combination of short-range repulsion and a long-range attractive force, reproducing well the anharmonicity of real molecules. However, its dissociation energy is a bit larger than the real dissociation energy. The dihedral angle contribution can be modeled by a periodic function, so $u_{\text{torsion}}(\phi) = \sum_{i=1}^{n} c_i(cos\phi)^i$, where ϕ is the torsion angle and $c_0, \ldots, c_n$ are constants.

The nonbonded interactions include electrostatic, Van der Waals, and polarization forces. The first one is described by Coulomb interactions. So

$$u(r_{ij}) = \frac{q_i q_j}{4\pi\epsilon_0 r_{ij}}, \tag{2.81}$$

where ϵ_0 is the dielectric constant of vacuum and charged particles i and j (q_i and q_j) are apart by distance r_{ij}.

The polarization forces can be considered implicitly in the Van der Waals interactions, which is then usually modeled by a Lennard-Jones potential [70],

$$u(r_{ij} = 4\epsilon\Big[\Big(\frac{\sigma}{r_{ij}}\Big)^{12} - \Big(\frac{\sigma}{r_{ij}}\Big)^{6}\Big]. \tag{2.82}$$

The first term inside the square brackets describes a short-range Pauli repulsion, whereas the second term describes the attractive long-range Van der Waals potential. The ϵ represents the depth of the potential at the minimum ($r_{\text{min}} = 2^{1/6}\sigma$) and $r = \sigma$ is at $u(r) = 0$. In computations, the Lennard-Jones is generally truncated at a certain cut-off radius ($u_{ij} = 0$ at $r_{ij} > r_{\text{cut}}$), most commonly $r_{\text{cut}} = 2.5\sigma$.

2.6.5 SIMCAT

The semi-empirical SIMCAT potential, which was developed by the Texas A & M University [71] is used here to perform classical MD calculations. Its force field considers separate contributions of carbon-carbon, metal-metal, and metal-carbon interactions. It uses a many-body Morse type potential [72] to describe the interactions between

atomic elements i and j separated by r_{ij}, where the binding energy E_{ij} is given by a combination of attractive, $V^{\mathrm{a}}(r_{ij})$, and repulsive potentials, $V^{\mathrm{r}}(r_{ij})$, as shown in Eq. 2.83. The Ni-Ni interactions are fitted with parameters described by the Sutton-Chen potential [73]. The C-C potential functions are taken from the REBO [74] and the Ni-C are adapted from Yamaguchi and Maruyama [72]. The main feature of this potential is the introduction of weighting factors in the Ni-C and C-C interactions according with the atoms coordination numbers. This differential permits the evaluation of different contributions of the potential energy according with the C and Ni positions. Prior to the present work, this potential was successfully used to simulate carbon nanotube growth on Ni catalytic clusters on a substrate [75, 76].

$$E_{ij} = V^{\mathrm{r}}(r_{ij}) - V^{\mathrm{a}}(r_{ij}). \tag{2.83}$$

As it is shown in chapter 5, the growth on a floating catalyst is possible at appropriate relations of work of adhesion and temperature. Additionally, as shown in section 5.5, *ab initio* simulations of C on Ni surfaces (and other transition metals) can result on very different results, according with the calculation methodology. In fact, previous to the present work, the SIMCAT potential was unsuccessful to simulate the cap lift-off on a floating catalyst, which was due to the excessively strong Ni-C binding energies previously used by the team at the A & M. The potential functions which describe the Ni-C interactions as implemented on the SIMCAT are described below. Note that a complete description of the interaction functions and parametrization of the SIMCAT is available in reference [71].

A function G is used to modify E_{ij} in order to take into account the different types of metal-C bonds, so

$$E_{ij}^{\mathrm{MC}} = G(\alpha_{ij}^{\mathrm{MC}}, V^{\mathrm{r}}(r_{ij}), V^{\mathrm{a}}(r_{ij}), \tag{2.84}$$

where

$$G = \alpha_{ij}^{\mathrm{MC}} V^{\mathrm{r}}(r_{ij}) - (\alpha_{ij}^{\mathrm{MC}})^{1.1} V^{\mathrm{a}}(r_{ij})). \tag{2.85}$$

The parameter $\alpha_{ij}^{\mathrm{MC}}$ is a function of the total atoms coordination number (N_{ij}), which ensures that C-Ni interaction energy decreases as the number of neighboring atoms increases.

$$\alpha_{ij} = \begin{cases} 1 & N_{\mathrm{carbon}}^{\mathrm{C}} < N_1^{\mathrm{C}}, \text{ i.e., C(0)} \\ \alpha_1 + \dfrac{(1-\alpha_1)}{2}[1+\cos(\pi \dfrac{N_{\mathrm{carbon}}^{\mathrm{C}} - N_1^{\mathrm{C}}}{N_2^{\mathrm{C}} - N_1^{\mathrm{C}}})] & N_1^{\mathrm{C}} < N_{\mathrm{carbon}}^{\mathrm{C}} < N_2^{\mathrm{C}} \\ \alpha_1 & N_2^{\mathrm{C}} < N_{\mathrm{carbon}}^{\mathrm{C}} < N_3^{\mathrm{C}}, \text{ i.e., C(II)} \\ \alpha_2 + \dfrac{(\alpha_1-\alpha_2)}{2}[1+\cos(\pi \dfrac{N_{\mathrm{carbon}}^{\mathrm{C}} - N_3^{\mathrm{C}}}{N_4^{\mathrm{C}} - N_3^{\mathrm{C}}})] & N_3^{\mathrm{C}} < N_{\mathrm{carbon}}^{\mathrm{C}} < N_4^{\mathrm{C}} \\ \alpha_2 & N_{\mathrm{carbon}}^{\mathrm{C}} > N_4^{\mathrm{C}}, \text{ i.e., C(III)} \end{cases}$$

where

$$N_{ij} = N_j^{\mathrm{Ni}} + \lambda N_i^{\mathrm{C}}, \tag{2.86}$$

in which λ weights the contribution of the metal (N_j^{Ni}) and carbon (N_i^{C}) coordination numbers.

Chapter 3

H-Spillover through the catalyst saturation

3.1 Introduction

Hydrogen is a carrier of clean energy [77, 78] and can be easily generated from renewable sources. A cost effective, safe and efficient storage medium is the key to utilize its full potential. Among the various possibilities, the carbon-based adsorbents [38,39,79–82] are recognized as strong candidates, where large surface area and lighter weight make the substantial volumetric and gravimetric content possible. Furthermore, the storage capacity of graphitic materials, e.g., nanotubes and fullerenes, can be significantly enhanced by decorating them with metal atoms [83–88], which absorb multiple H_2 molecules via Kubas interaction [89].

Although promising, the experimental efforts in synthesizing the metal-decorated nanotubes and fullerenes have not been successful so far. Additionally, the tendency of metal atoms to cluster [90,91], leads to considerable reduction in potential storage capacity. In contrast, the metal cluster supported on graphitic materials, acts as a catalyst and enhances the hydrogen uptake of substrates via spillover [92–95].

3.2 The spillover process

The spillover process involves the transport of an active species (e.g., H) formed on a catalyst onto a receptor that does not sorb the species [40] under the same conditions. Current growing interest in efficient storage of hydrogen brought this long-known phe-

nomenon into the spotlight. The most widely used catalysts for spillover of H-atoms on graphitic materials are Ni, Pd, Pt, and 3 d-transition metal atoms. Recently, several experiments have shown the enhancement of H_2 adsorption via spillover on activated carbons and metal-organic framework [93, 96, 97]. Up to 4 wt.% of adsorption has been reported for IRMOF-8 at 298 K and 10 MPa [98]. Furthermore, it is empirically established that the spillover can be enhanced by adding so-called bridges [97] between the catalyst and receptor. Although exact distribution and the binding sites of the H remain experimentally unspecified, it is reasonable to suggest that the best coverage of the H on graphitic substrates can be achieved when they are hydrogenated on both sides [45, 99, 100], and spillover is considered as a possible path to achieving it.

A fully hydrogenated graphene would have stoichiometry CH, with 7.7 wt.% of hydrogen [45, 99–101], meeting the DOE goals. Even though the spillover of the H on graphitic surfaces was observed decades ago [40], it is still not well understood how an H binds to graphene, when it seems energetically more favorable to stay on the catalyst or even to remain in a molecular H_2 form in gas phase. To better understand the spillover mechanism, with the goal to optimize its kinetics, it is important to compare the relative energy states of the hydrogen in its (i) dihydrogen gas form, (ii) at the metal-catalyst, and (iii) on the receptor-substrate, Fig. 3.1 (left). The energy states available for H will depend on the degree of saturation, or substrate coverage.

Indeed, Cheng et al. [102, 103] have studied the dissociative chemisorption of molecular hydrogen and desorption of atomic hydrogen on Pt clusters, and concluded that the number of adsorbed H_2 increases with the increasing size of the cluster. Furthermore, they show that the binding strengths decrease with the increasing coverage that is, energy-states available for H raise, approximately representing the increase of

the chemical potential μ_H since the entropy contribution is less significant. They find that in low coverage the adsorption strengths are very large and at the saturation level are closer to the energies on a fully H-covered Pt (111) surface [102, 103]. In contrast, the strength of an H binding to sp^2-carbon receptor is shown to increase with the greater coverage, due to its clustering and CH-phase formation [100]. This analysis reconciles the weak binding of the H to the bare substrate in the spillover by stressing the role of nucleation of condensed CH phase, which must be forming in the process of spillover on a graphene-receptor, as it is more favorable than the H_2 molecule [100]. Previously, the catalyst per se was not considered, and the focus was on the variation of the hydrogen binding to the receptor and its thermodynamic comparison with gaseous H_2.

3.3 Hydrogen spillover model

The details of hydrogen binding to the catalyst particle are reported here, serving as a gateway to the entire process in which the catalyst saturation is also an important aspect of spillover. Combining – molecular dihydrogen gas phase, H dissolved on the catalyst, and H in the storage phase on the receptor – all the pieces, a conceptual qualitative schematic of spillover is drawn in Fig. 3.1. On the left, the blue line marks the energy of H in its molecular form; the additional broad (also blue) range is the chemical potential of H including the entropic contribution at different gas conditions. On the right side, a family of thin dark-blue lines corresponds to the energies of H bound to graphene, which vary with the size and the configuration of the cluster-island [100] and converge to the CH-phase energy. The mid-section pink block shows the range of energies of H at the catalyst as computed and analyzed below. The first H_2 molecule dissociates and binds to the catalyst rather strongly, and therefore μ_H lies

deep in this picture. However, the energies of the subsequent H_2 binding gradually decrease, raising the μ_H. For the spillover of an H to occur from the metal, the μ_H must exceed the CH state energy level shown by the gray line, before the metal cluster saturates (i.e., becomes unable to further accept new H_2 molecules).

The catalyst plays an important role in bringing the μ_H into this range. Possible metal-hydride phase formation imposes an additional constraint on the μ_H. The former must lie above the μ_H of the receptor, to avoid formation of metal-hydride before the spillover (assuming that the hydride-phase would inhibit the catalytic activity). In this work this model is validated by exploring, through *ab initio* computations, the gradual energy change of H on the catalyst, to reveal how it fits between the energy on the receptor and as free gas. Comparing these μ_H values identifies the range of chemical potential favorable for the spillover. The role of catalyst saturation and binding strength of H with the receptor in bringing the μ_H in this desirable range, is explored. Furthermore, to understand the first kinetic step, the barrier involved in the motion of an H atom from catalyst to receptor is computed and compared with the experimental observation.

3.4 Computational methods

The calculations are based on the density-functional method with all-electron projected augmented wave potentials [61, 104] and the generalized gradient approximation of the Perdew-Burke-Ernzerhof (PBE) [55] for exchange and correlation, as implemented in VASP [105–107]. Gamma point is used for Brillouin zone sampling. Conjugate gradient scheme is employed to relax the geometry until the forces on every atom are less than 0.005 eV/Å. Large vacuum spaces (~15 Å) are used in supercells to minimize any cell-cell spurious interactions. The migration barrier for an

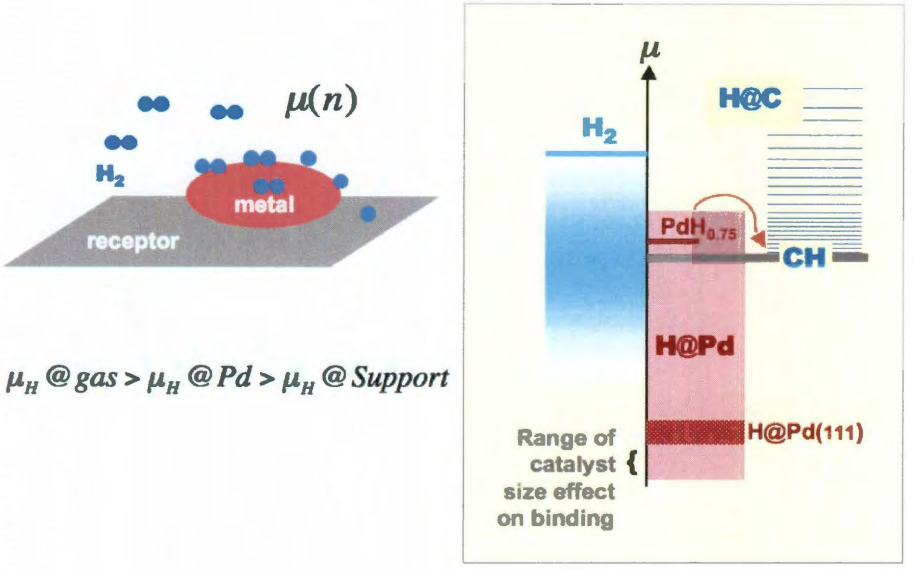

Figure 3.1 : Left: Schematics of spillover process in real space. The inequality shows the range of chemical potential favorable for spillover. Right: model of spillover in energy space displays the relative energy (chemical potential) of H in different states. The gray, dark-red, and blue lines show the μ_H in fully a hydrogenated graphene (CH), in metal hydride, and in the H_2 molecule, respectively. The pink and dark-red blocks show the range of energies of H at the catalyst and at the Pd (111) surface with the H coverage varying form 0.25 to 1 ML. The family of thin dark-blue lines corresponds to the energies of H bound to graphene.

H-atom is calculated using the nudged elastic band method [108].

3.5 Unsupported catalyst hydrogen saturation

In order to get the μ_{H} on the metal catalyst, hydrogen uptake process of a free unsupported cluster was performed. More specifically, a relatively small four-atom Ni and Pd clusters were considered as *catalysts* and a graphene with the H-terminated edge as *receptor*. The binding energy, as well as the chemical potential of H_2 on the metal cluster, will depend upon the number of H_2 attached and the relative positions of the H atoms. For example, the binding energy of the first H_2 on the cluster will differ from the next H_2 and so on. Addition of a H_2 molecule leads to gain in the incremental energy, which approximately represents the chemical potential μ_{H}, which is defined as

$$\mu_{\mathrm{H}} = [\Delta E(\mathrm{M}_n\mathrm{H}_m) - E(\mathrm{H}_2) - E(\mathrm{M}_n\mathrm{H}_{m-2})]/2, \tag{3.1}$$

where M_n is a metal-catalyst. A comparison of the $\mu_{\mathrm{H}}(m)$ in the metal cluster and in the receptor provides the number of H_2 molecules required to saturate the metal cluster sufficiently to permit the spillover onto the receptor.

The geometries of Pd_4 clusters are optimized and among the various structures, a tetrahedron is found to be the lowest in energy [109]. The magnetic moment (2 μ_B) and the Pd-Pd bond lengths (2.65 Å) in Pd_4 cluster, are in good agreement with the previous calculations [109] performed by using the hybrid B3LYP exchange correlation functional, which gives a better description of the transition metals. The comparison provides an independent test of the method accuracy. For the subsequent hydrogenation of the catalyst, several symmetrically non-equivalent adsorption sites for a H_2 molecule on the cluster are considered and their respective energies are

compared. The first H_2 dissociatively adsorbs on the Pd_4 cluster (essentially forming a hydride molecule). Among the various structures of the Pd_4H_2 there are two lowest energy configurations, as it was also observed in a previous calculation [109]. In one of the structures the dissociated H atoms cap the adjacent triangular faces of the Pd_4 cluster (Fig. 3.2a), while in the other they bridge the Pd-Pd edges, which do not have the common Pd atom.

The hydrogenation process continues by subsequently adding H_2 molecules, to the ground state structure (cluster+H_2), obtained from the previous optimization. From the second H_2 onwards, H_2 molecules do not fully dissociate, but rather bind to Pd_4 via Kubas [89] type of interaction, where the H-H bonds are elongated from 0.73 Å (as in molecular H_2) to $0.84 \sim 0.87$ Å. The hydrogenation was continued until the cluster stopped to adsorb any further H_2, i.e., no bound stable configuration could be found. The Pd_4 cluster saturates after adsorbing nine H_2 molecules. The optimized geometries of these clusters are shown in Fig. 3.2(a). The 10^{th} H_2 is repelled from the cluster and remains in the molecular form. This unattached H_2 lies more than 3.3 Å away from the atoms of the saturated cluster. The H-H bond length remains the same as in the molecular H_2, accompanied by almost no gain in binding energy, signaling the saturation of the cluster.

The incremental energies ΔE, which are plotted in the Fig. 3.2(b), never exceed the energy of an H on a pristine graphene (not shown in Fig. 3.2, and corresponding to the topmost thin line on the right side of Fig. 3.1). Hence, thermodynamically spillover cannot be easily initiated on a pristine graphene. The possibility cannot be completely excluded, because at higher temperature, due to fluctuations, some of the H atoms can move to the graphene. On the other hand, the incremental binding energies do exceed the chemical potential of H in hydrogenated phase, after the ad-

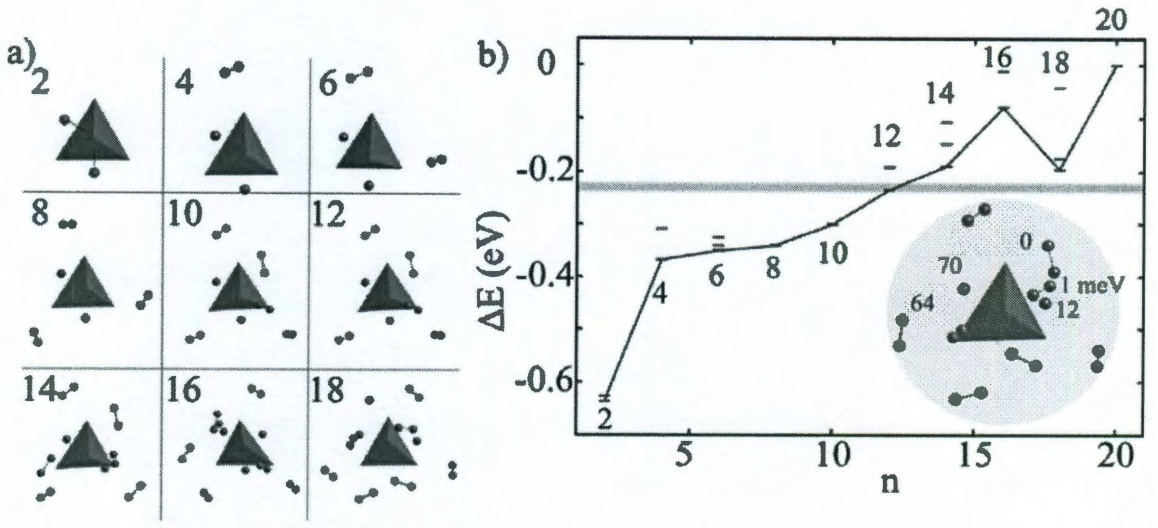

Figure 3.2 : (a) The optimized structures of $Pd_4H_n(n = 2$ to 18) clusters. (b) Plot of ΔE with the increasing number of H atoms. The gray dashes are the energies of other isomers. The horizontal gray line shows the μ_H in a fully hydrogenated graphene. Inset: the optimized geometry of a fully saturated Pd_4H_{18} cluster. The removal energies are given with respect to the energy (0) of the most stable H.

sorption of 6^{th} H_2 molecule as shown in Fig. 3.2(b) (the gray line corresponds to the thin gray line in Fig. 3.1, as well). Therefore, the spillover to the fully hydrogenated phase is indeed thermodynamically favorable after the catalyst has adsorbed six H_2 molecules.

In order to study the effect of different metal element catalysts on the spillover, we also carried out simulated hydrogenation of a Ni_4 cluster. The ground state geometry of the Ni_4 is also found to be a tetrahedron, with the Ni-Ni bond length of 2.60 Å and magnetic moment of 4 μ_B. The larger magnetic moment arises due to localized nature of the Ni $3d$ orbital. The Ni_4 adsorbs the first two H_2 molecules dissociatively. The cluster saturates after adsorbing the 10^{th} H_2 molecule. The incremental binding energy exceeds the chemical potential of H in hydrogenated phase, after the adsorption

of the 7^{th} H_2 (Fig. 3.3). Therefore, the effect of changing the metal from Pd to Ni essentially shifts the threshold of the spillover from the 6^{th} to $7^{th}H_2$, because of the more diffused nature of Pd 4*d* orbital compared with the Ni 3*d* orbital. The overall trend in the hydrogenation of the Ni_4 cluster remains similar to the Pd_4 (Fig. 3.3).

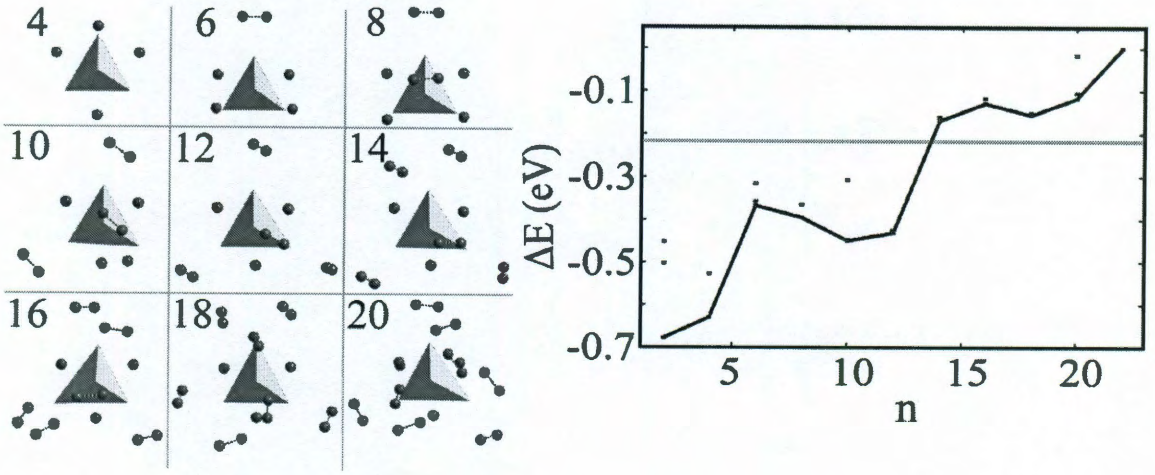

Figure 3.3 : (a) The optimized structures of Ni_4H_n (n =4 to 20) clusters. (b) Plot of of ΔE with the increasing number of H atoms. The gray dashes are the energies of other isomers. The horizontal gray line shows the μ_H in a fully hydrogenated graphene.

Although a small cluster is used to model the catalyst due to computational limitations, the qualitative conclusions on spillover are quite general. Although it is believed that the overall chemisorption behavior of the catalyst does not change much with increasing size [102], some additional complications may appear. Among them could be possible bulk metal-hydride phase formation. In order to assess this, the chemical potential of H in the Pd-hydride crystal ($PdH_{0.75}$) was separately calculated using standard periodic boundary conditions instead of the cluster approach.

The result is shown by the red line in Fig. 3.1, which lies ~60 meV above the gray CH-line. Hence, in the case of Pd the spillover will occur before formation

of hydride. The position of this line may vary for different metal catalysts, which is helpful in determining the best metal catalyst for spillover, and could be further tuned/optimized by alloying. We also calculate the adsorption energy of the H on Pd(111) surface, from 0.25 ML to 1 ML, shown by the red block in Fig. 3.1. The adsorption energy of 0.25 ML hydrogen is 0.57 eV, only slightly higher (~0.1 eV) than that in the Pd_4. Thus, with increasing cluster size the threshold of the spillover may decrease but not very significantly.

The justification of considering incremental energies as chemical potential (essentially an average quantity), depends on how large the variance is in the removal energies of the different H atoms from a saturated cluster/catalyst. The energy cost to remove an H from the cluster may in principle differ with the type/position of the removed atom. In order to evaluate this, we have calculated the removal energies of the 5-symmetrically non-equivalent H-atoms including Kubas and dissociated from a fully saturated Pd_4H_{18}, as shown in Fig. 3.2(b) (inset). The difference in removal energies of the five non-equivalent atoms lies within 70 meV, which is relatively small. This energy difference is within 15 % of the total range of chemical potential of H on a catalyst, and is reasonable enough to justify its use as a chemical potential. This difference is expected to decrease with the increasing size of the catalyst. Moreover, the bonding strengths of the Kubas type H atoms are similar to the dissociatively adsorbed H atoms, indicating that any atom could potentially participate in the spillover process, as long as μ_H of the system has reached high enough level at overall saturation.

The above analysis shows that it is energetically possible for spillover to occur from an unsupported metal cluster to a receptor. In experiments these clusters are supported on the substrate and hydrogen diffuses (or rather hops) from the catalyst to

the support/receptor. Note that the focus here is only the very first step – a diffusion hop from the catalyst to the receptor. This of course must be followed by H diffusion on carbon sites away from metal, which has been demonstrated to be reasonably fast [110]. In order to make this model closer to the experimental situation, the hydrogenation of a supported cluster on a receptor is studied next.

3.6 Supported catalyst hydrogen saturation

The pristine graphene was chosen as support as the C atoms in the vicinity of the catalyst might exhibit improved binding with the hydrogen. First, several non-equivalent sites for Pd_4 cluster on graphene have been optimized. After relaxation, however, most of the configurations converge to a structure where three corners of the tetrahedron lie above the centers of C-C bond, Fig. 3.4. There are two types of Pd-Pd bond with the bond lengths of 2.60 and 2.69 Å, whereas average Pd-C bond lengths are 2.30 Å. The binding energy and the total magnetic moment of the whole Pd_4 cluster on the graphene are 0.42 eV and 1 μ_B (reduced from the unsupported cluster), respectively.

The bonding of receptor and catalyst is analyzed by plotting the total, accumulation, and depletion of charges, shown in Fig. 3.4(b), (c), and (d), respectively. The accumulation/depletion of charges is obtained by subtracting the total charges of free Pd_4 cluster and graphene calculated independently, with the same atomic position, from the total charge of the Pd_4@graphene. The positive (negative) value of the isosurface represents the accumulated (depleted) charge regions. The total charge density shows some directionality of the C-Pd bond, nevertheless, the charges around Pd are diffused, a signature of a mixed covalent and metallic bonding, Fig. 3.4(b). Further evidence comes from the isosurfaces of accumulation and depletion, as the

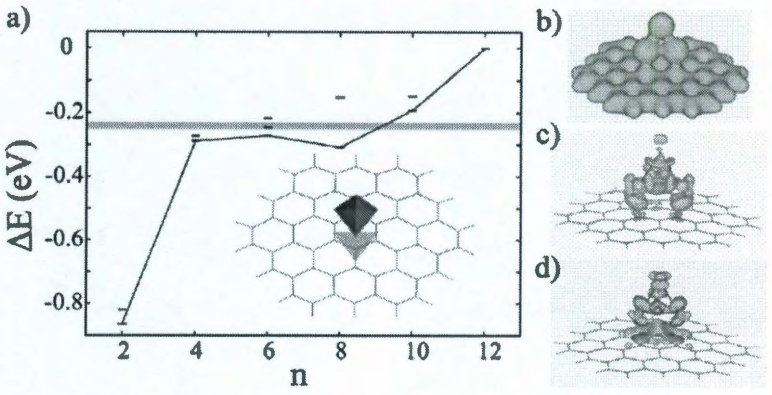

Figure 3.4 : (a) The plot of incremental energy ΔE vs. the number of H atoms on a supported cluster. Gray dashes are the energy of other isomers. Inset: the optimized geometry of Pd_4@graphene. The gray line shows the μ_H in a fully hydrogenated graphene. (b), (c), and (d) are the isosurfaces of the total, accumulation, and depletion of charges.

charge has been accumulated between the C-Pd bonds and depleted from the π-cloud of hexagonal ring in graphene, Fig. 3.4(c) and (d).

Next, the hydrogenation of this supported cluster was performed, following the same procedure as described above for the free cluster. Like the free cluster, the first H_2 is adsorbed dissociatively and subsequent ones bind via Kubas interaction [89]. The cluster saturates with five H_2 molecules, much sooner than the free cluster. As expected, the incremental adsorption energy never exceeds the energy of an H on pristine graphene. However, it does cross the level-line of C-H energy of a fully hydrogenated graphene after the adsorption of the 5^{th} H_2 molecule, hence, showing the thermodynamic possibility of the spillover. The onset of spillover occurs earlier than in the free cluster because the charge available for binding with the H_2 is now shared with the support material. This reduces the overall intake of H on the catalyst, with no harm to spillover.

3.7 Kinetics of the spillover

Having shown the possibility of the spillover from both free and supported cluster, the kinetics aspects can be explored, which essentially involves the motion of the H atom from the metal to the receptor. The likelihood of an H atom to hop from the catalyst to the pristine graphene substrate was tested in a computational experiment, by removing the H atom from the saturated catalyst and bringing it to the receptor. Upon relaxation, H goes back to the catalyst spontaneously. When the removed hydrogen is placed farther away from the catalyst, it remains attached but the whole process is endothermic by 2.5 eV, highlighting again the difficulty of spillover on pristine graphene. Similarly, it was tested the hopping of an H atom to the receptor in the vicinity of a fully hydrogenated graphene phase, which was represented by a hydrogenated ring-hexagon near the catalyst. In this case, the H-atom removed from the catalyst is more stable on the hydrogenated phase: unlike in pristine graphene case, the H does not come back to the catalyst, and the overall process becomes energetically favorable by 0.15 eV, making spillover possible on hydrogenated graphene.

Although it is more favorable for H to be in the hydrogenated phase than on the saturated catalyst, there are still barriers involved for the motion of the H. The migration barrier for H to move from the metal to CH-phase is calculated using the nudged elastic band method [108], Fig. 3.5. The barrier is $E_s = 0.68$ eV, which can be overcome even below the room temperature. Indeed, at $k_BT = 0.025$ eV the characteristic time τ of this step can be estimated from standard rate theory [111] as $\tau - 1 = (k_BT/h).exp(-E_s/k_BT)$. With the pre-factor $k_BT/h = 10^{13}\,\mathrm{s}^{-1}$, one obtains $\tau \approx 30\ ms$, which is a reasonably fast stage. Therefore, spillover is both thermodynamically favorable and kinetically feasible under the ambient conditions.

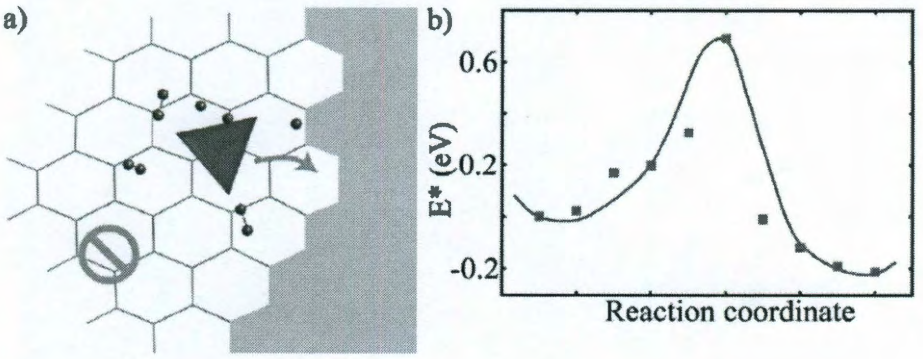

Figure 3.5 : (a) Fully relaxed cluster saturated with H, next to hydrogenated phase (gray area). (b) Plot of energies of intermediate images for the barrier calculation vs. the reaction coordinate.

3.8 Conclusions

In summary, the thermodynamic and kinetic plausibility of the spillover process was shown here. Energetically, it is possible for spillover of H to occur from a metal cluster to the hydrogenated graphene, both from the freestanding and receptor supported clusters. Importantly, the process does not require full saturation of the cluster, because thermodynamically the spillover becomes favorable even before a cluster saturates. Furthermore, it is energetically unfavorable for the spillover to occur on a pristine graphene surface, yet a phase of hydrogenated graphene facilitates the process by significantly improving the C-H binding. The migration barrier for hydrogen from the metal cluster to the hydrogenated phase is small, suggesting that the spillover can easily occur below room temperature. Moreover, this work provides possibly the first explanation of the nano-thermodynamics of spillover and also hints towards finding materials where it can be achieved more effectively. Along with the catalyst saturation, the optimum C-H bonding has emerged as an important factor for the spillover. Therefore, any modification of the receptor that leads to an increase in this energy

will also enhance the spillover (of course, within the reversibility limits).

Chapter 4

Fluorinated graphene: Patterning nanoroads and quantum dots

4.1 Opening the gap of graphene

After the first experimental evidence of graphene [18], research on its properties and applications has continued to grow with unprecedented pace. However, a great deal remains to be done to fully incorporate graphene's unique properties into electronic devices. The rapid advances in fabrication methods [20,21,112,113] have now made it possible to produce graphene on a large scale. The major obstacle to its application in electronic devices is the lack of a consistent method to open the zero band gap of graphene in a controlled fashion.

The use of graphene nanoribbons has been proposed as a way to tune graphenes electronic properties [114–116]. Depending upon their width and edge orientation, graphene nanoribbons can be either metallic or semiconducting [117–121]. Though there has been intensive research on nanoribbon fabrication, it is still difficult to obtain ribbons with well-defined edges (e.g., by chemical methods [116, 122, 123]) or to scale up its production (e.g., by carbon nanotube unzipping [124, 125]). Even a bottom-up approach [126] does not solve the challenge of assembling graphene nanoribbons into functional devices.

A recently explored alternative way to tune the band gap is to use a fully hydrogenated graphene [127] (also known as graphane [45]) as a matrix-host in which

graphene nanoroads [46] or quantum dots [42] are patterned. As is the case for graphene nanoribbons, the electronic properties of such roads and dots are width- and orientation-dependent. However, their biggest advantage over nanoribbons is that both semiconducting and metallic elements can be patterned and interconnected on the same graphene sheet, without compromising its mechanical integrity. This new approach has already been attempted experimentally [128] and has potential to quickly rival graphene ribbons.

The nanoroads and quantum dots can be patterned on any insulating functionalized graphene, e.g., graphane. The formation energy of graphane lies within a favorable and reversible range [100]. This reversibility is very important for applications such as hydrogen storage materials, and has been experimentally observed [129, 130]. However, a nucleation barrier exists in the initial steps of hydrogenation of graphene and it is desirable to find a similar or even more favorable element which can transform graphene into a semiconducting material.

4.2 Fluorination of graphene

The functionalization of graphene by fluorine, explored here, results in compositions similar to Teflon – $(CF_2)_n$–, which in a 2-dimensional incarnation corresponds to – $(CF)_n$. The biggest advantage of fluorination of graphene comes from the shear availability of experimental and theoretical research that has been done on fluorinated graphite [131–142] and fluorinated carbon nanotubes [143–148]. This knowledge base can help devise ways of controllable fluorination of graphene. Depending on the experimental conditions and reactant gases, different stoichiometries (e.g., $(CF)_n$ [149], $(C_2F)_n$ [132], and $(C_4F)_n$ [150]) can be obtained.

Therefore, unlike hydrogenation, fluorination can offer several promising function-

alized phases to serve as host materials for graphene nanoroads and quantum dots. Hence, the wide range of possible chemical reactions involving fluorinated graphitic materials, in combination with possibility of tunable electronic properties of patterned graphene structures, opens the door to a range of exciting applications.

A comparative study of the formation of CF, C_2F, and C_4F by chemisorption of F atoms on graphene is carried out using *ab initio* density functional theory (DFT) methods, Fig. 4.1. Based on the formation energies, CF is the most favorable, and its formation does not have a nucleation barrier, in contrast to the barrier observed for the formation of graphane. Going further, nanoroads and quantum dots of graphene are patterned on these substrates and show tunable electronic and magnetic properties, offering a possibility to a variety of applications.

4.3 Calculation methods

Ab initio methods are used to calculate the smallest system, as in the case of fluorinated graphene nucleation, nanoroads, and the smallest quantum dots. Besides the higher accuracy of the results, this allows a direct comparison with previous first principles calculations of graphane nucleation [100] and patterning of hydrogenated graphene [42, 46]. The calculations were carried out using *ab initio* density functional theory, as implemented in the Vienna *ab initio* package simulation (VASP) [105, 107]. Spin polarized calculations were performed using the projected augmented wave (PAW) method [61, 104] and Perdew-Burke-Ernzerhof (PBE) [55] approximation for the exchange and correlation, with plane wave kinetic energy cutoff of 400 eV. Periodic boundary conditions were used, and the system was considered optimized when the residual forces were less than 0.005 eV/Å. The unit cells lengths of C_xF_y and nanoroads were fully optimized. The Brillouin zone integrations were

carried out using a $15 \times 15 \times 1$ Monkhorst-Pack k-grid for the C_xF_y, $1 \times 1 \times 5$ for the nanoroads, and at the Γ-point for the clusters.

For the quantum dots, the total energies for $n = 1 - 384$ were calculated using a density functional based tight-binding method (DF-TB) with the corresponding Slater-Koster parameters [151], as implemented in the DFTB$^+$ code [152]. Initially several non-equivalent geometries were tested for the smallest dots ($n < 7$) and the lowest energy structures were generally derived from $n - 1$ structures. The DF-TB results were tested by comparing the formation energies of the smaller dots ($n = 1 - 24$) on a finite fully fluorinated graphene cluster ($C_{54}F_{72}$) by DFT calculations (as described above). To mimic an infinite sp^3 CF, the edge C atoms of the cluster were passivated with two F atoms and kept constrained during the simulation of the dots. In all calculations sufficient vacuum space was kept between the periodic images to avoid spurious interactions.

4.4 Structure and electronic properties

The structure of the fluorinated graphite, based on X-ray diffraction results, has long been believed to consist of trans-linked cyclohexane chairs of fluoridated sp^3 carbon [131, 132, 139, 140]. Such a structure was later confirmed by DFT calculations [47], and it is the one used here to represent CF, Fig. 4.1(a). There are two possible stacking sequences for $(C_2F)_n$: AB/A′B′ and AA′/AA′ [132, 136], where the prime and slash indicate a mirror symmetry and the presence of covalently bonded fluorine atoms, respectively. Both AB, Fig. 4.1(b), and AA′ (not shown) are analyzed here. Furthermore, the structures of single-sided, Fig. 4.1(c), and double-sided fluorinated C_4F [141, 150] are also examined.

Considering the fluorination to occur through the simple reaction x C$+y/2$ F$_2 \longrightarrow$

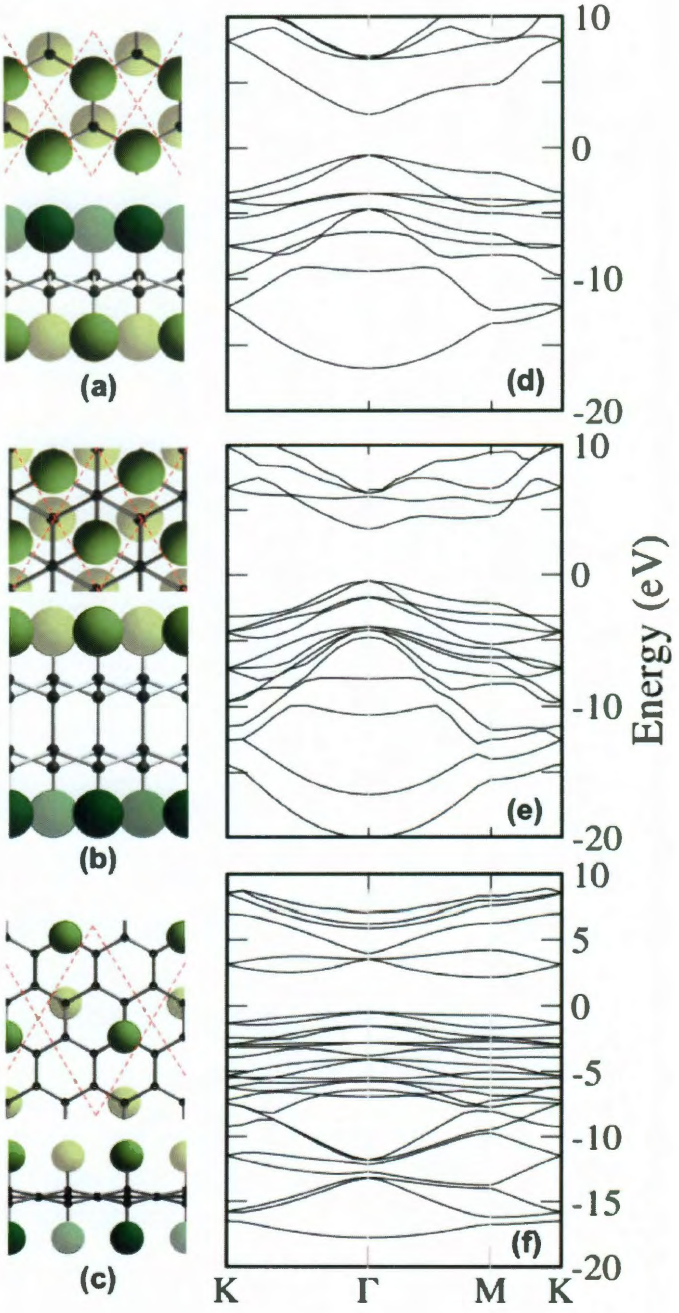

Figure 4.1 : The atomic structures (darker atoms are closer; red dashed lines mark the unit cells) of (a) CF, (b) C_2F for AB stacking, and (c) C_4F for double-sided fluorination, and (d)–(f) the corresponding electronic band structures. CF and C_2F AB have a direct band gap at the Γ-point, 3.12 eV and 3.99 eV, respectively, whereas C_4F has an indirect band gap of 2.94 eV.

Table 4.1 : Formation energy (E_f), band gap (E_g), equilibrium lattice parameter (d_0), and bond lengths of the fluorinated graphene at different coverage.

	E_f, eV/atom	E_g, eV	C-F, Å	C-C, Å	d_0, Å
CF	-1.615	3.12	1.38	1.58	2.61
C_2F AB	-1.508	3.99	1.38	1.56	2.55
C_2F AA′	-1.468	3.97	1.38	1.56	2.55
C_4F single-sided	-1.100	2.93	1.45	1.51^a / 1.40^b	2.48
C_4F double-sided	-1.095	2.68	1.48	1.50^a / 1.40^b	2.49

a] Bond length between sp^3 and sp^2 C atoms, and b] between two sp^2 C atoms.

C_xF_y, the formation energies (E_f) of these four structures were calculated, Table 4.1,

$$E_f = \frac{1}{y}(E_{C_xF_y} - x\ E_C - y/2\ E_{F_2}) \tag{4.1}$$

where $E_{C_xF_y}$ is the energy of C_xF_y, E_C and E_{F_2} are the energies of a C atom on graphene and F_2, respectively, and x and y are the number of C and F atoms, respectively. The formation of CF is more favorable than C_2F and C_4F. The formation energy decreases with increasing F coverage. For C_2F, AB stacking is energetically more favorable than AA′. The formation energies for C_4F with single- and double-sided fluorination are very similar, within the error of the calculation.

The length of the C-F bond in molecular species is 1.47 Å, and the C-F bond strength is partially attributed to its highly polarized nature. As a result, fluorocarbons have been widely explored in organic chemistry for a variety of applications [135, 153–155]. The calculated C-F bond lengths in CF and C_2F are 1.38 Å in each case and agree well with both experimental (1.41 Å) [136, 140] and theoretical (1.37 Å) [47] values. C_4F shows a much longer C-F bond length (1.45 Å for single-

sided fluorination), closer to the C-F bond in molecular species. The computed C-C bond lengths in CF are also in good agreement with both experimental (1.53 Å) [136] and theoretical (1.55 Å) [47,156] values. The resulting lattice mismatch with graphene (d_0 = 2.47 Å) increases with increasing fluorine content. CF has the largest lattice mismatch, 5.7 %, followed by C_2F, 3.2 %, and C_4F, between 0.4 % (for single-sided coverage) and 0.8 % (for double-sided coverage).

Graphene's gapless electronic structure changes completely after fluorination. A finite gap appears in the electronic band structure of CF, C_2F, and C_4F (Figs. 4.1(d)–1(f), respectively), transforming them into wide band gap semiconductors. The electronic band structure of CF shows a 3.12 eV direct band gap at the Γ-point, agreeing well with previously reported values [3,47,150]. The band gaps of C_2F for both stacking sequences are very similar, which is as expected due to the similarities in their structures. Recent experiments on graphene fluorination yielded an optically transparent C_4F with a 2.93 eV calculated band gap [150]. Here, the calculated band gap for the single-sided fluorinated C_4F is 2.93 eV, a little larger than for the double-sided fluorinated C_4F, 2.68 eV.

4.5 Formation of fluorinated graphene

The initial steps of graphene fluorination can be studied by incrementally adding n F atoms to different positions of a $C_{54}H_{18}$ cluster and calculating the formation energy,

$$E_f(n) = E_{C_{54}H_{18}F_n} - \frac{1}{2} n E_{F_2} - E_{C_{54}H_{18}}, \tag{4.2}$$

where $E_{C_{54}H_{18}}$ is the energy of the $C_{54}H_{18}$ cluster with hydrogenated edges and $E_{C_{54}H_{18}F_n}$ the energy when n F atoms are adsorbed on the cluster. In an aromatic system the π-electrons form pairs between C atoms from different subgroups, starred

and un-starred [157]. The adsorption of an odd number of F atoms leaves one unpaired π-electron in the aromatic system. This is exemplified by E_f of a single F atom, which is 0.45 eV/F lower than 1/2 E_{F_2} (the reference zero on the graphic in Fig. 4.2(a). Notably, F attachment is immediately exothermic, in contrast to hydrogenation where H binding is initially an endothermic process ($\sim$1.5 eV, relative to molecular H_2), causing significant nucleation barrier to the formation of the graphane phases.

Thus, graphene clusters with an odd number of π-electrons are energetically unfavorable and have higher E_f, as shown in Fig. 4.2(a) for $n = 1$, 3, and 5. For a pair of fluorine atoms there are six different positions (single- and double-sided fluorination, on ortho, meta, and para sites) where they can be added on a ring, Fig. 4.2(b). The meta configuration yields the highest E_f because the F atoms bind to C atoms from the same subgroup, therefore creating two unfavorable radicals. Placing the second F atom on the opposite side in the ortho-configuration results in a lower E_f; the value is 1.17 eV/atom lower than 1/2 E_{F_2}, which is as expected since the radical on the adjacent C atom is completely passivated.

Adsorption of an F atom transforms the hybridization of the host C atom from sp^2 to sp^3. As a result of this, the bond between the sp^3 and sp^2 carbon atoms becomes elongated, which leads to strain in the structure and an out of plain buckling of the fluorinated C atom. By adding a second F atom on the opposite side, the induced strains compensate one another further lowering the total energy, Fig. 4.2(c). The E_f decreases with increasing F content and approaches asymptotically to $E_f(\infty)$, which is equal to the formation energy of a fully fluorinated infinite graphene sheet.

According to the definition of the formation energy, fluorination of the graphene is favorable when $E_f(n) < 1/2\ E_{F_2}$. In the case of the analogous structure of graphane,

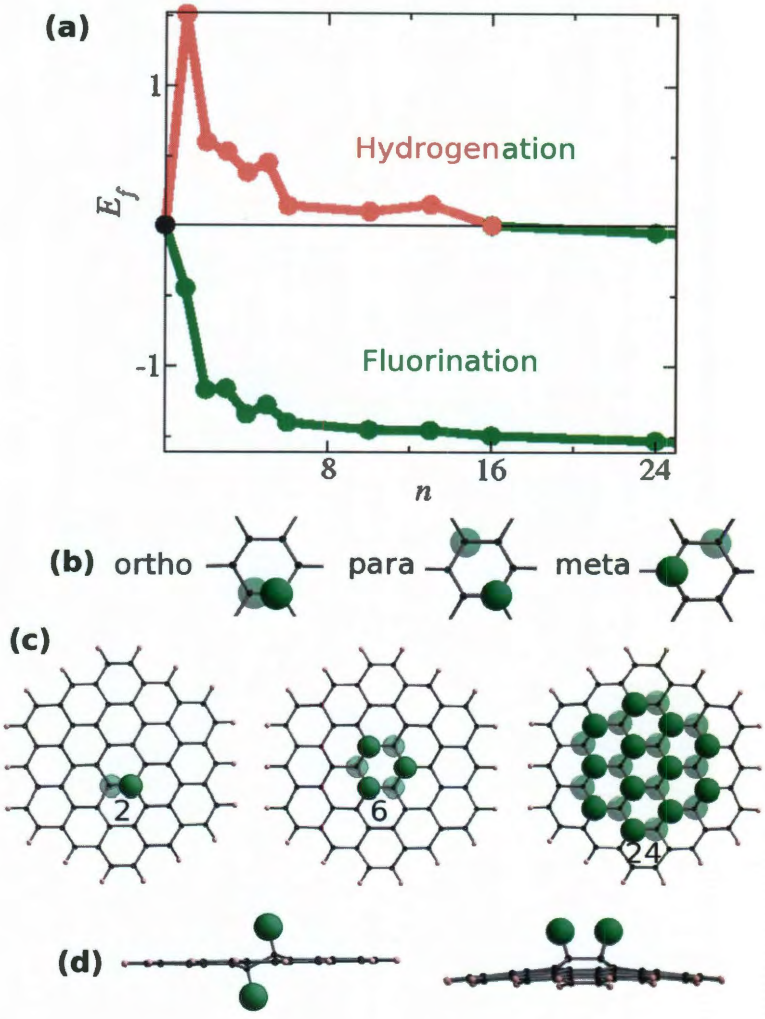

Figure 4.2 : Chemisorption behavior of F atoms on graphene. (a) The formation energy E_f is negative and further decreases with the number of F atoms n, without a nucleation barrier, in contrast to what is observed for hydrogenation. From the initial six positions for the F atom to adsorb (b), an ortho opposite-sided fluorination is lowest in energy, which ultimately results in a preference for aromatic magic cluster structures, as illustrated in (c). (d) Example of the lattice strain due to change in hybridization.

the formation energy is lower than $1/2\ E_{H_2}$ only after the formation of a stable nucleus formed by adsorption of 24 hydrogen atoms [100]. Since the C-F bond is stronger than the C-H bond and the F-F bond in F_2 is much weaker than the H-H bond in H_2, fluorination of the graphene is more favorable than its hydrogenation. In fact, $E_f(n)$ is always lower than $1/2\ E_{F_2}$. Therefore, unlike graphane, fluorinated graphene does not have a nucleation barrier to its formation and should be more stable and easily obtained than graphane.

4.6 Graphene nanoroads on CF

The patterning of nanoroads (NR′) and quantum dots on fluorinated graphene (FG) is investigated here in order to explore the possibility of combining metallic and semiconducting properties on the same sheet. Graphene nanoroads were formed by removing F atoms from a fully fluorinated graphene either along armchair (AC) dimers (N_{ac}) or zigzag (ZZ) chains (N_{zz}) to form pristine graphene roads, Figs. 4.3(a) and 4.3(b). After geometrical optimization, the AC nanoroad (AC-FGNR′) remains flat whereas the ZZ nanoroad (ZZ-FGNR′) is tilted. This tilting is a geometrical consequence of the position of the F atoms along the road being alternated in and out of the plane.

The AC-FGNR′ are semiconducting with large band gaps due to quantum confinement, Fig. 4.3(c). The band gap behavior can be divided into three hierarchical families for $N_{ac} = 3p$, $3p + 1$, and $3p + 2$, where p is a positive integer. For the AC orientation, the band gaps do not follow a monotonic trend with the width, and instead $\Delta_{N_{ac}=3p+2} < \Delta_{N_{ac}=3p+1} < \Delta_{N_{ac}=3p}$ (except for $N_{ac} = 3$ and 4). This trend is different from that observed for armchair nanoribbons [118], but is similar to that for graphane nanoroads [46]. The band gap energies are not affected by increasing the distance between the roads by adding additional chains of fluorinated graphene.

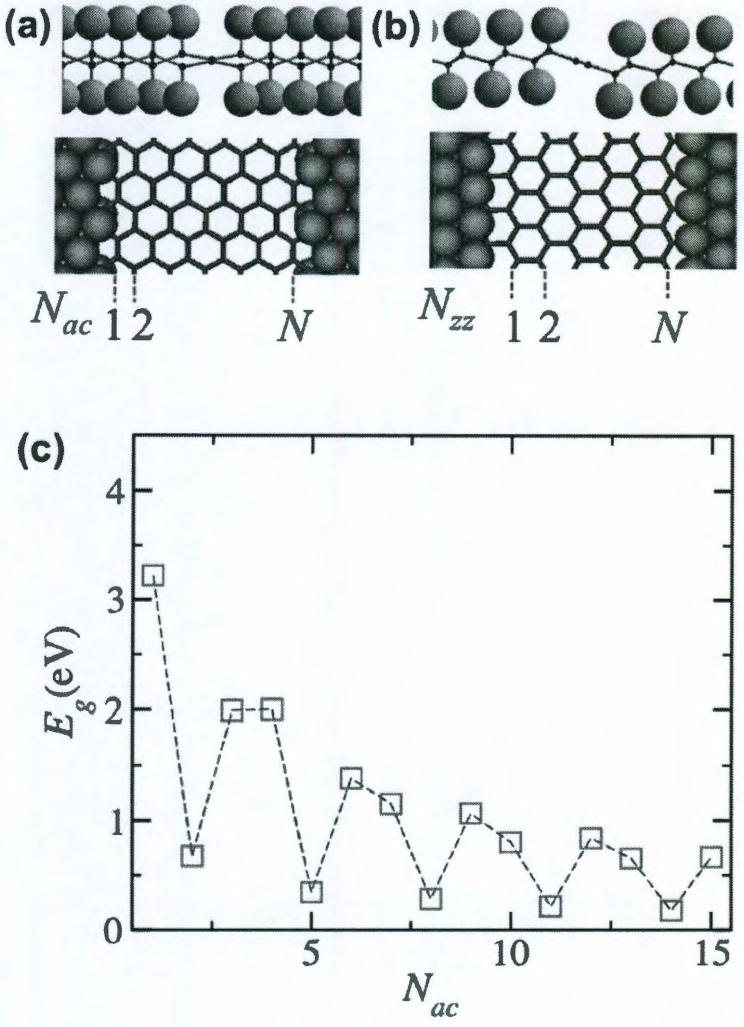

Figure 4.3 : Schematic illustrations of (a) armchair (AC), where N_{ac} is the number of sp^2 C dimer lines and (b) zigzag (ZZ), N_{zz} is the number of sp^2 C chains, roads. (c) For AC-FGNR′, the band gap E_g energy varies with the road width N_{ac}.

Thus the AC-FGNR′ are also well isolated from their lateral periodic images.

The electronic properties for the ZZ-FGNR′ depend strongly on the magnetic states of the system. It can be observed that the antiferromagnetic ZZ-FGNR′ are semiconducting, whereas the ferromagnetic ZZ-FGNR′ are semi-metallic. Very narrow nanoroads on graphane were found to be nonmagnetic, with a very small gap, and two bands near the Fermi level that do not cross. In contrast, narrow ZZ-FGNR′ have larger band gaps, for example E_g is 0.71 eV for $N_{zz} = 1$ and 0.56 eV for $N_{zz} = 2$. This difference may be due to the larger lattice mismatch between the fluorinated and pristine graphene. The states with antiferromagnetic spin distribution are lower in energy than the ferromagnetic, which can be used for spintronic applications.

For ZZ-FGNR′, the band gap energy increases with decreasing width, Fig. 4.4(a), due to quantum confinement. The band gap is inversely proportional to the width N_{zz}, which is similar to the dependence observed for nanoribbons [118, 158] or graphene with periodically adsorbed hydrogen chains [159], showing the best fit for $E_g(N_{zz}) = 4.47/(5.69 + N_{zz})$ eV. There are only two bands which cross near the Fermi level of the ZZ-FGNR′. The plot of their corresponding band-decomposed charge densities in Figs. 4.4(b) and 4.4(c) and shows that the π-bands formed by the overlap of p_z orbitals are mostly localized on the C atoms at the sp^2–sp^3 interface.

4.7 Graphene quantum dots on CF and C_4F

Experimentally, graphene quantum dots are obtained by cutting tiny pieces of graphene into different shapes; however, the problem of how to tune graphenes band gap still persists. The approach here is to consider quantum dots as small islands of graphene created by the removal of the F atoms from CF and C_4F. Their thermodynamic feasibility is studied by analyzing several possible configurations and exploring how

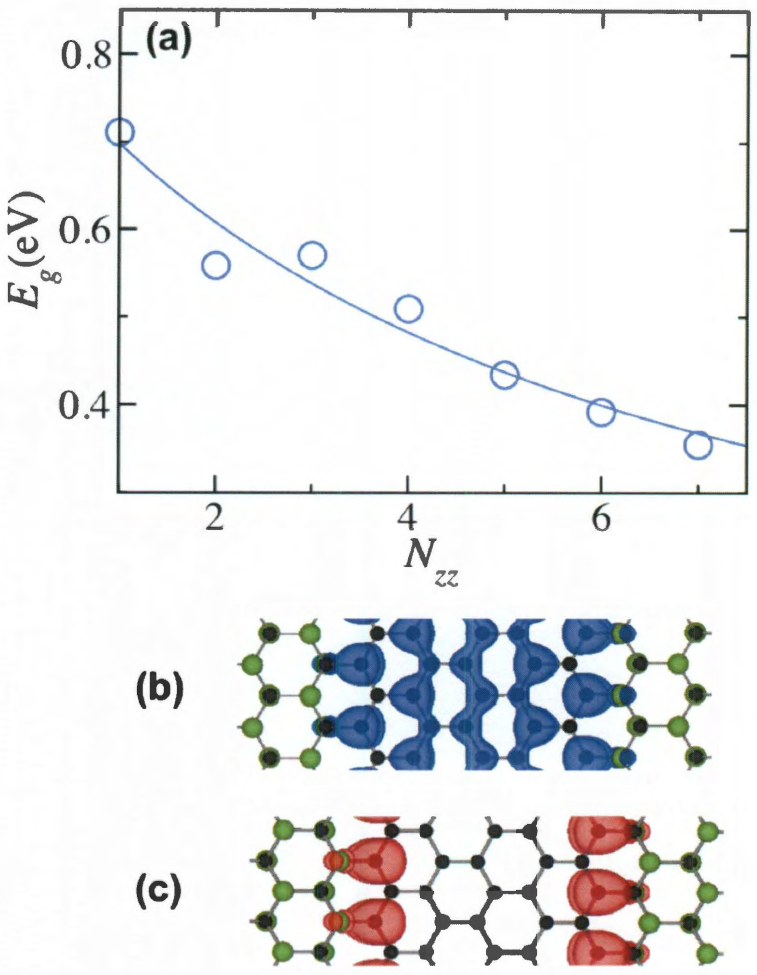

Figure 4.4 : (a) Plot showing the decrease in band gap with increasing width of the road for ZZ-FGNR′. The band-decomposed charge densities (3×10^{-3} Å^{-3}) for the 5-ZZ-FGNR′, corresponding to the top of the valence band (b) and the bottom of the conduction band (c).

quantum confinement affects their electronic properties. The removal of the F atoms yields graphitic islands of connected n sp^2 C atoms on a fully fluorinated graphene finite cluster or infinite sheet. For $(C_xF)_n \longrightarrow (C_xF)_{N-n}C_n + n/2\ F_2$, the formation energy is calculated as

$$E_f(n) = \frac{1}{n}[E_{sys}(n) - n\,\mu_F - N\,\mu_{CF}], \tag{4.3}$$

where E_{sys} is the total energy of quantum dots on the fluorinated graphene, and $\mu_F(= 1/2\ E_{F_2})$ and μ_{CF} are the chemical potentials of fluorine and CF, respectively. The removal of one F atom introduces an additional π radical on the C atoms; this is the inverse of F adsorption on graphene shown in section 4.5.

Formation of dots with lower $E_f(n)$ is more favorable and, overall, the formation energy of quantum dots decreases with increasing size of the dots. This trend can be observed by both DFT and DF-TB for dots carved on CF, Fig. 4.5(a). Larger dots can be studied using DF-TB, and upon their inclusion a clear trend, where $E(n) - E(\infty) \sim \text{const}/\sqrt{n}$, can be observed, Fig. 4.5(b). The quantum dots with the lowest formation energies are those in which the structure restores the aromaticity of the graphene, for example $n = 6$, 10, 16, and 24, Fig. 4.5(c).

The realization of quantum confinement promises many exciting applications like quantum computing [160, 161], single-electron transistors [162], and optoelectronics. The band gap is important for optical applications, but DFT and DF-TB calculations generally underestimate its value. The DF-TB band gaps at the Γ-point for $n = 6$ (3.28 eV) and 24 (2.44 eV) agree well with the HOMO-LUMO gaps calculated by DFT (3.37 and 2.47 eV for $n = 6$ and 24, respectively), therefore lending additional credibility to the DF-TB method employed. Although it is computationally prohibitive to calculate the precise band gaps of large systems ($n > 24$), these will most probably be within the optical range of ~1–3 eV.

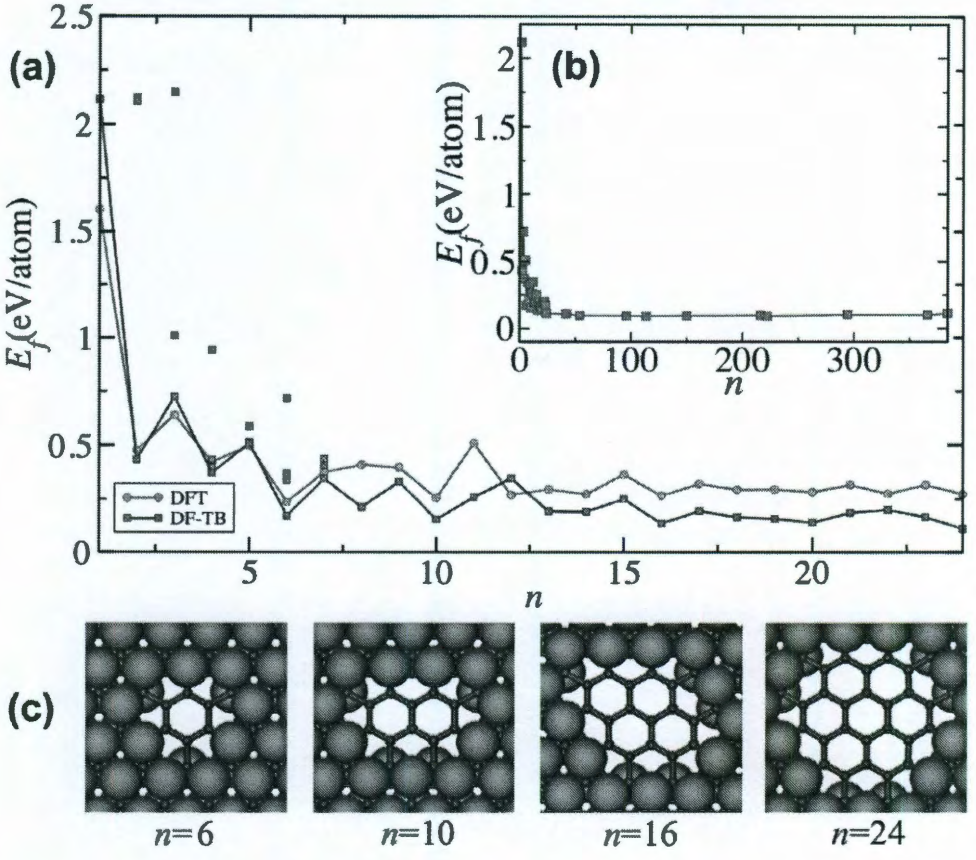

Figure 4.5 : (a) Formation energy $E_f(n)$ for different sizes of quantum dots calculated by DFT and DF-TB. (b) Overall, $E(n) - E(\infty) \sim \text{const}/\sqrt{n}$, using DF-TB. (c) Examples of aromatic quantum dots.

There is a reduction in quantum confinement with increasing size of the dots, hence reducing the band gap energy as their electronic properties approach those of graphene. Larger dots can be divided into AC and ZZ edges (examples shown in the inset in Fig. 4.6). Interestingly, plots of their band gaps show that dots with AC edges have larger band gaps than those with ZZ edges (Fig. 4.6). A least squares fit also shows the different trends for AC and ZZ edges; $E_g(n) = 14.1\,n^{-1/2+0.01}$ eV for AC edges and $E_g(n) = 19.4\,n^{-1/2-0.14}$ eV for ZZ edges. Different from conventional quantum dots, which follow a $\sim 1/R^2$ dependence, the observed trend is closer in behavior to the $1/R$ confinement of Dirac fermions [163,164], where $R \sim \sqrt{n}$.

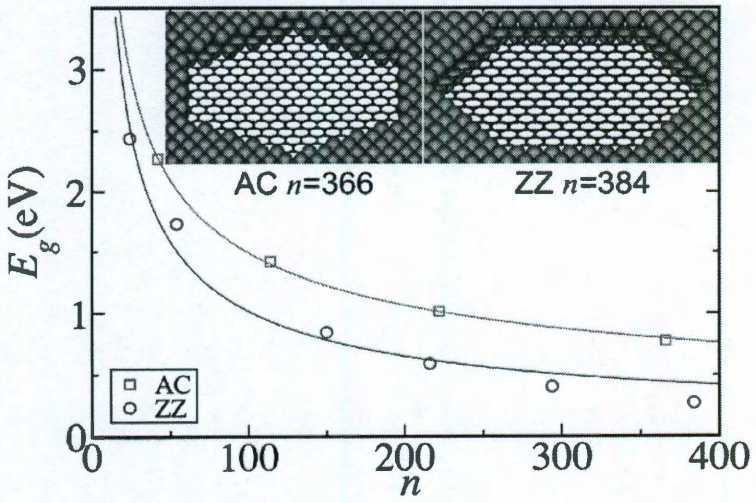

Figure 4.6 : Plots showing how the energy of the band gap for dots with AC and ZZ edges decreases with their size. Inset: Configurations of the largest optimized quantum dots.

Recently synthesized fluorinated graphene films were found to be optically transparent at the C_4F saturation level [150]. Next, two examples of 2-D quantum dot arrays are studied, as this is the way they are usually assembled for optical applica-

tions. A graphene patch designed as coronene is carved on a 7×7 hexagonal supercell of CF ($n = 24$) and on a 4×4 hexagonal supercell of C_4F ($n = 6$). All dots were separated by at least 10 Å.

The band-decomposed electron densities of the dots show atom-like states for CF and C_4F. The band gaps of the arrays are very similar to the ones obtained for the isolated dots, 2.50 eV for CF and 0.88 eV for C_4F. The nearly dispersionless bands for the dot on CF at the top of the valence band and at the bottom of the conduction band, Fig. 7(a), show a very good quantum confinement, with just a very small charge density leakage into the fluorinated graphene. In fact, the electronic state of the quantum dots on CF seems to be somehow more confined than on similar dots on graphane [42] due to the insulator character, which comes from the charge transfer from C to F in CF. The array of C_4F also shows localized charge density states, Fig. 7(b), with a non-hexagonal shape. The difference between the shape of the dots results from the more open structure of C_4F. Thus both CF and C_4F can be used for patterning quantum dots and, most importantly, the differences in fluorine coverage on graphene can be also used to tune the band gap.

4.8 Conclusions

In summary, gapless graphene can be altered by its patterned fluorination. Such fluorination results in wide band gap semiconductors (CF, C_2F, and C_4F), where higher F coverage is favored. Fluorination of graphene was found to be different from its hydrogenation, as it occurs without a nucleation barrier owing to the higher affinity of F towards C. Furthermore, the suitability of CF as a host material for graphene nanoroads and quantum dots has been demonstrated.

Nanoroads and quantum dots were found to exhibit orientation-, width-, and

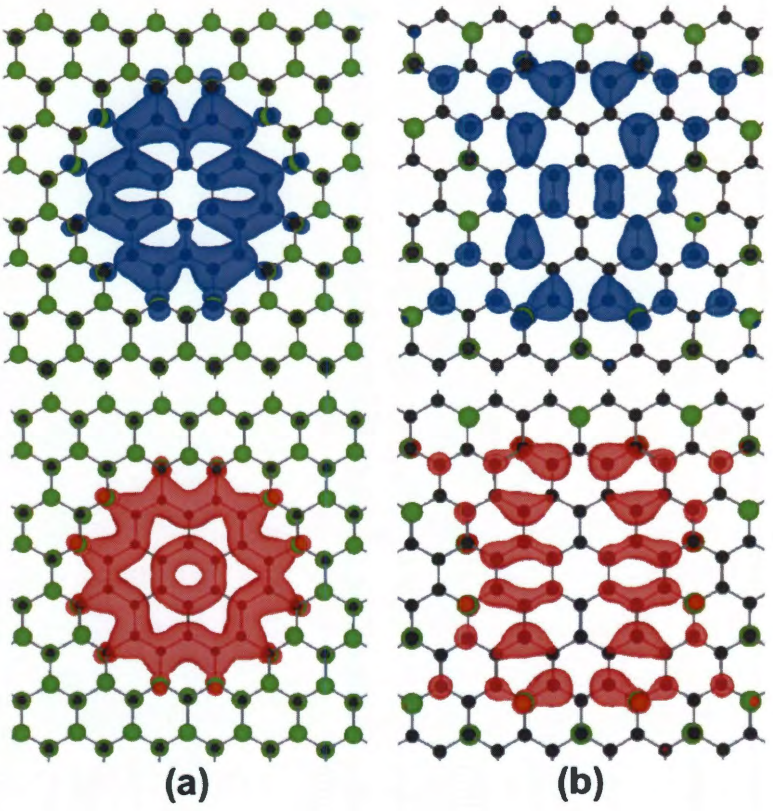

Figure 4.7 : Isosurfaces of band-decomposed charge densities (1.5×10^{-4} Å^{-3}) at the top of the valence band (upper figures in blue) and at the bottom of the conduction band (lower figures in red) for 2-D quantum dot arrays on (a) CF for $n = 24$, and C_4F for (b) $n = 6$.

F coverage-dependent electronic properties. Fluorinated graphene nanoroads with AC orientation are semiconducting with large band gaps, following a non-monotonic variation. The nanoroads with ZZ edge are semiconducting or semi-metallic according to their spin orientation; antiferromagnetic or ferromagnetic, respectively. The band gaps in ZZ roads vary as $\sim 1/N_{zz}$. The formation energy of the quantum dots depends on their size as $E(n) - E(\infty) \sim \text{const}/\sqrt{n}$. The band gaps of the larger quantum dots follow a $1/R$ trend similar to the confinement of Dirac fermions, where $R \sim \sqrt{n}$. The band-decomposed electron densities of 2-D quantum dot arrays in CF and C_4F show atom-like states with very good electron confinement.

4.9 Afterwords

It is important to mention that as in the case of any chemical attack [165], fluorination can cause some defects and the degree of such damage will depend on the specific conditions (source of F, temperature, etc.). Another uncertainty is due to the possible coexistence of different configurations (chair, boat, etc.), which is not within the scope of this study. The emphasis here is simple: Most of these fluorinated graphene phases have a sizable gap, and therefore can serve as a host matrix for confined nearly-metallic domains of pristine carbon.

It will be important to further explore the interface and to learn how to avoid possible frustration [166] which may destroy the interfaces and the clear picture of confinement, calling for further careful studies. One can speculate that possible experimental approaches fall into two classes: Either one can mask certain areas prior to exposing them to fluorination, or start from fully fluorinated graphene and then attempt a local removal of F (say, with focused ion beam of not too high an energy).

Furthermore, after the completion of this work, an experimental evidence of stoi-

chiometric fluorinated graphene was reported [167]. The authors report that the CF phase is indeed more stable that graphane, further corroborating the work presented here.

Chapter 5

Nanotube nucleation versus carbon-catalyst adhesion

5.1 Introduction

Despite key experimental advances to produce longer carbon nanotubes (CNTs) [168, 169], with more uniform diameter distribution [27–30] and at lower temperatures [170–173], the mechanism of single-wall carbon nanotubes (SWNT) growth at the atomic level is far from being completely understood. It is still not known how to fully control SWNT growth or even if such control can be achieved. Meanwhile, complete utilization of SWNT remarkable electronic properties awaits this scientific and technological achievement.

Experimentally, transmission electron microscopy *in situ* observations allow one to see the nucleation and growth of SWNT in some detail [174–176]. However, processes such as feedstock decomposition on catalyst surface, C diffusion on or through the catalyst and C incorporation into the nanotube wall cannot be seen directly. Fortunately, these details, which are key parts of the SWNT growth mechanism, can be explored using molecular dynamics (MD) simulations [75, 177, 178]. Recently developed dislocation theory of nanotube growth [179] transforms the principles of crystal step-flow to the lower-dimension of a tube edge; it enables quantitative predictions of growth rate of individual SWNT, yet does not address at all the complementary and important stages of nucleation.

The cap lift-off versus catalyst encapsulation is the to be or not question in the SWNT formation and has been studied extensively by theoretical methods, including *ab initio* [180–182], tight-binding MD (TBMD) [183, 184] or tight-binding Monte Carlo [185,186] simulations, and classical MD simulations [75,177,178,187]. *Ab initio* based MD is the most time consuming method and is only able to simulate small carbon-metal systems for a few picoseconds [180–182]. TBMD is an intermediary expensive method; it is hundreds of times faster than *ab initio* DFT based MD and can be used to simulate CNT growth in a reasonable time period (e.g., 100 ps) [183,184]. Classical MD simulations are two and three orders of magnitude faster than TBMD and therefore can be applied to large systems (up to 1000 atoms) and perform very long trajectories of up to 100 ns [173,178].

In the often referred to phenomenological vapor-liquid-solid model (Fig. 5.1), a complete CNT growth process is divided into three successive stages: Cap nucleation, cap lift-off as a short tube, and SWNT lengthening [175,188–190]. Detrimental to growth, catalyst encapsulation prevents feedstock from accessing the catalyst, a phenomenon known as catalyst poisoning, hindering cap lift-off and growth. Thus avoiding catalyst encapsulation during both nucleation and growth stages is critical for SWNT growth.

An exhaustive theoretical study is presented here aiming to elucidate the role of work of adhesion (W_{ad}) between graphitic cap and catalyst, temperature, and C diffusion in catalyst encapsulation (or poisoning) at the nucleation stage. Statistics over more than 500 MD simulations clearly show that the work of adhesion controls the high temperature region, in which the C mobility is sufficiently high, while slow C diffusion may result in an encapsulated catalyst at low temperature. Also it is suggested that room temperature growth of CNT is possible if the work of adhesion

could be significantly reduced through careful selection of the catalyst.

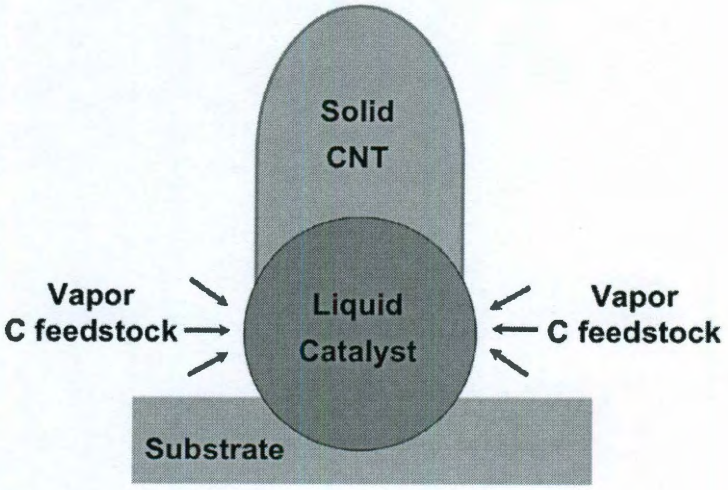

Figure 5.1 : Schematic diagram of the phenomenological vapor-liquid-solid model.

5.2 Driving force behind cap lift-off

Until now, three different aspects of the cap lift-off versus catalyst encapsulation have been distinguished and discussed: Adhesion versus curvature energy balance [191], decohesion by thermal kinetic energy model [192,193], and requirement of fast C diffusion [177,187]. A diagram showing the temperature dependence of catalyst encapsulation as a function of work of adhesion, W_{ad}, was constructed in order to compare and evaluate these three models, Fig. 5.2.

5.2.1 Curvature energy model

This model considers the energy difference between a growing tube and an encapsulated catalyst [191]. For small catalysts (diameter smaller than 3 nm), a growing SWNT is energetically favorable if the work of adhesion between the fullerene and

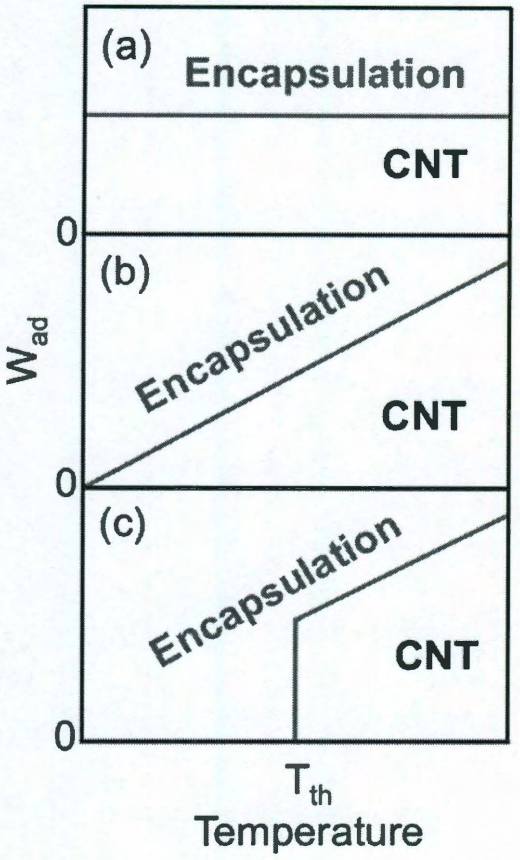

Figure 5.2 : Temperature dependence of SWNT growth/catalyst encapsulation as a function of work of adhesion has distinct characteristics for (a) curvature-energy, (b) thermal decohesion, and (c) fast C diffusion models.

catalyst particle is less than the curvature energy difference between the SWNT and the fullerene.

$$W_{ad,cF} < E_{cF} - E_{cT}, \tag{5.1}$$

where W_{ad} is the work of adhesion, and E_{cF} and E_{cT} are the curvature energy of the fullerene and SWNT, respectively. Inequality 5.1 shows that catalyst encapsulation happens only if the surrounding fullerene, which has larger curvature energy than that a SWNT of same diameter, is strongly attracted by the catalyst particle. According to this inequality, for catalysts with diameter larger than 3 nm, a graphitic encapsulation is energetically more favorable. This model correctly explains the narrow diameter distribution of SWNT grown in floating catalyst experiments (e.g., arc discharge, laser ablation, and HiPco). However, it does not apply to cases of a catalyst sitting on a substrate, in which a strong subtract-catalyst interaction could prevent the formation of catalyst encapsulation. In general, the curvature energy model predicts that catalyst encapsulation is a function of only catalyst diameter and work of adhesion, Fig. 5.2(a).

5.2.2 Thermal decohesion model

A strong argument against the above mechanistic energy model was that the thermal fluctuations [192, 193] must play a role (and even thermodynamic theory is not fully applicable because the kinetics must be considered in the nonequilibrium process of CNT growth [179, 194]). To augment the lack of thermal fluctuations in the curvature energy model, it has been suggested that for a SWNT to grow, it needs thermal kinetic energy sufficient to overcome the work of adhesion between graphene and catalyst [178, 187]. To permit the cap lift-off on a catalyst surface during SWNT

nucleation stage, a proposed criterion is

$$E_{kin} > W_{ad}, \tag{5.2}$$

where $E_{kin} \sim k_B T$ is the kinetic energy of a carbon atom on the graphitic cap (k_B is Boltzmanns constant). Such a model was used to estimate the diameter distribution of the SWNT growth in laser ablation or arc discharge experiments [193]. In sharp contrast to the curvature energy model, this model shows that the cap lifting-off is independent of the catalyst diameter, but strongly dependent on the SWNT growth temperature, Fig. 5.2(b).

5.2.3 Requirement of fast C diffusion

Recent MD simulations [177, 187] clearly show that sufficiently rapid C diffusion is required to avoid the catalyst encapsulation. During SWNT growth, all deposited carbon atoms, which may arrive at the catalyst surface randomly due to feedstock decomposition, must incorporate into the tube wall through the SWNT-catalyst contact circle. Thus, if the C mobility is not sufficient, the slowly moving C atoms may nucleate into graphitic islands or caps around the catalyst surface and eventually encapsulate it wholly. This encapsulation due to lack of C mobility means that there is a threshold temperature T_{th}, which depends on the C deposition rate, and below which the catalyst encapsulation is inevitable. MD simulations [187] also show that temperatures above T_{th} are required for the growth energy to overcome the work of adhesion, Fig. 5.2(c).

$$T > T_{th}. \tag{5.3}$$

5.2.4 Discussion

All three diagrams in Fig. 5.2 are distinct and even seem to disagree, which is not surprising because the corresponding models emphasize different factors. The curvature energy model is temperature independent, whereas the thermal decohesion model shows a W_{ad} on the encapsulation-CNT boundary as proportional to T. Experimentally, although SWNT growth dependence on temperature has been well studied, it is not possible to identify precisely the role of kinetic energy or the work of adhesion on it.

This has served as a motivation for this study, in which the catalyst encapsulation is studied as a function of W_{ad}, temperature, and consequently the C diffusion rate, by classical MD simulations. Compared with the *ab initio* method or tight-binding approximation based MD, the potential energy surface (PES) of classical MD simulation is considered less accurate, although it permits to run trajectories many orders of magnitude longer. Availability of long enough simulation time is critical to reasonably simulate SWNT growth process. Another advantage of the classical PES is that all the parameters are adjustable, which allows one to gain insight into the role of a specific parameter. For example, recently Ding et al. [195] studied how a catalyst would maintain an open end of a growing SWNT by varying the bond strength between the open end and the catalyst.

5.3 Potential energy surface

In order to run a sufficient number of long time MD trajectories, which provide statistical results, a classical PES is used here. This PES is based on the SIMCAT potential, which was described in section 2.6.5. For this study, an important charac-

teristic of this potential is the possibility to vary the interaction forces between sp^2 hybrid C and the metal cluster. This particular characteristic is used to gradually tune the work of adhesion between the graphene and the metal cluster, which allows the study of the role of W_{ad} in the nucleation of SWNT by classical MD simulation.

The tuning of the interaction forces between sp^2 hybrid C and the metal cluster is achieved by modifying the parameter α_{MC}. In this work W_{ad} between graphene and metal cluster is varied (0.0 to $\sim$ 0.3 eV) by changing α_{MC} (0.0 to 0.15), Fig. 5.3. W_{ad} is calculated for both stacking arrangements, AC and BC, using classical MD and varying α_{MC}. W_{ad} linearly increases with α_{MC}, Fig. 5.4, but a BC arrangement shows lower energy than an AC. Apparently, the potential used is not able to differentiate such small variations in energy as Bertoni et al. [196] have observed. Hence, here only W_{ad} results obtained using a BC stacking arrangement are used, which is considered by this PES a more stable structure. Note that a flat Ni surface is used to calculate W_{ad}, since a spherical Ni cluster does not provide an even surface to match the flat graphene overlayer. Although the values of W_{ad} on a flat Ni surface might be different than those on a Ni cluster, it is expected that due to the isotropic nature of the metal surface this difference is not going to be significant.

5.4 Computational details

5.4.1 Molecular dynamics

For each simulation, a M_{32} cluster (Fig. 5.5, A1) is positioned in a periodic box (size 6 $\times$ 6 $\times$ 6 nm^3) that is filled with the precursor gas (density kept constant at 0.04 molecule.nm^3). In resemblance with the early stages of CNT growth, where carbon atoms dissolve into a catalyst and then precipitate on its surface before nu-

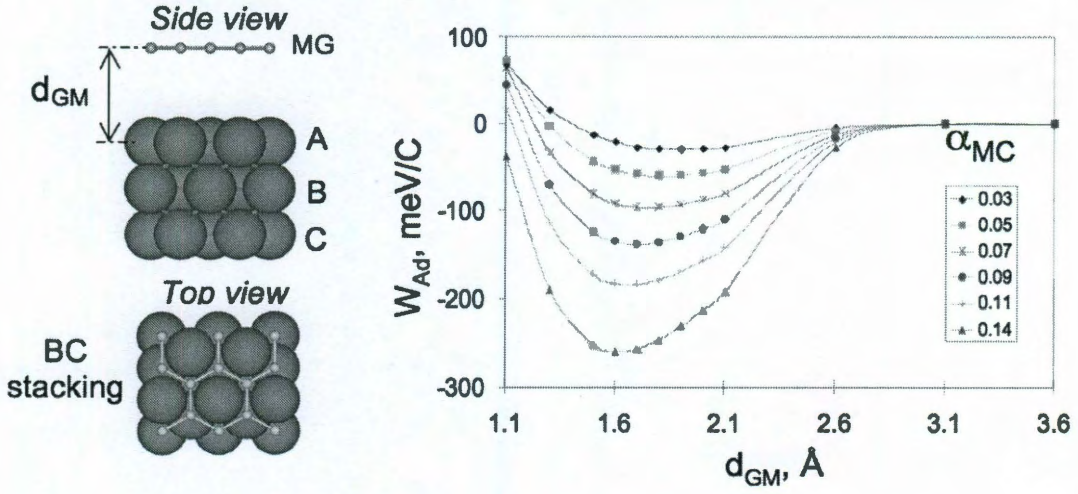

Figure 5.3 : A monolayer graphene is positioned above a Ni(111) slab and used to calculate W_{ad} by changing α_{MC}.

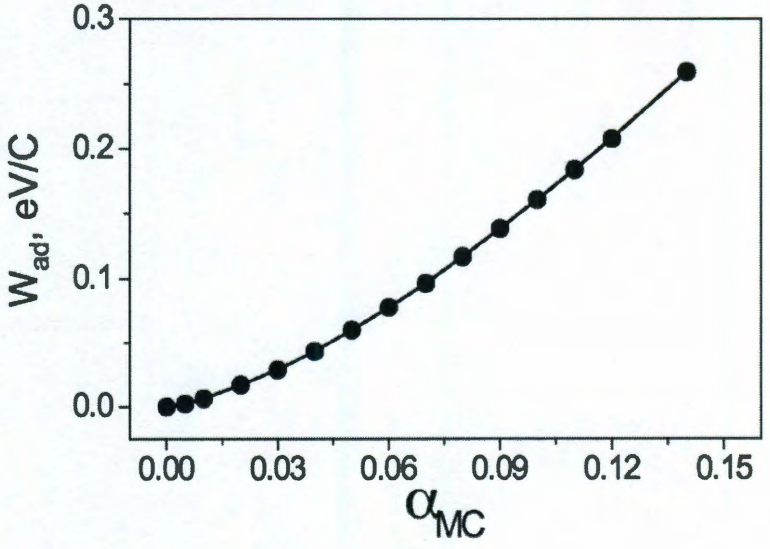

Figure 5.4 : W_{ad} increases almost linearly with α_{MC}.

cleation [178, 197, 198], the PES considers a equilibrium metal-carbon distance (calculated by DFT during its development [71]). Once an uncatalyzed C atom is close enough to a catalyst atom (metal-carbon equilibrium distance less than 0.18 nm), it is catalyzed into a normal C atom (i.e., its stronger interaction with metal is switched on), mimicking carbon feedstock decomposition in CVD carbon nanotube growth. Atomic interactions (C-C, C-Ni, and Ni-Ni) are calculated as described in section 2.6.5. The choice of relatively small metal particles permits to completely simulate a trajectory in a reasonable computational time using only one CPU; a few days for most of the simulations (the longest tube showed later in Fig. 5.8 was complete in about a month). This allowed to carry out the several hundreds of trajectories which are part of this study. Although encapsulation may occur at different conditions, as a combination of temperature and work of adhesion between the graphitic structure and the catalyst, a similar dependence for catalyst particles of different sizes is expected.

To study the competition of tubular structure vs. encapsulated catalyst as a function of temperature and W_{ad}, MD simulations were performed for a temperature range between 200 K and 1400 K, at 200 K increments. For each temperature W_{ad} was varied from 0 to 0.3 eV/C. In order to obtain more representative and convincing results, five runs are performed for each T and level of W_{ad}. In total, more than 500 MD simulations were carried out for this study. The Verlet algorithm [67] is used to integrate the equations of motion at a small time step of 0.5 fs.

5.4.2 *Ab initio* simulations

Ab initio density functional theory (DFT) is used to calculate the metal-graphene equilibrium distance (d_{GM}) and binding energy per C atom (E_{GM}). Spin polarized calculations are performed using the projected augmented wave (PAW) method [61,

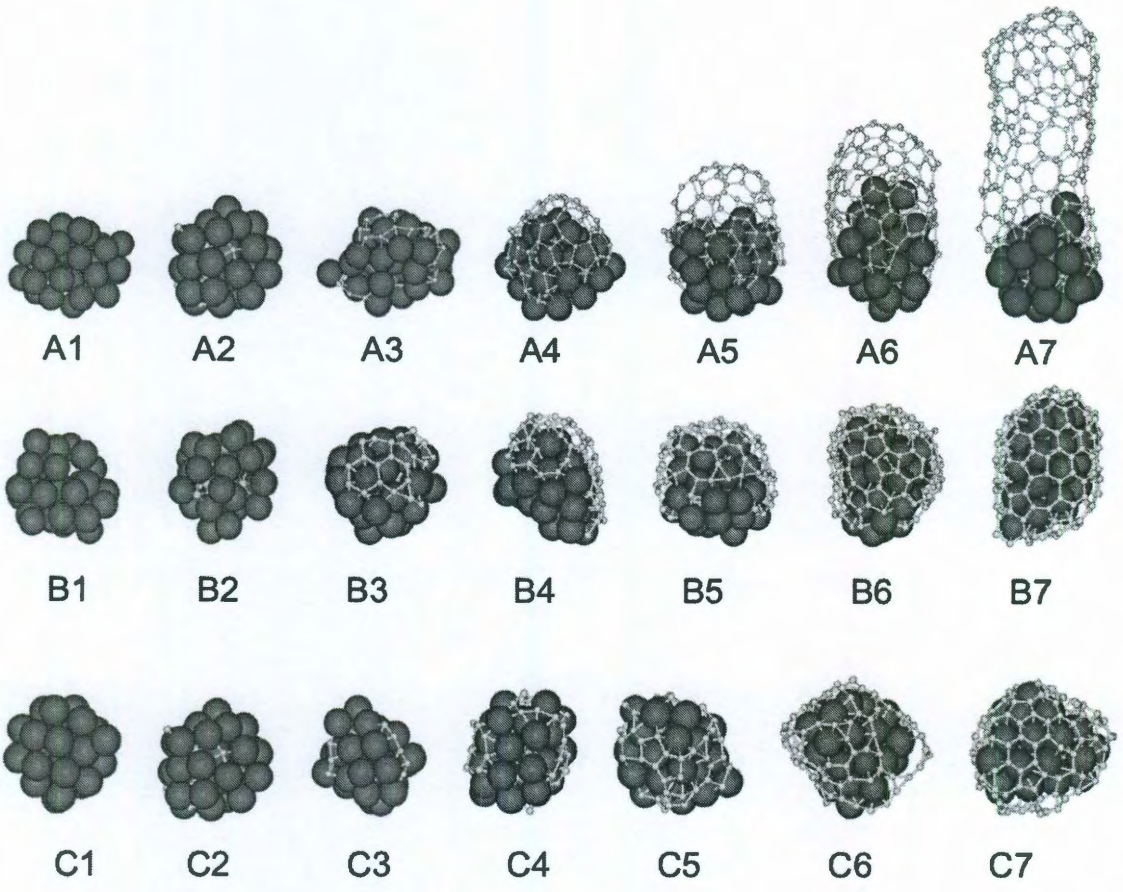

Figure 5.5 : At 1000 K and lower W_{ad} (~0.04 eV/C) C nucleates (A2–A3) on the catalyst surface forming a graphitic cap (A4) that lifts-off (A5) and grows further into a SWNT (A6–A7). A cap forms in the same way at 1000 K, but higher W_{ad} (~0.2 eV/C) (B1–B4), however it does not lift-off, and grows until it encapsulates the entire catalyst surface (B5–B7), hence deactivating it. At 200 K and lower W_{ad} (~0.04 eV/C) the metal catalyst encapsulates due to extremely slow C diffusion (C1–C7), when initially sparse C-network gradually thickens, to become impermeable for further carbon feedstock.

104] and local-density approximation (LDA) and Perdew-Burke-Ernzerhof (PBE) [55] approximation for the exchange and correlation, with plane waves kinetic energy cut-off of 400 eV. For comparison, calculations using LDA and ultrasoft pseudopotentials (US) [60] were also performed, with an energy cut-off of 286.6 eV. The system is considered optimized when the residual forces are less than 0.005 eV/Å. The semi-core p-states of Ni are considered as valence electrons in the PAW pseudo potentials. Due to the metallic character of the system, the method of Methfessel-Paxton [199] is used, with $N = 1$, and the smearing is adjusted in order to get a difference between the total energy and the extrapolated energy of less 0.5 meV/atom. The Brillouin zone integrations are carried out using a $4 \times 4 \times 1$ Monkhorst-Pack grid, and sufficient vacuum space is kept in the z direction in order to avoid spurious interactions between the slabs.

The three layered Ni (111) surface is built, using the optimized 3.53 Å lattice constant, and fully relaxed, using DFT as described above. A graphene overlayer is positioned on top of this surface according with AC and BC stacking (see Fig. 5.3 (left). Binding energy was calculated as $E_{GM} = E_{total} - E_{Ni(111)} - E_{C@graphene}$, and the corresponding d_{GM} values are comparable to literature data [174, 196, 200–202].

5.5 SWNT nucleation and growth or encapsulation

Fig. 5.5 (A1–A7) depicts a SWNT growth starting from a pure M_{32} cluster at 1000 K and with $W_{ad} = 0.04$ eV/C. The SWNT growth process is generally close to that shown in previous publications of Ding et al. [178, 197, 198]: at early stages carbon atoms dissolve into a catalyst (A1→A2) and then precipitate to the catalyst surface (A2) to nucleate into carbon chains and polygons (A3). Eventually a carbon island or carbon cap is formed (A4). A key step towards a SWNT formation is the lifting off

of the graphitic cap from the catalyst surface (A4, A5). The SWNT grows longer and longer (A5→A6→A7) in a repeatable manner. The resulting SWNT has roughly the same diameter as the catalyst particle (~1 nm), as often observed experimentally [30, 203, 204]. Unfortunately, as in previously simulated nanotubes, there is a number of defects (pentagons and heptagons) which frequently appear on the tube wall in such a way that we are not able to assign it a pair of (n, m) chiral indexes [177, 178, 180, 183, 184]. Note that this may be a consequence of the limited simulation time when compared with real experiments.

The initial nucleation stage of the simulation with a large W_{ad} (~0.2 eV/C), Fig. 5.5 (B1–B4), is almost exactly the same as shown above, Fig. 5.5 (A1–A4), but here the cap lift-off does not occur. Instead, the graphitic cap grows larger and larger until it covers the whole surface of the catalyst (Fig. 5.5 B4→B5→B6→B7). It is important to note that the catalyst surface that is not covered with a graphitic cap is almost totally free of C atoms, a result that is explained as a consequence of the reduction of dissolved carbon concentration and fast carbon diffusion [187, 198].

Fig. 5.5 C shows another simulation at temperature of 200 K and with lower W_{ad}~0.04 eV/C. Although the early nucleation stage (C atoms dissolved in the catalyst) resembles the simulations performed at high temperature, they differ significantly, as is shown below. Because of the low temperature, C diffusion is extremely slow and most of the catalyzed C atoms just stay on the initial position and a catalyzed C atom can interact only with those around it. As a consequence, C chains and small islands may form everywhere around the catalyst surface (C3, C4). Additional catalyzed carbon atoms connect these islands to form a low quality C network around the catalyst surface (C5, C6). This network becomes a full encapsulated graphene layer around the catalyst after its holes are repaired (C6→C7). The difference in

encapsulation processes at low and high temperature clearly shows an important role of C diffusion for SWNT growth.

5.6 Cap lift-off dependence on work of adhesion

A strong correlation between catalyst encapsulation and W_{ad} is clearly depicted. Fig. 5.6 shows the simulation results at 1000 K and Appendix A includes simulations at other temperatures. At lesser values of work of adhesion ($W_{ad} < 130$ meV/C), SWNT formation appears in all MD simulations. However, catalyst encapsulation starts to happen at intermediate levels of work of adhesion ($130 < W_{ad} < 170$ meV/C), to finally become inevitable at higher work of adhesion values ($W_{ad} > 170$ meV/C). Roughly, the transition from SWNT to catalyst encapsulation occurs at $W_{ad} \sim$150 meV/C or $\sim 1.7\ k_BT$, which is qualitatively in agreement with the thermal decohesion model (equation 5.2). Comparing the same simulation results to the curvature energy model, the curvature energy for the SWNT is $E_{cSWNT}(D) = C/D^2$, C=0.08 (eV nm^2/atom), whereas it doubles for the fullerene-like encapsulated catalyst, $E_{cF}(D) = 2.0\ E_{cSWNT}(D)$. Since the diameter of the catalyst is $\sim$1 nm, the curvature energy difference between an fullerene-like encapsulated catalyst and a SWNT is about ΔE_c =80 meV/C, which seems to be only half of the critical work of adhesion according to the curvature energy model. However, considering the high simulation temperature and the low structural quality of the SWNTs, this disagreement is still in the range of error.

Additionally, all MD simulations that have been performed, at different temperatures and levels of W_{ad} values (shown in Fig. 5.6 and in the Appendix A), exhibit similar dependence on the work of adhesion (Fig. 5.7a) and strongly support the idea that the work of adhesion controls the catalyst encapsulation. Statistical plots of these

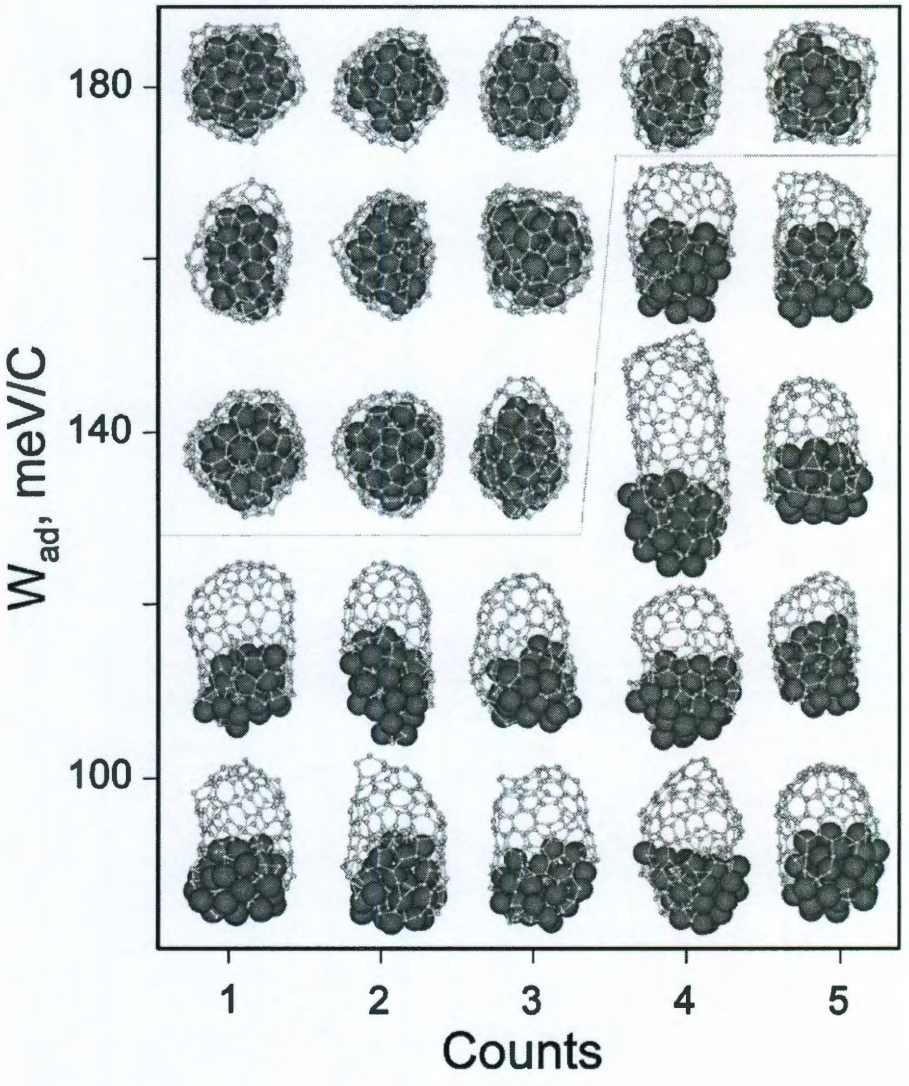

Figure 5.6 : SWNT growth and catalyst encapsulation are strongly dependent on work of adhesion. Here an example at $T = 1000$ K including all five simulations, repeated for each value of W_{ad}. (Thin line separates the incidents of encapsulation from those with lift-off.)

numerical experiments are presented as a diagram of SWNT formation vs. catalyst encapsulation, Fig. 5.7(b), which clearly shows two distinct regions. At higher temperatures, W_{ad} linearly depends on temperature. This dependence on temperature means that to lift-off the graphitic cap from the catalyst surface, higher temperatures are required at larger values of work of adhesion. This trend is in agreement with most experimental observations [28, 191, 205]: SWNTs require high temperatures for growth, whereas catalysts are encapsulated at lower temperatures. The slope of the threshold temperature is lower than that predicted by the thermal decohesion model, which means that sufficient kinetic energy is not the only cause for graphitic cap lift-off. The change in curvature energy, formation energy of the required pentagons, and edge tension around the cap should also be carefully considered. These considerations were partially included in the model proposed by Kuznetsov et al. [206] but a more detailed discussion is beyond the scope of this study.

Catalyst encapsulation dependence is very different at $T < 600$ K; it strongly depends on temperature. At very low temperature, for example at 200 K as shown in Fig. 5.5 C1–C7, the catalyst is in a solid shape, which limits the diffusion of C atoms both on its surface and across its body. This lack of diffusion hinders the transport of catalyzed carbon atoms to the growing cap or SWNT and results in catalyst encapsulation by a nucleated graphitic structure around its surface (Fig. 5.5 C). As a consequence, no tubular structures were observed to form at this very low temperature level, even at a minimum work of adhesion. Thereby, at low temperature range ($T < 600$ K) there is a strong temperature dependence, because its reduction will significantly reduce the carbon diffusion coefficient, $D \sim exp(-E_D/k_BT)$, where E_D is the diffusion barrier.

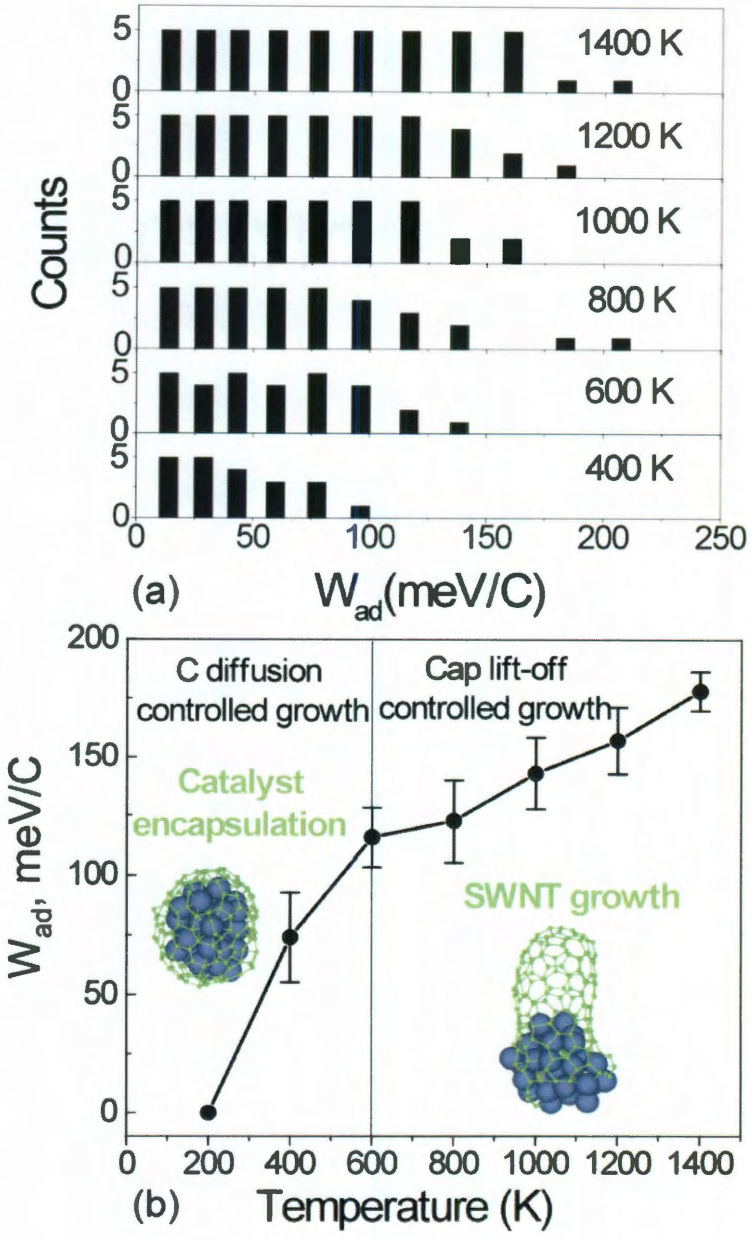

Figure 5.7 : (a) Statistical plots of the number of tubes (counts 0 to 5) at different levels of W_{ad}, from 400 to 1400 K, show two distinct regions. (b) At temperatures higher than 600 K SWNT growth is nearly temperature independent, whereas at lower temperatures (< 600 K) it is strongly temperature dependent, as limited C diffusion hinders cap lift-off and growth.

5.7 Low temperature CNT growth

Here one can ask: what is the lowest temperature at which a SWNT can grow? Early on, motivated by SWNT production from arc discharge and laser ablation experiments, it was believed that a very high temperature is required to grow SWNTs, mainly because of the high melting point of carbon materials [190,207,208]. Gradually, the lowest SWNT growth temperature was reduced below 1000 °C [171–173], until being recently reported as 350 °C [170]. Experimentally, it was shown that low SWNT growth temperature is limited by the feedstock decomposition, thus being sensitively dependent on the type of carbon feedstock [209].

From the point of view of graphitic cap lift-off, the lowest SWNT growth temperature must be associated with work of adhesion and diffusion of catalyzed C atoms. Ideally, as shown in Fig. 5.7, one can find the lowest SWNT growth temperature for a given catalyst with known constant work of adhesion. The measurement and calculation of W_{ad} is still a big challenge and the accuracy of the present data is very low. The Ni-C interaction energy in a nanotube was estimated to be between 10 meV and 1000 meV [210]. Even data obtained from state of the art *ab initio* calculations can be widely distributed within a large range (Table 5.1). Though such analysis could not be applied to obtain the lowest SWNT growth lift-off temperature of a given catalyst (e.g., Fe, Co, Ni, Au, and Cu), it is expected to be obtained in the future, based on the information contained in Fig. 5.7, through more accurate measurement or calculation of W_{ad}.

On the other hand, considering the reported lowest SWNT growth temperature on iron (350 °C), the work of adhesion of an iron catalyst can be estimated to be less than ~120 meV/C. In fact, according with the calculated results showed here, SWNT growth near room temperature (e.g., 273 K) is possible at very low level

Table 5.1 : Ni(111)-graphene binding energy (E_{GM}) and equilibrium distance (d_{GM}) calculated using different pseudopotentials.

Ni(111) stacking	Pseudopotential	E_{GM} (meV/C)	d_{GM}(Å)
AC	PAW-PBE	13.65	2.12
	PAW-LDA	290.44	1.95
	US-LDA	196.38	1.96
BC	PAW-PBE	40.29	3.85
	PAW-LDA	78.29	3.34
	US-LDA	38.19	3.30

of work of adhesion $W_{ad} < 50$ meV/C. Of course the presented MD simulations completely neglect the effects of feedstock conversion and catalyst activity, the role of buffer gas and substrate, which should be accounted for prior to real experiments (e.g., Ref. [211]). Feedstock-decomposition and C diffusion may prohibit the overall synthesis at low temperature and should be studied separately in future. Although these aspects remain oversimplified in present simulations, the findings presented here strongly encourage the search of catalysts with low W_{ad} (< 50 meV/C) and sufficient C diffusion, in order to achieve lower SWNT growth temperatures.

5.8 Growing longer CNT

The relationship between W_{ad} and T in Fig. 5.7(b), permits to make an informed choice of parameters to obtain the longest SWNT produced in any MD simulation up to date. At 600 K and $W_{ad} = 50$ meV, at relatively low carbon-gas density (0.02 molecule.nm^{-3}), a tube of $\sim$1.2 nm in length is initially obtained, which is

comparable to previously reported [75, 187]. Moreover, the growth successfully continues, at somewhat higher precursor gas density (0.04 molecule.nm^{-3}) to accelerate the process. Fig. 5.8(b)-(c) shows the SWNT as long as ~8.2 nm and then even ~13 nm, without detectable changes in quality (the proportion of hexagons is shown in the inset in Fig. 5.8). Although the quality requires further improvement, just the fact of steady uninterrupted growth within reasonable simulation times represents a significant step of achieving realistic computational modeling.

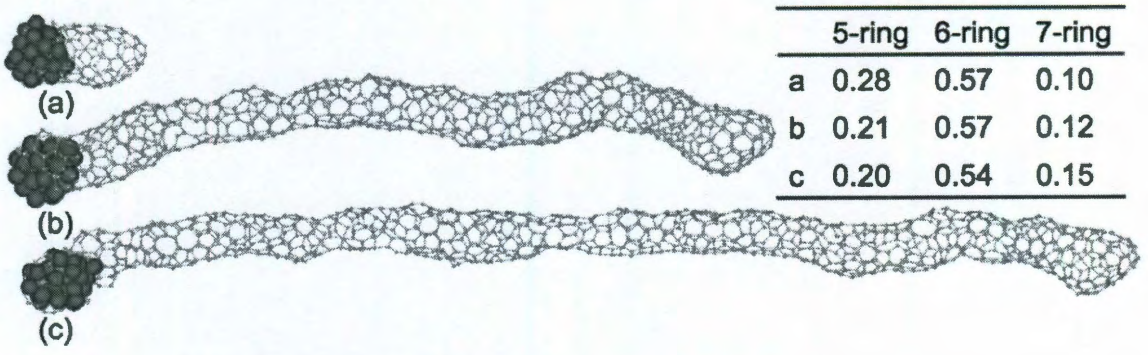

	5-ring	6-ring	7-ring
a	0.28	0.57	0.10
b	0.21	0.57	0.12
c	0.20	0.54	0.15

Figure 5.8 : Choosing the parameters based on Fig. 5.7, the longest SWNT is obtained, here at 600 K and W_{ad} =50 meV/C. (a) ~1.2 nm in length after 10 ns at 0.02 molecule nm^{-3}, (b) ~8.2 nm after 20.5 ns, and (c) ~13 nm after 27 ns, both (b) and (c) at 0.04 molecule nm^{-3}. Inset: Proportion of pentagons, hexagons, and heptagons at different simulation times.

5.9 Conclusions

Understanding the SWNT cap lift-off is a crucial part of carbon nanotube growth research. Until now, all three available models had different predictions on what is the driving force behind cap lift-off. Through MD simulations, a more comprehensive picture, composed of two distinct regions, is introduced here: i) High temperature (> 600 K), where catalyst encapsulation depends on work of adhesion, and ii) low

temperature (< 600 K), or strongly temperature dependent, where limited C diffusion hinders cap localization and lift-off for growth. The simulations also show that SWNT growth is strongly dependent on work of adhesion and C diffusion at very low temperatures (e.g., 273 K). Based on this analysis, it is suggested that experimental low SWNT growth temperatures can be achieved through use of catalysts with low work of adhesion. This is critically important not only from a general process efficiency point of view but especially for possible *in situ* growth for nanoelectronics applications.

Chapter 6

Effect of catalyst type and shape on CNT growth

The electronic properties of carbon nanotubes (CNT) depend on the tubes chirality, as shown in chapter 1. For almost two decades since its discovery, researchers around the world have sought how to obtain CNT with a chirality specific. The most successful attempts have been related with post-processing CNT selection, as recently shown for density-gradient ultracentrifugation utilization [31]. A more direct, although not easier, route is to achieve chirality selectivity during the CNT synthesis process. In a rare example, Harutyunyan et al. [32] obtained high yield of metallic tubes through tuning of CNT growth conditions. Nevertheless, little is know about the controlling forces behind such selectivity conditions.

Experimental evidence indicates that catalyst type and crystal shape have an important role during CNT growth. The use of alloyed nanocatalysts with variable atomic compositions resulted in CNTs with different nucleation ability, final length, and diameter [212]. Such bimetallic catalysts are analyzed here in section 6.2 as a means to precisely tune metal catalyst properties for chirality selective CNT growth. Experimental observation of CNT growth often includes catalyst reshaping [174, 175, 213, 214], as well. However, there has been no clear indication of the relation, if any, between CNT nucleation and catalyst reshaping. Very recently, catalyst dynamic restructuring has been connected to Ni diffusion through a series of multi-scale simulations [215], without taking into account the carbon atoms resulting from the feedstock decomposition, which are adsorbed on the catalyst surface. Here,

empirical potentials and first-principles methods are used to analyze how catalyst reshaping relates to CNT growth. Molecular dynamics simulations provide a qualitative picture of the CNT growth, which includes catalyst reshaping (section 6.3), whereas tight-binding and *ab initio* methods are used to analyze the modifications that various Ni surfaces undergo upon C chemisorption, in section 6.4. Such analysis serves as basis to formulate a continuum phenomenological model explaining CNT cap nucleation from the reshaping of the catalyst, in section 6.6, and to propose an oscillatory mechanism for CNT growth.

6.1 Methodology

6.1.1 Ab initio

The thermodynamic equilibrium geometries of the bimetallic clusters and Ni slabs were obtained through density-functional calculations with all-electron projected augmented wave potentials [61, 104] and the generalized gradient approximation of the Perdew-Burke-Ernzerhof (PBE) [55] for exchange and correlation, with plane waves kinetic energy cut-off of 400 eV, as implemented in VASP [105–107]. A conjugate gradient scheme was employed to relax the geometry until the forces on every atom were less than 0.005 eV/Å. Large vacuum spaces in the supercells (up to ~17 Å in the case of tube coupled to a catalyst) are used to minimize any cell-cell spurious interactions. The optimized Ni bulk lattice parameter (3.53 Å) was used to construct the various Ni surfaces. All the layers of the slab are allowed to relax for the surface energy calculations, whereas the bottom layer is fixed (to simulate the bulk) for calculations involving C adsorption. The Brillouin zone sampling used a $12 \times 12 \times 12$ Monkhorst-Pack grid for the Ni bulk and at Γ-point for the clusters. For the slabs with different

orientations, the number of k-points used in sampling is given in Table 6.1.

6.1.2 Empirical potentials

Molecular dynamics using the SIMCAT potential was used to simulate clusters with ~2.2 nm in diameter, using the same methodology described in Ref. [4,71]. The initial Ni_{500} cluster (Fig. 6.4 A) is submitted to constant C feedstock pressure (density 0.02 atoms.nm^{-3}), at 1000 K, and 0.02 eV/C carbon-metal adhesion energy.

The Reax Force Field (ReaxFF) is used to calculate the surface energy of the C adsorbed Ni surfaces. This empirical potential was introduced by van Duin et al. [216] and it describes the carbon chemistry through a bond order-bond distance relation. After recent re-parametrization [217] this potential has used to describe remarkably well the C-Ni interactions in CNT growth [218]. The ReaxFF was used as implemented in LAMMPS [219] and the initial structures were completely relaxed using a conjugate gradient scheme.

6.2 Catalyst design for CNT growth

What describes a "good" catalyst for CNT growth? Higher catalytic activity resulting in cap nucleation, along with feedstock decomposition, and adequate support for the tube are desirable characteristics of a catalyst for CNT growth. In chapter 5, the cap lift-off or encapsulation dependence on temperature and/or metal-C interaction was described as being divided in two regions: 1) High temperature (> 600 K), where catalyst encapsulation depends on work of adhesion, and 2) low temperature (< 600 K), or strongly temperature dependent, where limited C diffusion hinders cap localization and lift-off for growth.

Direct measurements of the binding energy of the cap to the catalyst have not

been realized yet, but they can be estimate through experimental observations. For example, composition variation in Fe-Co binary alloy catalysts resulted into different CNT nucleation ability, final length, and diameter [212]. Although a catalyst with higher content of Fe had better sustaining growth, resulting in longer single-wall carbon nanotube (SWNT), the ones with higher content of Co had larger nucleation yield, smaller diameter averages, and narrower diameter distribution. Theoretically, the binding energy of either a (3,3) or (5,0) SWNT to a M_{13} cluster, where M is the metal type, is stronger for Co, Ni, Fe than for Pd, Cu, and Au, in this order [195]. In this section, it is shown that the work of adhesion can be tuned by using bimetallic catalysts.

6.2.1 Bimetallic catalysts

Bimetallic nanocatalysts are obtained by alloying different metals at nano-scale, resulting into catalysts with new and desirable properties [5, 220]. Synergistic effects and lower production cost arising from the alloying process may have a big impact on applications, e.g., hydrogen storage [41] and CNT growth [212]. Selective chirality is the most desirable property to be achieved in CNT growth and the use of bimetallic catalysts may offer a route for that. Chiang and Sankaran [221] have found that by tuning the composition of Ni_xFe_{1-x} nanoparticles the chirality of synthesized CNTs is significantly narrowed.

One aspect to be explored is the ability of bimetallic nanoparticles to be used to fine tune the catalyst-CNT interaction. The first step is to determine the thermodynamically most favorable bimetallic catalyst structures. Here, a M_{13} icosahedral cluster is used to model a M_xFe_y alloy catalyst, where M=Ni or Cu and x and y are atomic fractions, for x =0.23 and 0.77, and $y = 1 - x$. The use of icosahedral clusters

permits to study all the possible homotops for each composition and isomer due to its high symmetry and, by using small clusters, permits the use of *ab initio* calculation methods.

The different possible arrangements of the atoms (homotops) [220, 222] for each composition of M_xFe_y catalyst are determined by comparing their binding (E_{coh}) and cluster formation ($E_{f,c}$) energies. As seen in Eq. 6.1, E_{coh} does not take into account the different possible structures [223]. Thus, the cluster formation energy is used to determine the thermodynamically most favorable configuration among the homotops.

In both sets of M_xFe_y, the Fe atoms occupies the central position in a somehow distorted icosahedral. For higher Fe at.%, the Ni and Cu atoms tend to maximize their respective number of Ni-Ni and Cu-Cu bonds and minimize the number of M-Fe bonds by forming compact structures on the surface of the cluster. At lower Fe at.%, the Ni and Cu atoms tend to form a ring around the cluster.

$$E_{coh} = -\left(E_{M_xFe_y} - x\,E_M - y\,E_{Fe}\right)/\,x + y, \tag{6.1}$$

where M=Ni or Cu and x and y are the atomic fractions, for x =0.23 and 0.77, and $y = 1 - x$.

$$E_{f,c} = \left(E_{M_xFe_y} - \frac{x}{x+y}E_{M_{x+y}} - \frac{y}{x+y}E_{Fe_{x+y}}\right)/\,x + y. \tag{6.2}$$

6.2.2 Bimetallic catalysts in CNT growth

The adhesion strength of a SWNT to the bimetallic catalysts is evaluated by placing an armchair (3,3) or zigzag (5,0) open SWNT on the lowest energy isomers for each atomic composition and calculating their binding energy (E_b), Fig. 6.3(a)-(b).

$$E_b = -(E_{SWNT+M_xFe_y} - E_{SWNT} - E_{M_xFe_y})/N_{db}, \tag{6.3}$$

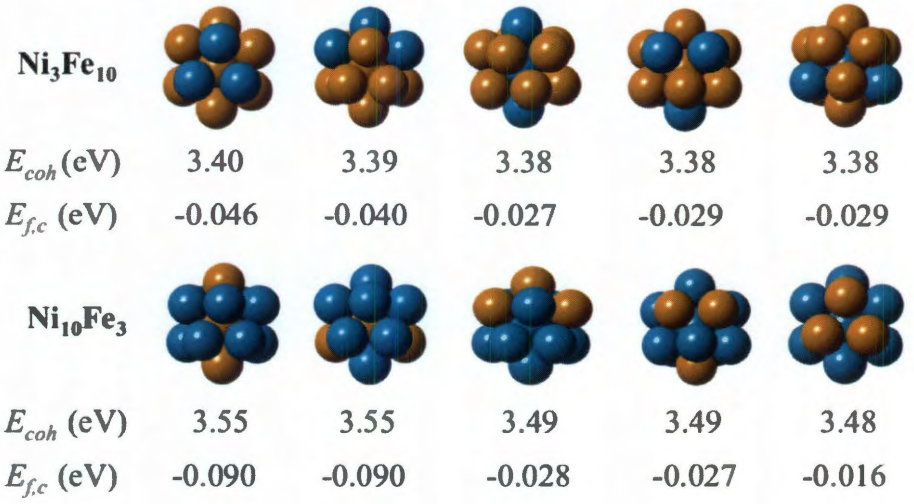

Figure 6.1 : Possible Ni and Fe atomic arrangements for Ni_xFe_y with their respective cohesive (E_{coh}) and cluster formation ($E_{f,c}$) energies. Ni and Fe atoms are blue and brown, respectively.

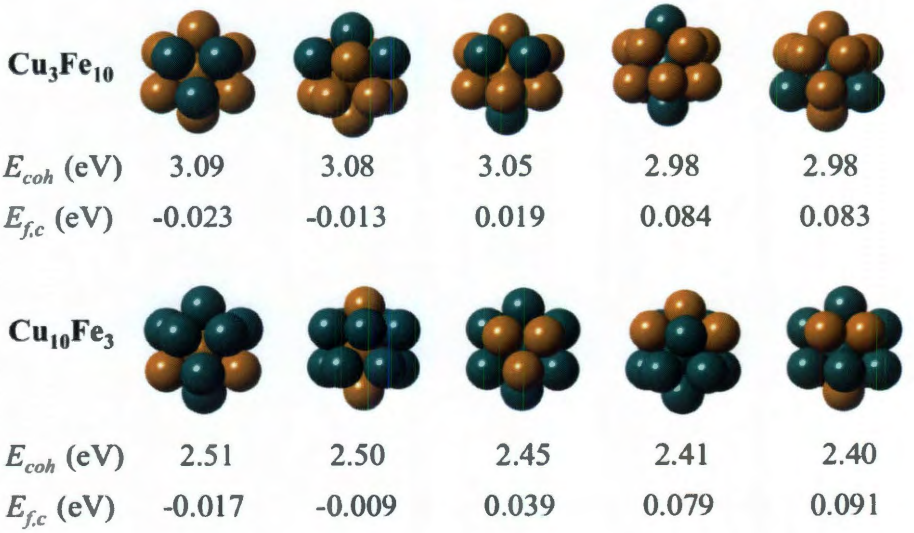

Figure 6.2 : Possible Ni and Fe atomic arrangements for Cu_xFe_y with their respective cohesive (E_{coh}) and cluster formation ($E_{f,c}$) energies. Cu and Fe atoms are green and brown, respectively.

where N_{db} is the number of dangling bonds on the open side of the tube to which hydrogen atoms are attached.

Here, there are a few possibilities of arrangements of the tube on the catalyst, as well. The complete set of possible configurations and their respective E_b is shown in Appendix B (Fig. B.1 and B.2). Clearly, for all the combinations of x and (n, m), the most stable structure is the one where the tube is placed on top of a Fe atom. In general, the most stable system favors the minimization of the number of M-C bonds for lower atomic fractions of Ni and Cu, whereas it tends to maximize the number of M-C bonds at higher atomic fractions, Fig. 6.3(c)-(d).

Among the pristine metals analyzed, Fe has the strongest binding energy, followed by Ni and Cu, agreeing well with previous calculated results [195]. The values of E_b showed in Fig. 6.3, calculated by first-principles, correspond to the relatively most stable configuration. The Ni-Fe catalyst variation in composition results in a small change of E_b when attached to the armchair (AC) tube, Fig. 6.3(a). Interestingly, E_b for $Ni_{0.23}Fe_{0.77}$ is higher and $Ni_{0.77}Fe_{0.23}$ is lower than the binding on the pristine metals. When switching to a zigzag (ZZ) tube, E_b for $Ni_{0.77}Fe_{0.23}$ behaves opposite to as on AC, being higher than on both Fe and Ni, Fig. 6.3(b). The difference in E_b for AC and ZZ on Cu_xFe_y with catalyst composition is more discrete. The adhesion strength energy values decrease with an increase of Cu atomic fraction; particularly for the ZZ case even a small fraction of Cu raises E_b close to Fe or Ni values. Thus, the binding energy of Ni_xFe_y to the CNT is chirality selective, which has indeed been observed experimentally [221]. For Cu_xFe_y, the inverse relation between E_b and Cu atomic fraction provide a clear way to fine tune the catalyst-CNT binding, which can also be beneficial to CNT selective production (e.g., length).

These differences in adhesion strengths indicate that specific bimetallic catalysts

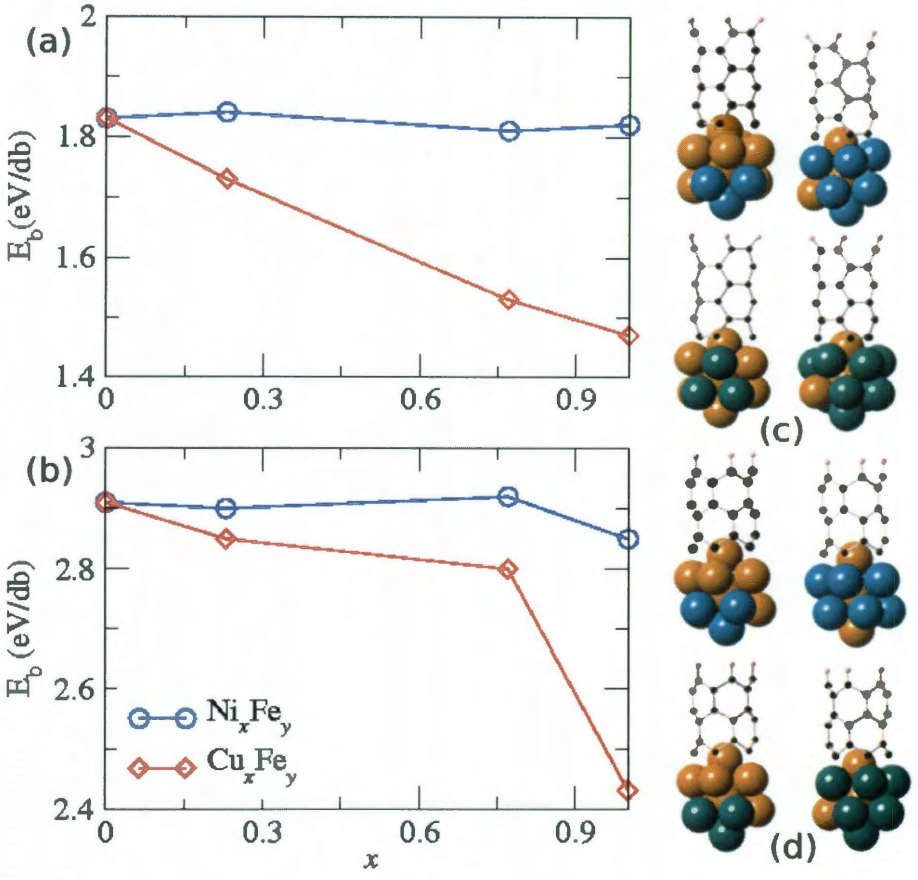

Figure 6.3 : Binding energy (E_b) of (a) (3,3) armchair and (b) (5,0) zigzag open SWNT on M_xFe_y catalysts, for M=Ni and Cu, x =0.23 and 0.77, and $y = 1 - x$. Lowest energy configurations for the (c) (3,3) and (d) (5,0) tubes on M_xFe_y.

could be used to fine tune the metal-carbon interaction during CNT growth. Experimentally, pristine Cu has been found to be a poor catalyst in CNT growth [224]. However, its weak binding to carbon has been positively used to successfully produce horizontally aligned arrays of SWNT [225]. Else, a too strong metal-carbon interaction could prevent the lift-off and growth [4]. A lower tube-catalyst interaction energy (compared with pristine Fe), as in the case of $Cu_{0.23}Fe_{0.77}$, would facilitate the lengthening of the tube. In fact, it has been observed experimentally that the addition of smaller amounts of Cu to Fe_3O_4 resulted in longer CNT than using only Fe_3O_4, and twice as longer than using smaller amounts of Ni [226].

In a previous work, Ding and co-workers observed that simulations of such small clusters and SWNT resulted in similar results of those using larger clusters and tubes [195]. However, a more realistic model for growth of SWNT requires the use of catalysts with diameters of 2-3 nm, which is not possible through first-principles, but can be done using molecular dynamics simulations, as shown next.

6.3 MD simulation of catalyst shape during CNT growth

Carbon nanotube nucleation and growth has been usually associated to the continuum-phenomenological VLS (vapor-liquid-solid) model. In this widely known simple growth model originally proposed for whiskers-nanowires [188, 189], the growth process is divided into cap nucleation, lift-off, and lengthening [175, 190, 227]. According to this model, carbon feedstock from a vapor phase decomposes onto a liquid catalyst surface, releasing the carbon atoms to diffuse across the catalyst towards the open end of the solid CNT and to be added at the edge. In chapter 5, small clusters ($\sim$1 nm in diameter) have been used to gain insight into the nucleation and growth of the CNT and to correctly illustrate the crucial steps of the VLS model applied to CNT growth.

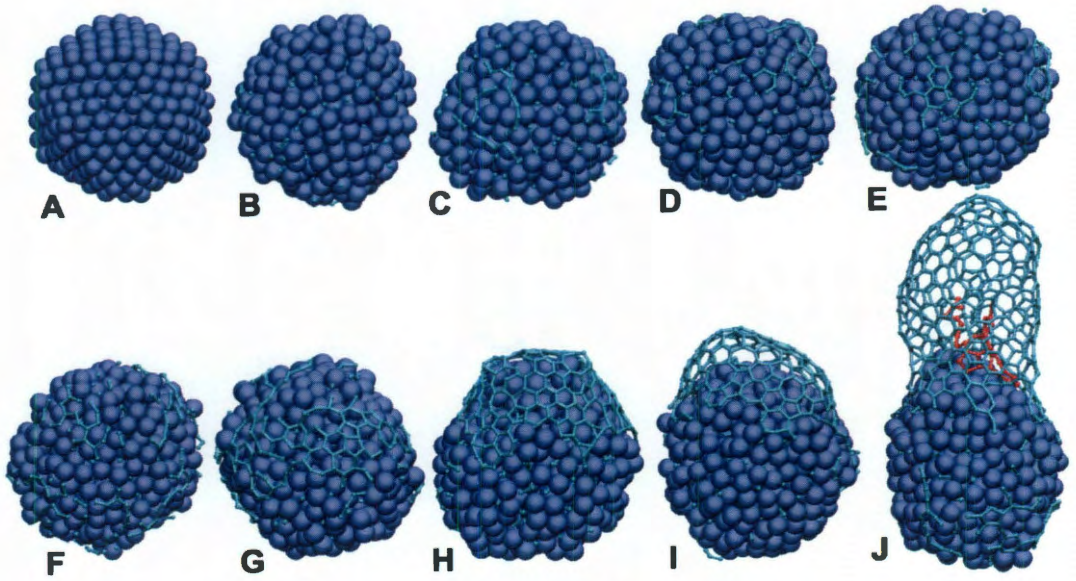

Figure 6.4 : Molecular dynamics sequential trajectories for carbon nanotube growth on a (A) Ni_{500} catalyst: (B–E) nucleation, (F–I) lift-off and (J) elongation.

Using a large Ni catalyst (~2.2 nm), the CNT nucleation, lift-off and growth are shown through MD simulations (Fig. 6.4) in a clear and defined way. The initial nucleation stages are very similar to those previously reported using very small clusters [4, 178, 198]. The carbon atoms are incorporated into the clean catalyst (Fig. 6.4 B), to later precipitate onto its surface forming chains (Fig. 6.4 C) and polygons (Fig. 6.4 D–E), which will grow into graphitic islands to form the cap.

The use of a more realistic metal catalyst presents some interesting additional features related with CNT nucleation and lift-off. Initially, it does not appear that a preferred nucleation site for the graphitic islands exists, and a few of these small structures are observed distributed on the catalyst (Fig. 6.4 F). However, subsequent steps show that these small islands give way to a major graphitic structure (Fig. 6.4 G), which becomes the precursor for the CNT cap. Once the cap is complete and rela-

tively stable, the catalyst reshapes itself (Fig. 6.4 H) and is somehow expelled from within the cap (Fig. 6.4 I), in what is commonly known to be the cap lift-off. After that, the cap grows by addition of new C atoms on its edge (Fig. 6.4 J). Interestingly, sometime after the lift-off a new graphitic structure starts to grow inside the tube (highlighted in red in Fig. 6.4 J) in what appears to be the precursor of a new CNT wall.

These simulations provide a good qualitative picture of the CNT growth, including events observed experimentally such as catalyst reshaping [174, 175, 213, 214] and an incipient double-wall. However, after the C atoms start depositing on the catalyst surface, the different facets, which belong to an equilibrium Wulff-construction, are indistinguishable during the MD simulations. One way to overcome this limitation is to model the deposition of C on each metal individual surface, as it is shown next.

6.4 Properties of the Ni surface

Many important catalytic processes depend on surface reactions between the carbon and transition metals. To obtain insight into heterogeneous catalysis and metallurgical processes like metal dusting and alloying, the Ni-C interaction was subject of intense experimental investigations in the 70's-80's [228–232]. Interest on such studies has been strongly renewed in recent years as researchers seek to discover ways to control CNT and graphene growth.

There has been several studies on the low-index Ni surfaces, with emphasis, in recent years, on the binding energy of the C atom to these surfaces [233–236]. Surprisingly, there has been no systematic study of the interplay of low- and high-index Ni surfaces and the behavior of the corresponding catalyst during CNT growth (C adsorption). High-index surfaces have a distinct stepped topography. They are par-

ticularly important given that stepped surfaces have been found to play a significant role on CNT growth, anchoring the tube and acting as growth sites [174, 179]. However, the surface energy and relaxation of Ni stepped surfaces have been scarcely studied and most of the studies involve only one stepped surface at a time [237, 238]. The high-index surfaces require considerably higher computational resources due to the minimum size of their slabs, which in part explains why most work done on these surfaces involved empirical or semi-empirical potentials [239, 240].

Even experimental observations of Ni catalysts still do no agree about which high-index facets have the lowest surface energy and, consequently, have a more significant role in describing the equilibrium crystal shape of the catalyst. Hence, besides the well-known low-index Ni surfaces (100), (110), and (111), the high-index surfaces (211), (311), (210), and (320) are studied here, through *ab initio* calculations. The (211) and (311) surfaces are vicinal to (100) and (111) and more close packed, whereas the (210) and (320) are vicinal to (100) and (110) and more loosely packed. The atomic arrangement and the unit cell used for the relaxation of these seven surfaces is shown in Fig. 6.5.

6.4.1 Surface relaxation

The selection of a slab is defined by how well its surface properties are converged. Here, slabs with increasing number of layers are used to determine the minimum thickness necessary for well-converged surface energy and relaxation. Surfaces with the same number of layers can have very different thicknesses, for example, a slab of 6 Å will have four layers in Ni(111) or 14 layers in Ni(320) surfaces.

The surface relaxation is calculated as $\Delta_{ij} = (d_{ij} - d_{hkl})/d_{hkl} \times 100$, where d_{ij} is the interlayer spacing between layers i and j, and d_{hkl} is the interlayer spacing

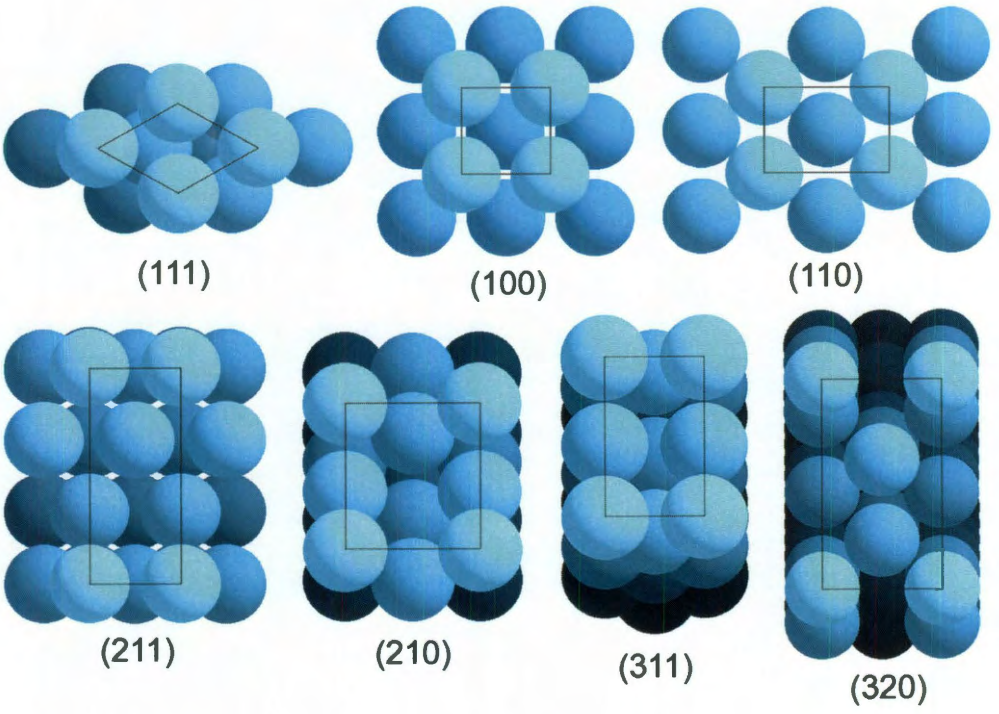

Figure 6.5 : Top view of the atomic arrangements of the various relaxed Ni surfaces; lighter atoms are close and darker atoms are farther from the surface. The unit cells are indicated.

in the bulk for the (hkl) surface. The calculated values of the surface relaxation between the first and second top most layer (Δ_{12}) for various thickness are shown in Fig. 6.6(a). Except for the thinnest (210) slab, all the surfaces contract, with the oscillatory behavior of Δ_{12} being more evident for the high-index surfaces. For (100), (110), and (111), Δ_{12} values are well-converged for slabs thicker than 6 Å. For (211), (311), 210, and (320), its values are well-converged for slabs thicker than 12 Å, though optimum thicknesses (to reduce the computational effort) can be found between 6 and 12 Å.

It is very important to establish the correct thickness of the slabs to be used in adsorption simulations because a too thin slab may have unrealistic open spaces. For example, a complete slab without missing atoms for the (311) surface will have 11 layers, with a corresponding thickness of 10.61 Å, whereas for the (320) surface it will have 13 layers, with a corresponding thickness of 5.87 Å.

Both experimental and theoretical data on surface relaxation of Ni are spread over a wide range of values as shown by Rodríguez and co-workers [241]. Experimentally, it has been evaluated only for the four most close-packed Ni surfaces, mostly using low-energy electron diffraction (LEED). Experimental measurements of Δ_{12}, plus or minus some error bar of less than 1%, are -1.23 % for (111) [242], -3.2 % for (100) [243], $\sim$ -8.4 to -9.8 % for (110) [244–246], and -15.9 % for (311) [247]. The calculated Δ_{12} (for slabs $\sim$12 Å, shown in Table 6.1) for (111), (100), (110), and (311) agree well with the respective experimental values found in the literature, which are plotted as open symbols in Fig. 6.6(b). For the other high-index surfaces, there has been no experimental measurements, though the surface relaxation of (210) has been calculated (-12 %) by FLAPW [238].

The openness of the surfaces can be better understood by calculating their rough-

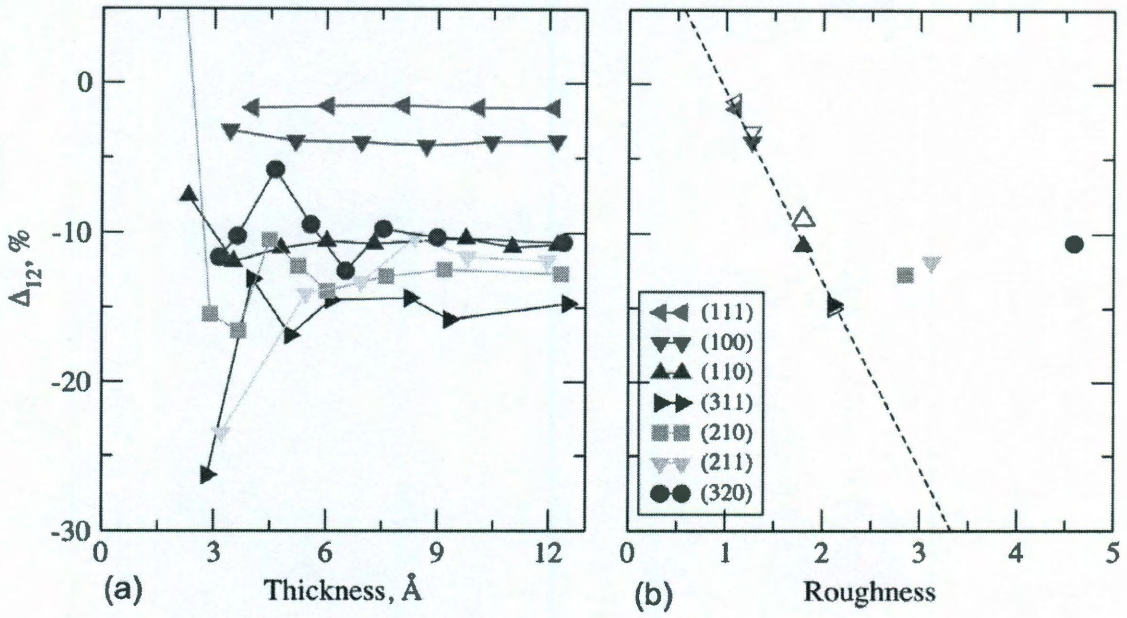

Figure 6.6 : Surface relaxation between the first and second top most layer (Δ_{12}): (a) For various slabs thicknesses and (b) its relation with roughness for slabs ~12 Å. The open symbols correspond to Δ_{12} found in the literature (see text for details)

Table 6.1 : Surface energy (γ_0) and relaxation (Δ_{12}) for the clean surfaces in slabs > 6 Å, surface roughness (S_r), interlayer spacing in the bulk (d_{hkl}), and the number of k-points for the Brillouin zone integrations.

Surface	γ_0 (eV/Å^2)	Δ_{12} (%)	S_r	d_{hkl}	k-points
(111)	0.119	-1.68	1.10	$a/\sqrt{3}$	$12 \times 12 \times 1$
(100)	0.136	-3.93	1.27	$a/2$	$12 \times 12 \times 1$
(211)	0.136	-13.29	3.12	$a/2\sqrt{6}$	$12 \times 6 \times 1$
(110)	0.139	-10.72	1.80	$a/2\sqrt{2}$	$12 \times 8 \times 1$
(311)	0.141	-14.49	2.11	$a/\sqrt{11}$	$12 \times 4 \times 1$
(210)	0.145	-12.45	2.85	$a/2\sqrt{5}$	$8 \times 4 \times 1$
(320)	0.146	-9.46	4.59	$a/2\sqrt{13}$	$8 \times 4 \times 1$

a is the lattice parameter.

ness (Table 6.1). The roughness (S_r) can be estimated by the interplanar spacing or calculated as the ratio between the 2-D planar area and the cross section of a hard-sphere with radius corresponding to half of the nearest neighbor distance in bulk, i.e., $S_r = A/A_{\mathrm{Ni}}$, in which $A_{\mathrm{Ni}} = \pi a^2/8$. As the surfaces become more open the interplanar distance decreases and the roughness increases. Accordingly, Δ_{12} is inversely proportional to the roughness for (111), (100), (110), and (311), Fig. 6.6(b), similarly to the body-centered Fe [248, 249].

6.4.2 Surface energy

Given the *in situ* observations of metal catalyst reshaping during CNT growth [174, 175, 213, 214], and Ni being a common catalyst used for CNT growth, it is surprisingly that there has not been any theoretical study to determinate the complete Ni

equilibrium crystal shape yet. The equilibrium crystal shape is obtained through the minimization of the surface energy, and the study of a large enough number of facets, including the high-index surfaces, is fundamental to obtain more realistic results.

The general expression to calculate the surface energy uses the value of the total energy of a slab (E_{total}) with N layers and the bulk energy (E_{bulk}). As the slab has two surfaces, the factor $1/2$ brings the equation to account for the energy of only one of the surfaces.

$$\gamma_0 = \lim_{N\to\infty} \frac{1}{2}(E^N_{\text{total}} - N\,E_{\text{bulk}}). \tag{6.4}$$

A commonly overlooked issue refers to the value of E_{bulk}. Boettger [250] has shown that using the E_{bulk} value obtained from a separate bulk calculation γ_0 diverges as the slab thickness N increases. This is particularly important when evaluating γ_0 of high-index surfaces, which require thicker slabs for representative calculations.

As an alternative to avoid such problem, Fiorentini and Methfessel [251] observed that Eq. 6.4 implies that $E^N_{\text{slab}} \approx 2\gamma + N\,E_{\text{bulk}}$. Hence, their suggestion is to extract E_{bulk} from the linear fitting of E_{total} vs. N, as shown in Fig. 6.7(a). The values for the Ni facets fall perfectly into a linear curve; for clarity only the smallest and highest linear slopes are shown in the figure, -5.559 eV for (211) and -5.564 for (111), respectively. The γ_0 converges very well using the Fiorentini-Methfessel scheme, whereas, for the same calculations, it diverges when E_{bulk} is taken from a bulk calculation, as shown in Fig. 6.7(b) for the Ni(320) surface. As well as for the other Ni facets, γ_0 completely converges for (111), (100), (110), (211), (210), (311), and (320) slabs at 12 Å, Fig. 6.8(a).

The Wulff-construction is obtained using a computational tool called Wulffman [252] and Geomview [253], Fig. 6.8(b), utilizing the values of $\gamma_0 \sim 6$ Å, which are shown in Table 6.1. It is observed that the initial Ni catalyst shape is faceted, which agrees

with experimental observations. Hong et al. identified the {111}, {100}, {110}, and a facet which could be either {210} or {320} as present in the Ni equilibrium crystal shape [254]. In Moors et al. [255], the surfaces of a supported Ni catalyst used for CNT growth were identified as {111}, {100}, {110}, and {311} [255]. Considering γ_0 calculated here, the surfaces visible in the Wulff-construction, shown in Fig. 6.8(b) are {111}, {100}, {110}, {210} and {311}, which reconciles both experimental observations.

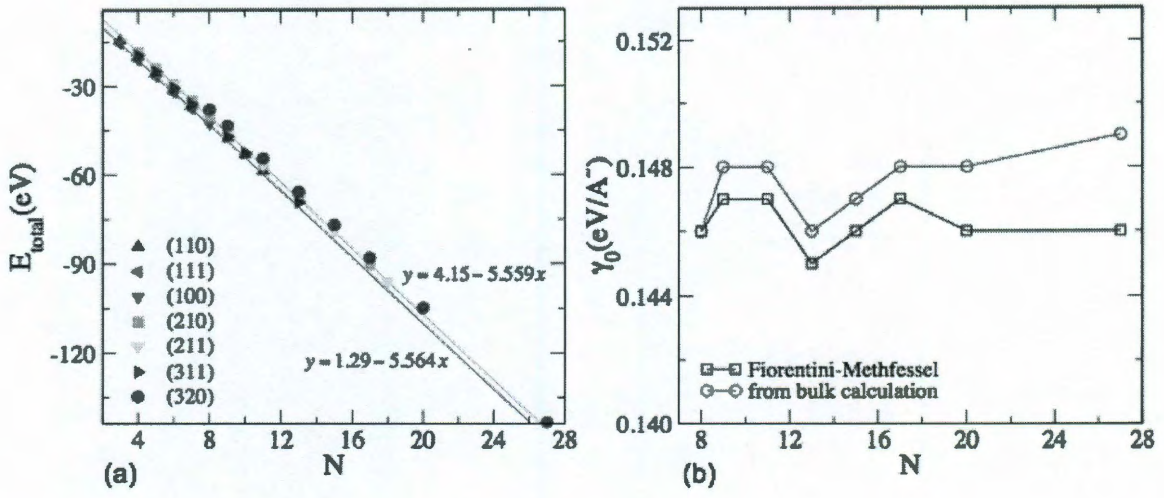

Figure 6.7 : (a) Linear fitting to obtain E_{bulk} according with the Fiorentini-Methfessel (F-M) scheme. (b) γ_0 converges very well using the F-M scheme, whereas it diverges when E_{bulk} is taken from a bulk calculation, as illustrated by the Ni(320) surface results.

6.5 Carbon adsorption on Ni surfaces

6.5.1 Binding energy

Metal surfaces are very reactive to gaseous species and the binding energy measures how strongly a certain species is adsorbed on the surface. Hence, considering C atoms

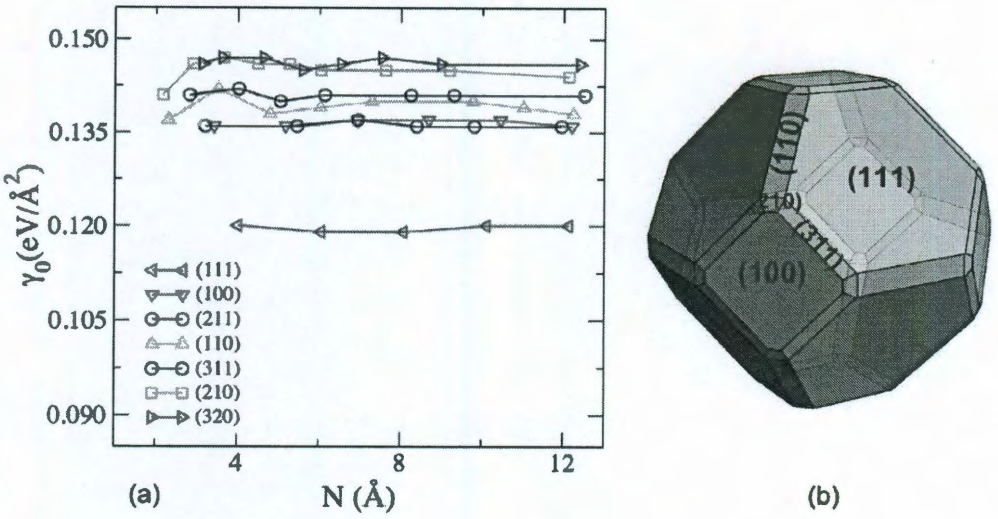

Figure 6.8 : (a) Surface energy (γ_0) for the Ni surfaces converges with the slab thickness. (b) Ni equilibrium shape obtained from the minimized γ_0 for low- and high-index surfaces.

adsorbing on a Ni slab, firs-principles are used to calculate the binding energy (E_b).

$$E_b = E_{\text{slab}} + E_{\text{C}} - E_{\text{total}}, \tag{6.5}$$

where E_{slab}, E_{C}, and E_{total} are the clean slab, C atom, and system total energies. The calculated E_b for the most energetically favorable adsorption sites of the low-index (111), (110), and (100) surfaces are shown in Table 6.2. The E_b experimental and calculated DFT values are also shown for comparison.

The Ni(111) surface has two adsorption sites, at the hexagonal close-packed (hcp) and face-centered cubic (fcc) positions (Fig. 6.9). For the adsorption of a C atom, the hcp site is more favorable than the fcc by just 0.05 eV. Similarly, the Ni(110) surface also has two adsorption sites, at the long-bridge (between the top atoms) and hollow site (on top of the atom on the next layer). A C atom at the (110) long-bridge is more stable than at the hollow site by 0.15 eV. The Ni(100) surface has only one

adsorption site, at the hollow site of the unit cell.

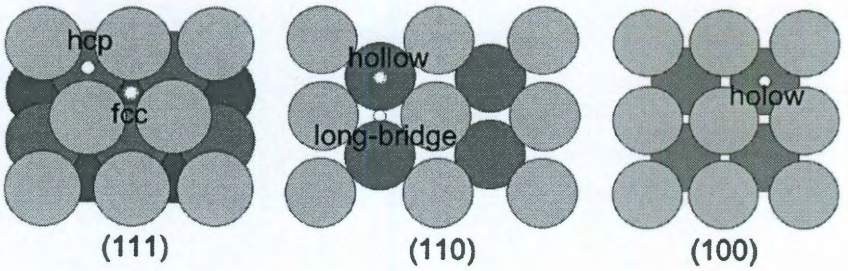

Figure 6.9 : The adsorption sites for Ni low-index surfaces are shown on (2×2) supercells. Ni atoms are grey and C are white; darker atoms are farther from the surface.

Table 6.2 : Binding energies (eV/C) for the Ni low-index surfaces, (111), (110), and (100). The present calculated values are compared with theoretical and experimental values (eV) from the literature.

Surface	Present	DFT	Experimental
(111)	6.93	7.25 [234] / 6.28 [237]	7.5 [228] / 7.40 [229] / 6.91 [231]
(110)	7.64	7.65 [234] / 6.76 [237]	
(100)	8.28	8.49 [234] / 7.61 [237]	7.35 [230]
–			6.89[a][232]
			7.07[b][232]

[a] $\theta = 0.5$ and [b] 0.9, on Ni/Al_2O_3 catalyst.

A clear trend of the calculated E_b can be seen in Table 6.2, with C adsorbing more strongly from the (111) to the (100) surfaces. As seen in chapter 5, Ni-C interaction vary strongly with the pseudopotential used, and as discussed in chapter 2, the local density approximation (LDA) does not describe the behavior of transition metals as

well as the generalized gradient approximation (GGA) does. The calculated E_b from the references, shown in the table, have different values for the same surface, though they were all calculated using the same cut-off energy, GGA, and VASP package. These variations can be attributed to use of different slab thicknesses and k-points, hence the need of a systematic study as it is done here.

Graphene growth was experimentally observed to occur on the Ni(111) surface [202, 228, 256], as the interaction of the graphene overlayer with the Ni(111) surface results in very small lattice mismatch (2 % contraction [202]). The transition of one C atom until formation of a complete graphene layer adsorbed on the Ni(111) surface is shown in details next. Several non-equivalent initial arrangements for the C on the surfaces are evaluated and the final thermodynamically most favorable structures are shown in Fig. 6.10. These are similar to those obtained by Kalibaeva et al. [257]. The surface coverage is calculated as $\theta_s = N_{\mathrm{C}}/N_{\mathrm{ads}}(a \times b)$, where N_{C} is the number of adsorbed C atoms, N_{ads} is the total number of adsorption sites for the facet, and $(a \times b)$ is the size of the supercell. Hence, $\theta_s = 0.125$ ML for one C adsorbed on a Ni(111)-(2×2) surface, whereas $\theta_s = 1$ ML for graphene.

For 0.25 ML, a C dimer (atoms on the hcp and fcc sites) is energetically more favorable, binding 0.25 eV/C stronger to the surface than the monomer. The C trimer is favored for 0.375 ML, binding 0.12 eV/C stronger to the surface than the dimer. The two atoms at the hcp site are at 1.56 Å and the middle atom is at 1.97 Å distant from the surface, forming a 123° bond angle. At 0.5 ML, the most stable structure forms an infinite zigzag chain, at the hcp and fcc site, which is stronger than the trimer by 0.28 eV/C. Increasing coverage to 0.75 ML, results on a chain of benzene rings, which binds stronger than the zigzag chain by 0.31 eV/C and appears to be sinking into the metal (Fig. 6.10, side view 0.75 ML) as one of the top Ni atoms (lighter

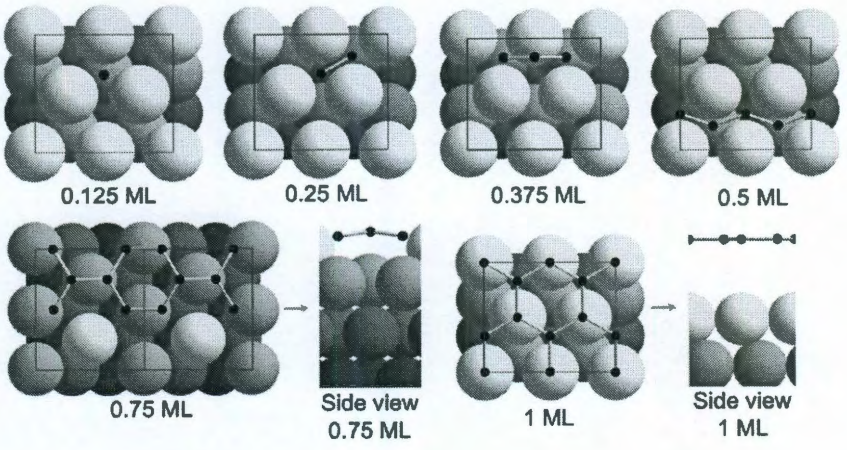

Figure 6.10 : Relaxed structures for increasing carbon coverage on Ni(111)-(2 × 2) surface. The box indicates the supercell, whereas the orange arrows show the direction of the side views. Color key: Ni - blue, C - black, darker atoms are farther from the surface.

blue) move outward. Finally, a graphene overlayer (top and fcc sites) forms at full coverage, binding 0.68 eV/C stronger than at 0.75 ML. Similar trend was observed experimentally by Takeuchi et al. [232], in which the binding energy increased from 6.89 eV/C, at 0.5 ML, to 7.07 eV/C, at 0.9 ML, Table 6.2.

The change of Ni-C binding energy with C coverage was also analyzed for the (110) and (100) surfaces, Fig. 6.11. Whereas the binding energy increases with C coverage for (111), it decreases for (110) and (100). At first, as the coverage increases, there is a preference for maximizing the C-C interaction distance. For the (100), at 0.5 ML the atoms adsorb at the hollow site, as it did at 0.25 ML, but 0.52 eV/C weaker binding energy. Like in the (111), the trimer is favored for the configuration with three C atoms and a zigzag chain for the one with four C atoms, the binding energy decreasing 0.36 and 0.23 eV/C, respectively, as the atoms move away from the surface. For the (110), there is always two atoms at the long-bridge sites, which eventually

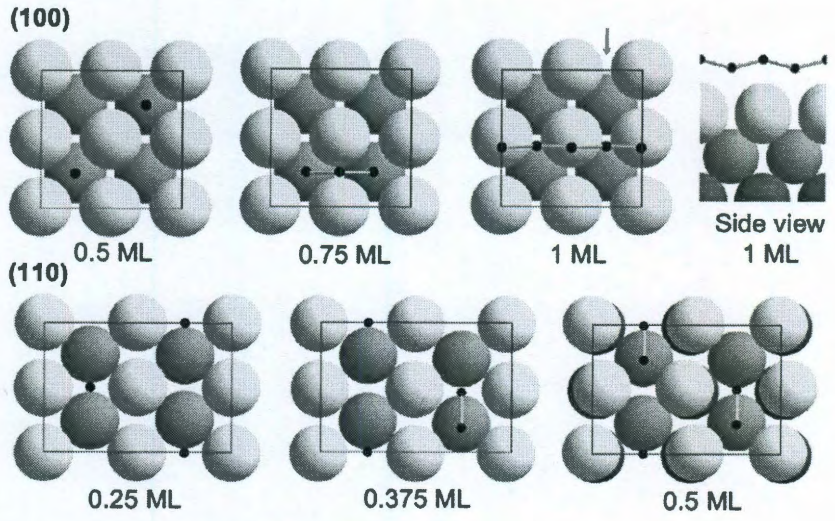

Figure 6.11 : Relaxed structures for increasing carbon coverage on Ni(110)- and (100)-(2 × 2) surface.

form a dimer with a second atom on the hollow site. The binding energy has only a small variation, decreasing 0.02 eV/C at 0.25 ML, 0.18 eV/C at 0.375 ML, and 0.03 eV/C at 0.5 ML. No C adsorbed on Ni(110) surface was observed beyond 0.5 ML, and there are no known structures for C high coverage on Ni(110). However, at 0.5 ML a clock-wise reconstruction of the Ni layer co-planar with the C adsorbed can be seen, similarly to the one which was observed by scanning tunneling microscopy under certain experimental conditions [258, 259]. The stress induced by adsorbed C on the Ni surface is minimized by such reconstruction.

6.5.2 Surface energy

The slab thicknesses and number of k-points necessary to obtain representative calculations limit the use of *ab initio* methods. Therefore, the C chemisorption was studied on the low-index surfaces, (111), (100), and (110), by first-principles and its

results were compared with calculations using ReaxFF. The energy of the Ni surfaces upon C adsorption is calculated as

$$\gamma = \frac{1}{A}(\tilde{E}_b + \mu_{\text{graphene}}) + \gamma_0, \tag{6.6}$$

where the average binding energy $\tilde{E}_b$ is the difference per C atom between the clean surface and the surface with adsorbed carbon.

The surface energy (γ) values obtained from the *ab initio* simulations show a trend in reduction of γ anisotropy at high-C coverage, Fig. 6.12(a). In general, the surface energy decreases with C adsorption. In the case of Ni(111), this initial decrease is followed by a increase when the graphene layer moves away from the surface. Though no C was adsorbed on the Ni(110) beyond 0.5 ML, the γ remains almost invariant, close to the value for 1 ML on (111). Calculations using ReaxFF yield a similar trend, Fig. 6.12(b). Here, one can assume that at high temperature and upon C adsorption, the surface energy anisotropy is eliminated. Based on such assumption, an idealized Ni Wulff-construction in which γ is isotropic is plotted, Fig. 6.12(c). The result is a polyhedron that is very close to a spherical shape.

The γ is calculated for the high-index Ni surfaces, (211), (210), and (311), using ReaxFF. The resulting Ni equilibrium shape reveals a much more rounded, spherical, shape than the one for the clean surfaces, Fig. 6.13(a). For the (211), γ decreases from 0.131 to 0.124 eV/Å^2. However, in (311) γ presents only a small variation upon C adsorption, from 0.133 to 0.129 eV/Å^2, whereas in (210) it remains constant at 0.138 eV/Å^2. Although such small variations are within the accuracy of the simulations, the resulting crystal shape describes well the reshaping that the Ni clean catalyst, Fig. 6.13(b), undergoes under carburizing atmosphere, Fig. 6.13(c) [254], and strongly resemble the idealized Ni Wulff-construction for isotropic γ shown in Fig. 6.12(c).

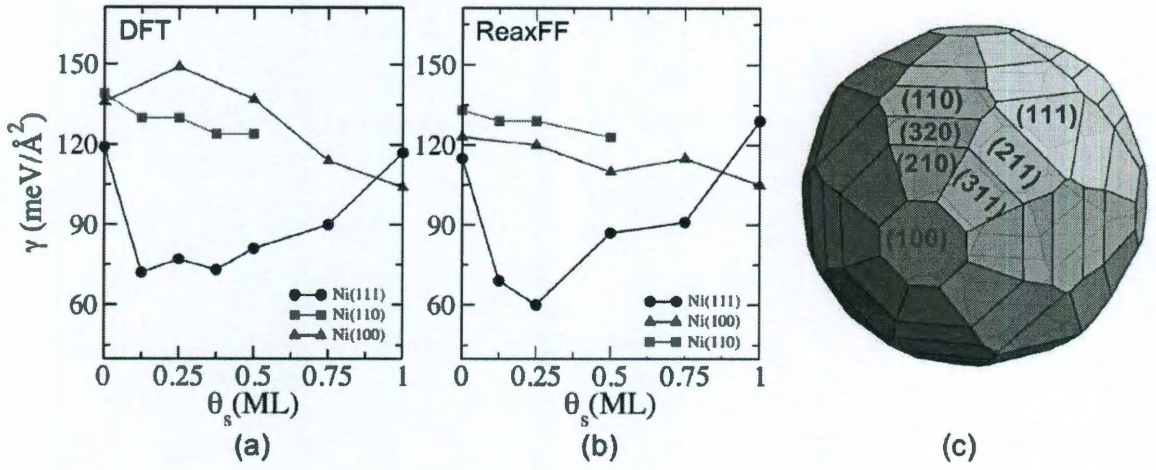

Figure 6.12 : Surface energy (γ) at various carbon coverages (θ) on the Ni low-index surfaces, calculated by (a) first-principles and (b) reactive force field. (c) Idealized Ni equilibrium crystal shape for isotropic γ.

6.6 Phenomenological model for CNT lift-off

It is clear that the catalyst crystal shape has a significant role during CNT growth. Although some studies have described the changes the crystal surface undergoes upon C adsorption, as seen above, there has been no analysis on the role of the catalyst reshaping on the CNT growth yet.

Based on the simulations described in the previous section and experimental observations of carburized Ni catalyst [254, 255], it is reasonable to assume that the C adsorbed and high temperature will eliminate the surface energy anisotropy, $\gamma(\theta) \simeq const.$ A continuum approximation of the catalyst and cap system would look like the schematics shown in Fig. 6.14(a), in which the catalyst is represented by a sphere of radius R_0. As shown by the simulations of C adsorption on Ni(111), an increase in coverage leads to sp^2 graphene formation, which is then connected to the metal through weak van der Waals forces (d_0 is the equilibrium distance between cap

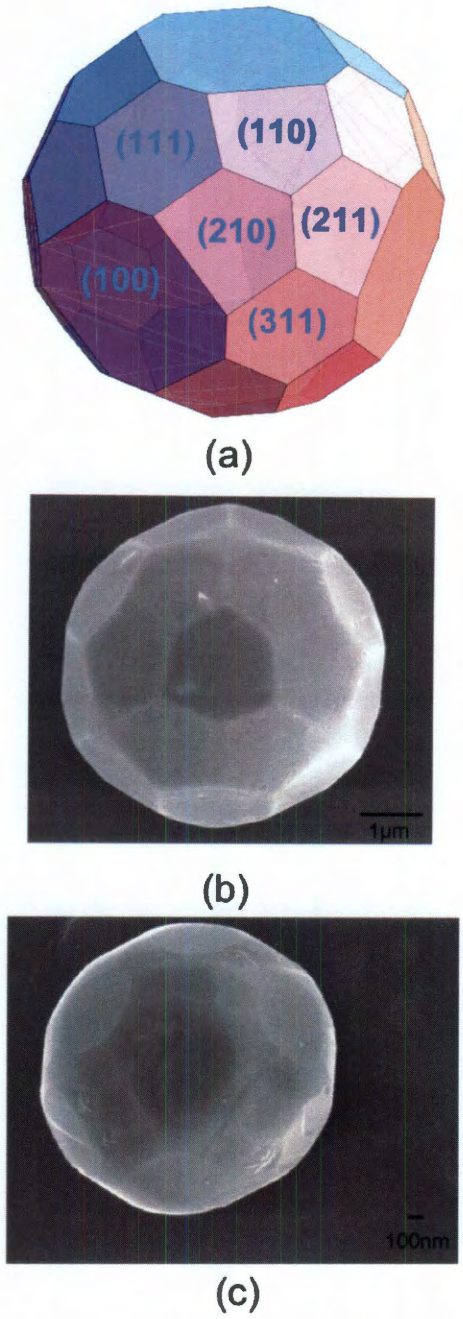

Figure 6.13 : (a) Ni equilibrium crystal shape calculated using reactive force field at 1 ML coverage. (b) Near-equilibrium shape of pure nickel crystals and (c) of Ni under carburizing atmosphere; both annealed at 1200 °C. (b)-(c) Reprinted with permission from [253]. Copyright 2009 Taylor & Francis.

and catalyst). For the Ni(111), the surface energy decreases with carbon adsorption on the metal. Similarly, the surface right under the cap in Fig. 6.14(a), does not have any adsorbed C after the cap lifts-off and its surface energy is the same as for a pristine metal γ_0. Outside the cap, however, C is still adsorbed, hence the surface energy γ. The energetics of the system is then governed by the relation γ/γ_0 and, as discussed next, so does the lift-off.

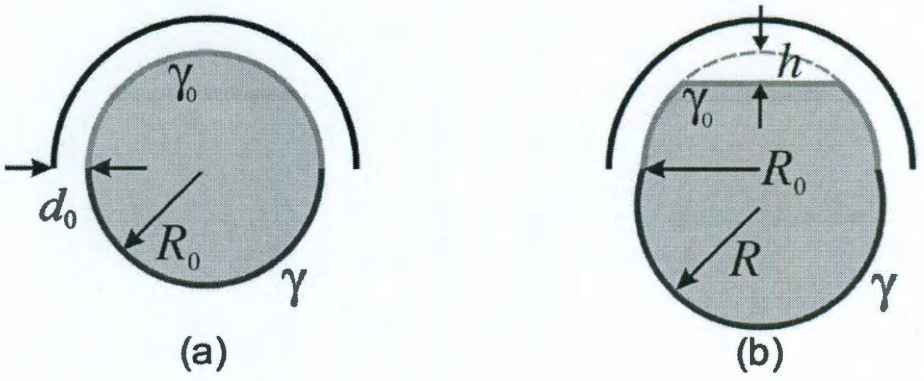

Figure 6.14 : Continuum representation of the catalyst and cap system: (a) initial geometry and (b) at the moment of catalyst reshaping.

Hence, the cap lift-off is associate with a reduction of the surface area underneath the cap, such that the catalyst is truncated by h, Fig. 6.14(b), for $0 \leqslant h \leqslant R_0$. Due to volume conservation, the excess of metal shifts to outside the cap such that $R > R_0$. The volume varies between 0 and $V_0/2 \equiv 4\pi R_0^3/6$, whereas the radius of the hemisphere $R = R(h; R_0)$ results from volume conservation,

$$V_0(R) - v_{h'}(R) = V_0(R_0)/2 + v_h(R_0), \tag{6.7}$$

where $v_h(R) = \pi h^2(3R - h)/3$ and $v_{2R}(R) = V_0(R)$, and geometrical considerations,

$$h'(2R - h') = R_0^2. \tag{6.8}$$

The driving force of the lift-off process is then given by

$$\Delta E(h, \gamma/\gamma_0) = \delta E_{\text{surf}}(h, \gamma/\gamma_0) + \delta E_{\text{vdW}}(h), \tag{6.9}$$

where the first term in right-hand side of the equation represents the change in the total surface energy of the particle due to reshaping and the second term reflects the change in the attractive van der Waals cap-catalyst interaction.

As a result of the lift-off, the distance d between the catalyst and the cap increases, hence $\delta E_{\text{vdW}}(h) > 0$. ΔE is calculated using $R_0 \simeq 1.1$ nm, $d_0 = 0.2$ nm, and 40 meV/C van der Waals attractive energy [260]. In the resulting $\Delta E(h, \gamma/\gamma_0)$ surface, Fig. 6.15, the boundary line defined by $\Delta E(h, \gamma/\gamma_0) = 0$, projected onto the (h, γ) plane, divides the (h, γ) plane into two domains. According with the choice of parameters, the continuum model proposed above is justified, as $\Delta E < 0$. At $\gamma/\gamma_0 \lesssim 0.6$ the catalyst reshaping is then favored.

The relation γ/γ_0 is easily obtained from the results shown in Fig. 6.16. Both DFT and ReaxFF calculations indicate that the relation between the clean and C-covered surface energies at low-C coverage is within the catalyst reshaping zone, Fig. 6.16, supporting the phenomenological model assumptions.

Based on experimental evidence [174, 175, 213, 214], MD simulations and the analysis regarding Ni catalyst reshaping discussed above, it is possible to suggest that the CNT growth follows an oscillatory mechanism, Fig. 6.17. Hence, after a complete cap nucleates and lift-off, the metal catalyst retracts from within the cap (1). The elongation of the tube (2) is done by addition of new C atoms to the edge of the cap, which is facilitated by the close contact with the catalyst, while the cluster reshaping and retraction progresses. The cycle starts over as a new cap nucleates inside the previous tube (3). Thus, (1)$\rightarrow$ (2) $\rightarrow$ (3) $\rightarrow$ (2)$\cdots$(3) progress until the catalyst becomes inactive.

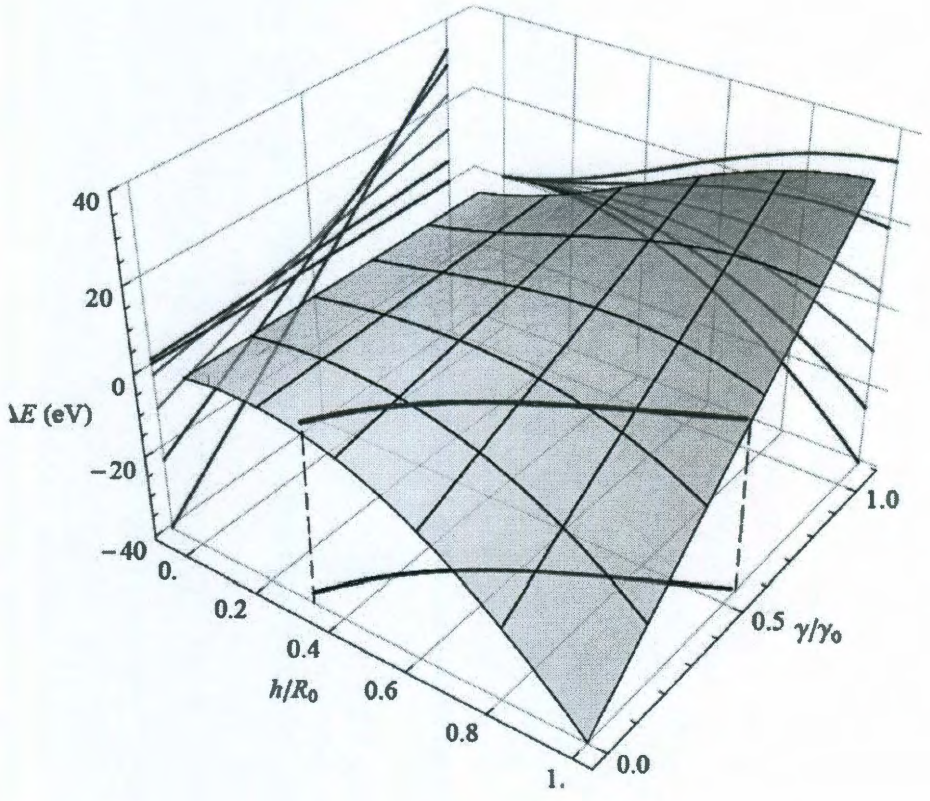

Figure 6.15 : Change in energy ΔE for cap lift-off as a function of catalyst reshaping h/R_0 according with the change in surface energy γ/γ_0 due to carbon adsorption.

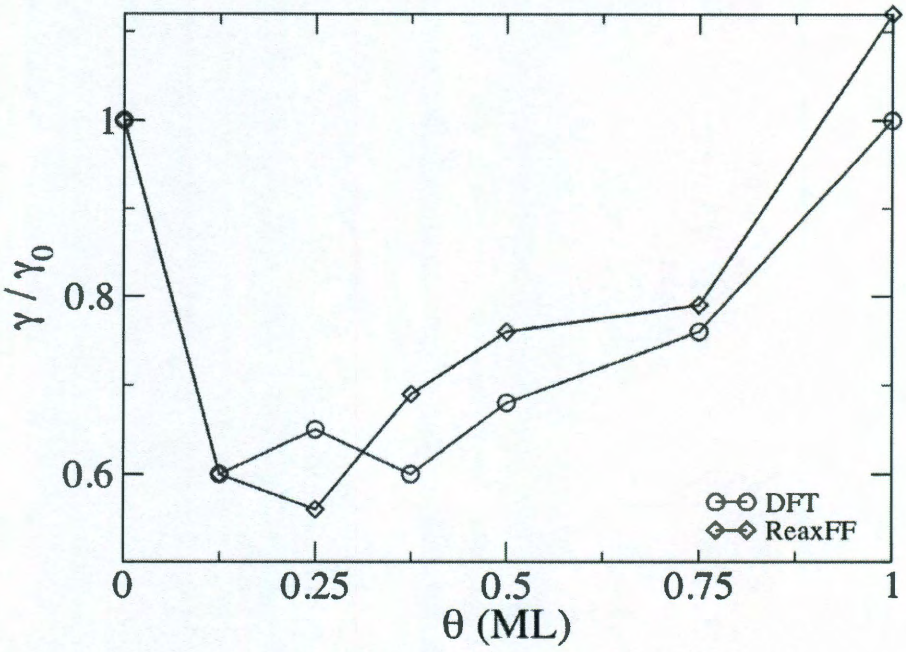

Figure 6.16 : Change in surface energy γ/γ_0 due to the carbon adsorption, for increasing coverage θ of the Ni (111) surface.

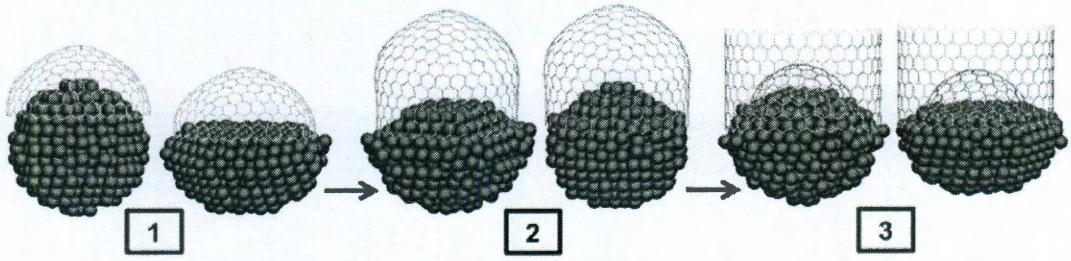

Figure 6.17 : Oscillatory mechanism for carbon nanotube growth: Cap nucleation and lift-off (1), elongation (2), and N caps nucleation and lift-off (3) are driven by the catalyst reshaping.

6.7 Conclusions

Catalyst type and shape can be used to gain better control over CNT growth. Here, metallic catalyst alloying is used for precisely tuning metal catalyst properties. The binding energy of Ni-Fe catalyst to the CNT is chirality selective, whereas the catalyst-CNT binding can be fine tuned through the inverse relation between E_b and Cu atomic fraction for Cu_xFe_y. The Ni catalyst reshaping is studied through the surface energy variation upon C adsorption. The Ni equilibrium crystal shape is initially faceted, in which (111), (100), (110), (210), and (311) surfaces are visible. The C adsorption reduces the surface energy anisotropy, which results in more rounded Wulff-construction. Thereby, a continuum phenomenological model is formulated, in which the catalyst is assumed as a sphere, which dynamically reshapes at $\gamma/\gamma_0 \lesssim 0.6$.

Chapter 7

Conclusions

This thesis explains the growth of graphitic structures and functionalized graphene at nano-scale in three important catalytic processes, viz., graphene hydrogenation and fluorination, and carbon nanotube (CNT) growth, through empirical potentials and *ab initio* simulations. It is shown here that the formation of hydrogenated graphene, i.e., graphane, facilitates the process of hydrogen spillover. Whereas the reversibility of graphane formation is welcome for developing hydrogen storage applications, it is undesirable for electronic applications. It is shown here that fluorination of graphene, instead, forms thermodynamically favorable phases without a nucleation barrier. In CNT synthesis, the catalyst properties, as defined by its type and shape, have an important role for achieving controllable CNT growth. It is shown here that alloyed nanocatalysts can be used to precisely tune the metal-tube interaction and that catalyst reshaping results from a reduction in the surface energy anisotropy upon carbon adsorption. These results are summarized next.

7.1 H-Spillover through the catalyst saturation

1. Thermodynamic spillover of hydrogen occurs from a metal cluster to the hydrogenated graphene, either for freestanding or supported clusters. The details of hydrogen binding to the catalyst particle are reported here, serving as a gateway to the entire process in which the catalyst saturation is also an important

aspect of spillover.

2. For the spillover of an H to occur from the metal, the chemical potential μ_H must exceed the CH state energy level, before the metal cluster saturates (i.e., becomes unable to further accept new H_2 molecules). *Ab initio* computations reveal how the gradual energy change of H on the catalyst fits between the energy on the receptor and as free gas. The hydrogen uptake process on free unsupported, relatively small, four-atom Ni and Pd clusters is performed. It is indeed observed that the spillover process does not require full saturation of the cluster, because thermodynamically the spillover becomes favorable even before a cluster saturates.

3. Pristine graphene and graphane are used as support to the cluster to study the thermodynamic possibility of the spillover. The graphane phase facilitates the spillover process by significantly improving the C-H binding, though it is energetically unfavorable for the spillover to occur on pristine graphene.

4. Although it is more favorable for H to be in the hydrogenated phase than on the saturated catalyst, there are still barriers involved for the motion of the H. The migration barrier for the hydrogen to migrate from the metal cluster to the hydrogenated phase is calculated using the nudged elastic band method. The small observed energy barrier (0.68 eV) suggests that the spillover can easily occur below room temperature. These findings are in agreement with recent experiments, in which H-uptake via the spillover increases with the temperature and the reduction of the substrate [261].

5. Besides providing here the first explanation of the nano-thermodynamics of hydrogen spillover, it is shown that optimum C-H bonding can be used as an

indication of materials in which the spillover can be achieved more effectively. Any modification of the receptor that leads to an increase in this energy, within its reversibility limit, will also enhance the spillover.

6. The incorporation of defects, curvature, and dopants are a few of the potential routes to facilitate nucleation by improving the C-H binding. For example, this has been demonstrated for graphene where the energy of hydrogenation changes drastically by Stone-Wales type of defects [262].

7.2 Fluorinated graphene: Patterning nanoroads and quantum dots

1. Like graphane phase, the sp^3 fluorinated graphene phase, which is investigated here by *ab initio* methods, is semiconducting. The process of graphene fluorination results in wide band gap semiconductors (CF, C_2F, and C_4F), in which higher F coverage is favored.

2. The graphene fluorination is found to be different from its hydrogenation, as it occurs without a nucleation barrier. This is partially due to the higher affinity of fluorine towards carbon atoms.

3. Through patterning of the chemically functionalized graphene, both semiconducting (i.e., fluorinated graphene) and metallic elements (i.e., graphene) can be combined on the same graphene sheet for use in electronic applications. Thereby, the suitability of the fluorinated graphene as a host material for graphene nanoroads and quantum dots is analized here.

4. Graphene nanoroads are formed by removing F atoms from a fully fluorinated

graphene either along armchair (AC) dimers (N_{ac}) or zigzag (ZZ) chains (N_{zz}) to form pristine graphene roads. The nanoroads with AC orientation are semiconducting with large band gaps, following a non-monotonic trend with the width, in which $\Delta_{N_{ac}=3p+2} < \Delta_{N_{ac}=3p+1} < \Delta_{N_{ac}=3p}$ (except for $N_{ac} = 3$ and 4). The nanoroads with ZZ edge are semiconducting or semi-metallic according to their spin orientation; antiferromagnetic or ferromagnetic, respectively. The band gap in ZZ roads is inversely proportional to the width, $\sim 1/N_{zz}$.

5. The quantum dots are defined here as small graphitic islands of connected n sp^2 C atoms created by the removal of the F atoms from CF and C_4F finite cluster or infinite sheet. Their thermodynamic feasibility is studied by analyzing several possible configurations and observing how quantum confinement affects their electronic properties. The formation energy of the quantum dots depends on their size as $E(n) - E(\infty) \sim \text{const}/\sqrt{n}$. The quantum dots in fluorinated graphene exhibit orientation-, width-, and F coverage-dependent electronic properties. Tight-binding methods are used to explore large edge-specific quantum dots. The band gaps of the larger quantum dots follow a $1/R$ trend similar to the confinement of Dirac fermions, where $R \sim \sqrt{n}$. The band-decomposed electron densities of 2-D quantum dot arrays in CF and C_4F show atom-like states with very good electron confinement.

6. Note that the ability to explore larger systems, as the large edge-specific quantum dots shown in Fig. 4.6, is possible only by using multi-scale methods, viz., *ab initio* and tight-binding. Similar studies can be carried out to investigate the effect of other functional groups (e.g., Br, Cl) on the electronic properties of graphene.

7. Current developments in techniques for the functionalization of graphene should make the patterns shown here an experimental possibility in near future. These patterns can serve as building blocks, which can be formed on different phases of fluorinated graphene (as shown here for CF and C_4F), opening the door to a range exciting of applications.

7.3 Nanotube nucleation versus carbon-catalyst adhesion

1. Understanding carbon nanotube cap lift-off is a crucial part of carbon nanotube growth research. Until now, all three available models, viz., adhesion versus curvature energy balance, decohesion by thermal kinetic energy, and requirement of fast C diffusion, had different predictions on what is the driving force behind cap lift-off. Hence, catalyst encapsulation is studied here as a function of work of adhesion, temperature, and consequently the C diffusion rate, by classical molecular dynamics (MD) simulations.

2. Although the potential energy surface of classical MD simulation is considered less accurate when compared with first-principles or tight-binding approximation based MD, it permits to run trajectories many orders of magnitude longer, which is critical to reasonably simulate the single-wall carbon nanotube (SWNT) growth process. Besides, its flexibility of adjustable parameters can be used to gain insight into the role of a specific parameter, as is the case here, in which α_{MC} is varied to tune the Ni-C interaction.

3. The nucleation, lift-off, and tube lengthening can be observed through MD simulations. Starting from a pure Ni cluster, at high enough temperature and low work of adhesion (W_{ad}), the carbon atoms dissolve in the catalyst and then

precipitate to its surface, to later nucleate into carbon chains and polygons. Eventually a carbon island or carbon cap is formed and lifts-off, to then grow longer and longer in a repeatable manner. At the same temperature, but at high W_{ad}, although the initial nucleation steps are identical, the cap lift-off does not occur. Instead, the graphitic cap grows larger and larger until it covers the whole surface of the catalyst, encapsulating it. At very low temperature and low W_{ad} the C diffusion is extremely slow and most of the catalyzed C atoms just stay on the initial position. As a consequence, C chains and small islands may form everywhere around the catalyst surface, but their limited mobility (ability to diffuse) leads to catalyst encapsulation.

4. Unfortunately, as in previously simulated nanotubes, there is a number of defects (pentagons and heptagons) which frequently appear on the tube wall in such a way that we are not able to assign it a pair of (n, m) chiral indexes. However, this may be a consequence of the limited simulation time (of the order of tens of nanoseconds) when compared with real experiments (of the order of seconds).

5. Through systematic analysis of hundreds of MD simulations, a comprehensive picture of the CNT growth versus catalyst encapsulation is introduced here. It is composed of two distinct regions: i) High temperature ($>$ 600 K), where catalyst encapsulation depends on work of adhesion, and ii) low temperature ($<$ 600 K), or strongly temperature dependent, where limited C diffusion hinders cap localization and lift-off for growth.

6. The relationship between W_{ad} and T, permits an informed choice of parameters to obtain the longest SWNT (up to $\sim$13 nm) produced in any MD simulation

up to date. Such accomplishment of steady uninterrupted growth within reasonable simulation times represents a significant step of achieving realistic CNT computational modeling.

7. The simulations also show that SWNT growth is strongly dependent on work of adhesion and C diffusion at very low temperatures (e.g., 273 K). Based on this analysis, it is suggested that experimental low SWNT growth temperatures can be achieved through use of catalysts with low work of adhesion. This is critically important not only from a general process efficiency point of view, but especially for possible *in situ* growth for nanoelectronics applications.

7.4 Effect of catalyst type and shape on CNT growth

1. It is shown here that the catalyst type and shape have an important role during CNT growth: (i) Controllable catalytic CNT growth can be achieved by precisely tuning metal catalyst properties through alloying and (ii) CNT cap nucleation mechanism originates from catalyst reshaping.

2. Bimetallic M_xFe_y nanocatalysts, where M = Ni and Cu, x =0.23 and 0.77, and $y = 1 - x$, are investigated here through *ab initio* calculations. The use os such catalysts to fine tune the catalyst-CNT interaction is analyzed for chirality selective CNT growth. The binding energy (E_b) of Ni_xFe_y to the CNT is chirality selective for AC or ZZ edges. For Cu_xFe_y, the catalyst-CNT binding can be fine tuned through the inverse relation between E_b and Cu atomic fraction, which can also be beneficial to CNT selective production (e.g., length).

3. Molecular dynamics simulations using large metal clusters (500 atoms) provide a good qualitative picture of the CNT growth, including catalyst reshaping and

incipient double-wall formation. However, after the C atoms start depositing on the catalyst, the different facets are indistinguishable. Here, this is overcome through studying the Ni individual surface energies and its variation upon C adsorption.

4. The surface relaxation and energy of low- {111}, {100}, and {110}, and high-index {211}, {210}, {311}, and {320} Ni surfaces are studied by first-principles for various slab thicknesses. Although the low-index surface properties converge for slabs $>$ 6 Å, the high-index surfaces require slabs $>$ 12 Å. The Ni(111) has the lowest surface energy, being also the dominant facet on the resulting Ni equilibrium crystal shape. Other visible facets are (100), (110),(210), and (311).

5. The effect of C adsorption on the low- and high-index surfaces is studied by first-principles and a reactive force field. The resulting equilibrium crystal shape suggests a significant reduction of the surface energy anisotropy, which results in more rounded, spherical, Ni equilibrium crystal shape.

6. Based on such evidence, a continuum phenomenological model describing the effect of the catalyst reshaping upon C adsorption is formulated, in which the catalyst is assumed as a sphere, which dynamically reshapes at $\gamma/\gamma_0 \lesssim 0.6$.

7. It is suggested that the CNT growth follows an oscillatory mechanism. Hence, after a complete cap nucleates and lift-off, the metal catalyst retracts from within the cap (1). The elongation of the tube (2) is done by addition of new C atoms to the cap's edge, which is facilitated by the close contact with the catalyst, while the cluster reshaping and retraction progresses. The cycle starts over as a new cap nucleates inside the previous tube (3). Thus, resulting into

an oscillatory mechanism in which (1)→ (2) → (3) → (2)$\cdots$(3) progress until the catalyst becomes inactive.

Appendix A

Varying W_{ad} in MD simulations

During each molecular dynamics (MD) simulation of the carbon nanotube (CNT) growth, there are two possible outcomes: cap nucleation and lift-off or cap nucleation and catalyst encapsulation. Specially near the equilibrium, represented by the line dividing the cap lift-off and catalyst encapsulation in Fig. 5.7b, the same set of initial conditions may result in both lift-off and catalyst encapsulation.

Thus, in order to obtain statistical results at least five MD simulations were performed for each temperature (600–1400 K, at 200 K intervals) and various work of adhesion (W_{ad}) values. The number of times each simulation results in either CNT growth or encapsulation is recorded and showed in the statistical plots of Fig. 5.7a. The complete set of the simulations outcome is showed in Fig. A.1 to Fig. A.5.

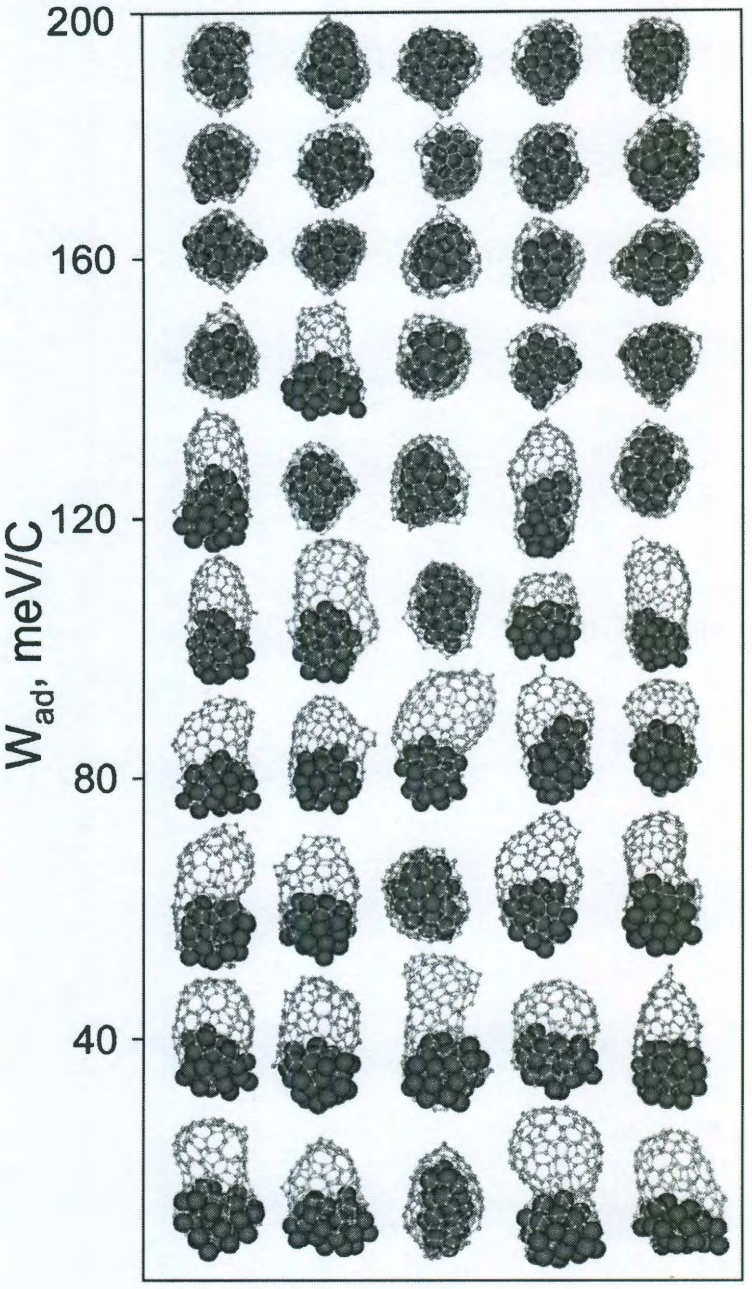

Figure A.1 : MD simulations at 600 K, at different levels of metal-carbon interaction.

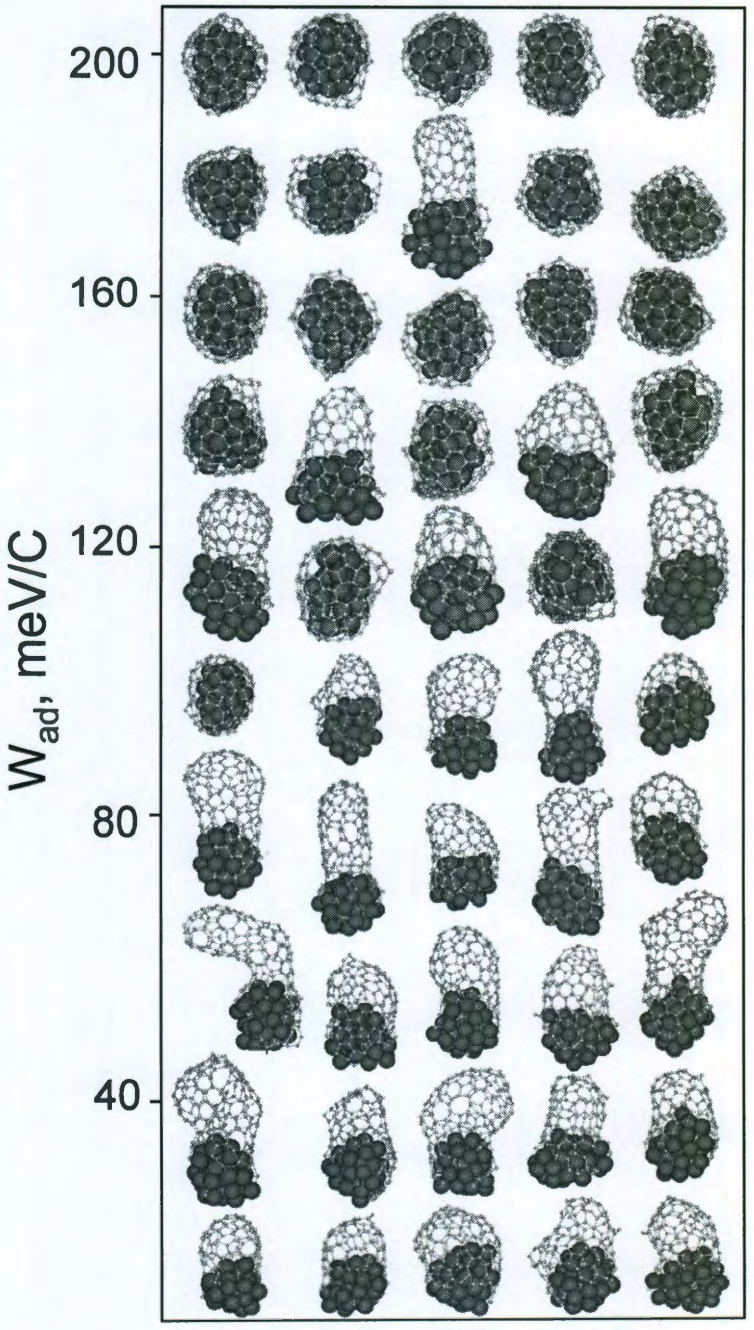

Figure A.2 : MD simulations at 800 K, at different levels of metal-carbon interaction.

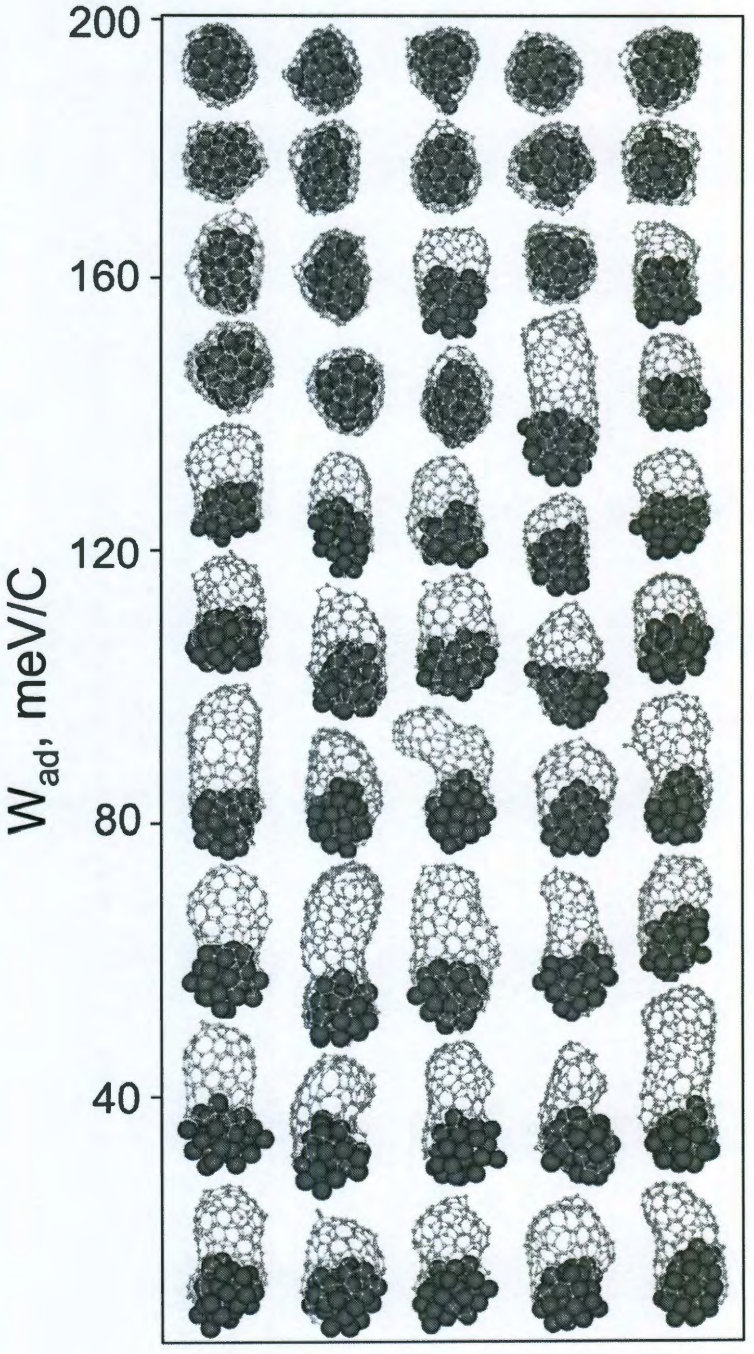

Figure A.3 : MD simulations at 1000 K, at different levels of metal-carbon interaction.

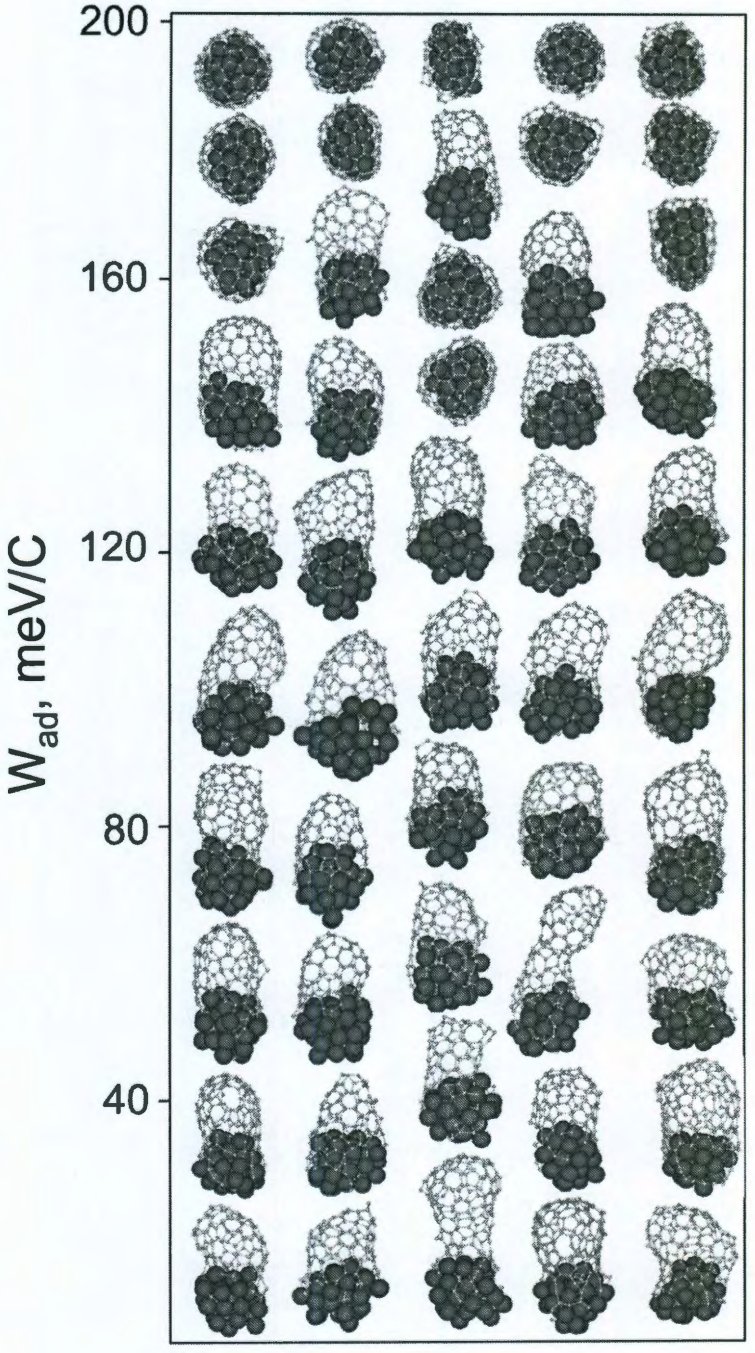

Figure A.4 : MD simulations at 1200 K, at different levels of metal-carbon interaction.

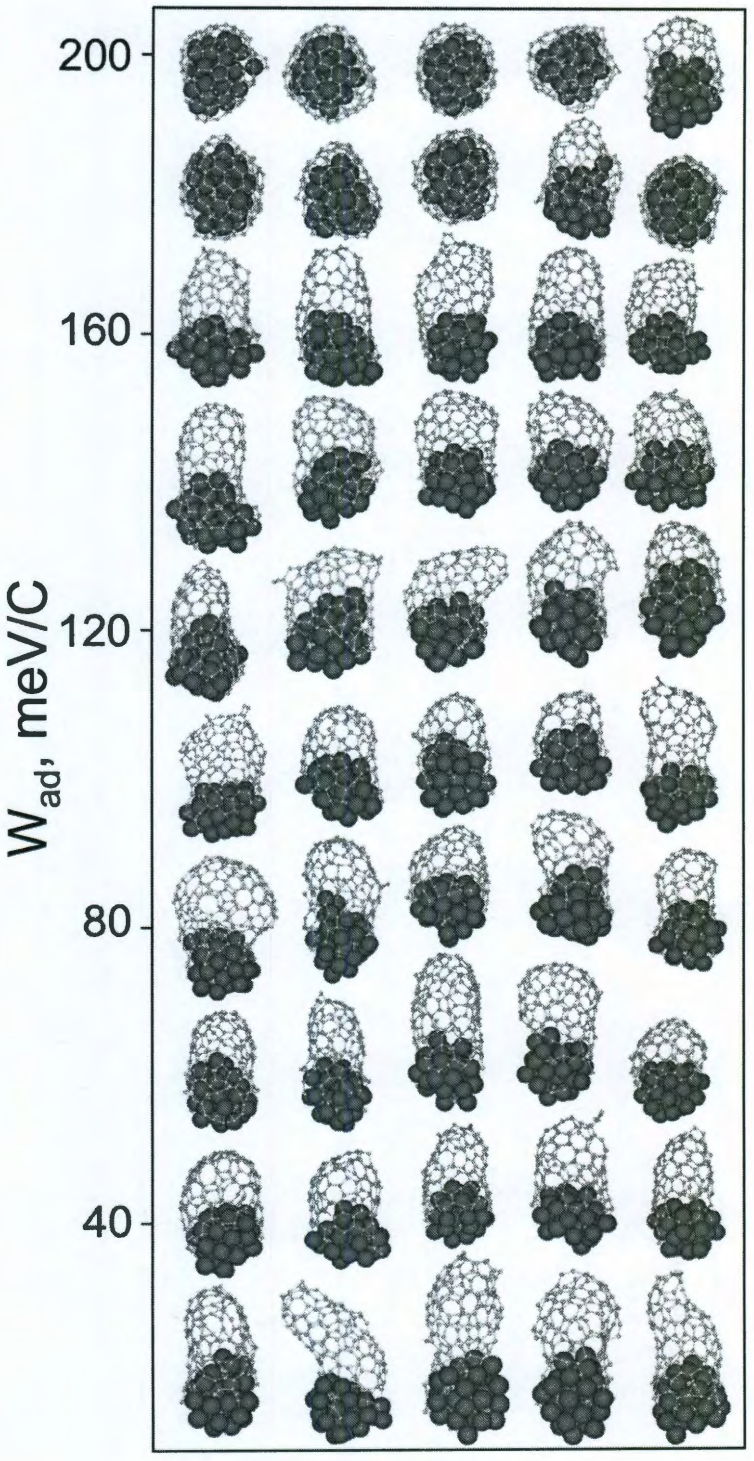

Figure A.5 : MD simulations at 1400 K, at different levels of metal-carbon interaction.

Appendix B

Structural arrangement of CNT on bimetallic catalysts

Several arrangements of the open single-wall carbon nanotube on the bimetallic catalyst (most stable structure) are possible. The most stable configuration is given by the largest binding energy (E_b), as shown in Fig. B.1 for Ni_xFe_y and Fig. B.2 for Cu_xFe_y.

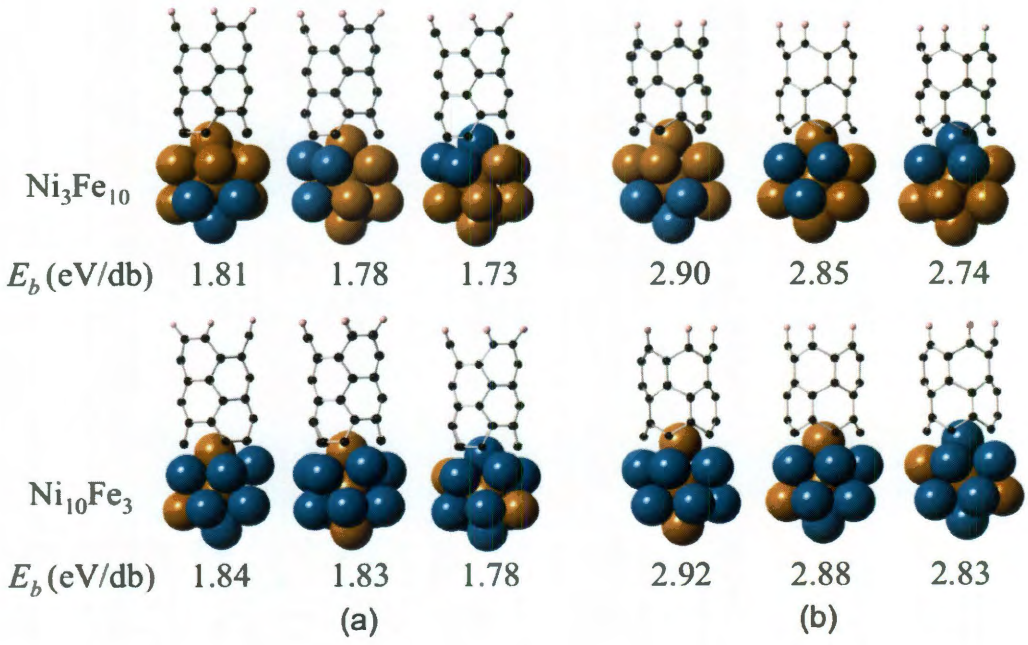

Figure B.1 : Possible arrangement of the bimetallic Ni_xFe_y catalyst with respect to the (a) (3,3) and (b) (5,0) open single-wall carbon nanotube and the respective binding energies (E_b). Ni and Fe atoms are blue and brown, respectively.

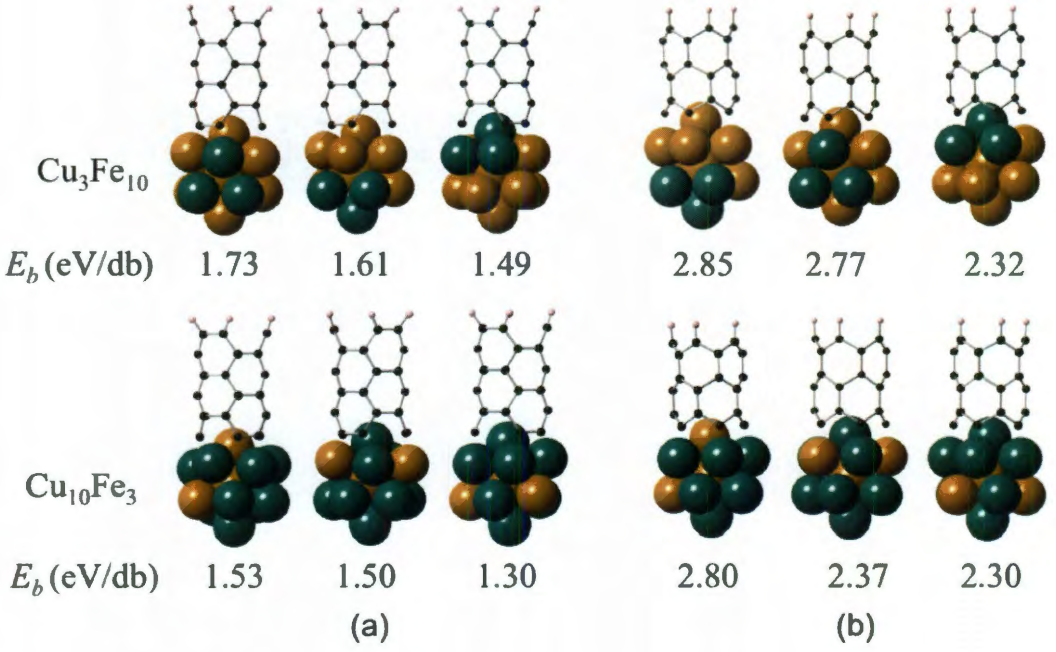

Figure B.2 : Possible arrangement of the bimetallic Cu_xFe_y catalyst with respect to the (a) (3,3) and (b) (5,0) open single-wall carbon nanotube and the respective binding energies (E_b). Cu and Fe atoms are green and brown, respectively.

Bibliography

[1] A. K. Singh, M. A. Ribas, and B. I. Yakobson, "H-spillover through the catalyst saturation: An ab initio thermodynamics study," *ACS Nano*, vol. 3, no. 7, pp. 1657–1662, 2009.

[2] M. A. Ribas, A. K. Singh, P. B. Sorokin, and B. I. Yakobson, "Patterning nanoroads and quantum dots on fluorinated graphene," *Nano Res.*, vol. 4, no. 1, pp. 143–152, 2011.

[3] E. Muñoz, A. K. Singh, M. A. Ribas, E. S. Penev, and B. I. Yakobson, "The ultimate diamond slab: Graphane versus graphene," *Diam. Relat. Mat.*, vol. 19, pp. 368–373, 2010.

[4] M. A. Ribas, F. Ding, P. B. Balbuena, and B. I. Yakobson, "Nanotube nucleation versus carbon-catalyst adhesion–probed by molecular dynamics simulations," *J. Chem. Phys.*, vol. 131, no. 22, p. 224501, 2009.

[5] S. Tabatabaei, M. A. Ribas, A. Kumar, and P. M. Ajayan, "Selective synthesis of Ag-Ni alloy nanoparticles by chemical reduction at room temperature." In preparation.

[6] M. A. Ribas, K. Bets, E. S. Penev, and B. I. Yakobson In preparation.

[7] E. Pigos, E. S. Penev, M. A. Ribas, R. Sharma, B. I. Yakobson, and A. R. Harutyunyan, "Carbon nanotube nucleation driven by catalyst morphology dy-

namics." In preparation.

[8] H. W. Kroto, J. R. Heath, S. C. O'Brien, R. F. Curl, and R. E. Smalley, "C_{60}: Buckminsterfullerene," *Nature*, vol. 318, no. 6042, pp. 162–163, 1985.

[9] A. Hirsch, "The era of carbon allotropes," *Nat. Mater.*, vol. 9, no. 11, pp. 868–871, 2010.

[10] W. Kratschmer, L. D. Lamb, K. Fostiropoulos, and D. R. Huffman, "Solid C_{60}: a new form of carbon," *Nature*, vol. 347, no. 6291, pp. 354–358, 1990.

[11] H. W. Kroto, "The stability of the fullerenes C_n, with n = 24, 28, 32, 36, 50, 60 and 70," *Nature*, vol. 329, no. 6139, pp. 529–531, 1987.

[12] S. Iijima, "Helical microtubules of graphitic carbon," *Nature*, vol. 354, pp. 56–58, 1991.

[13] R. Saito, M. Fujita, G. Dresselhaus, and M. S. Dresselhaus, "Electronic structure of chiral graphene tubules," *Appl. Phys. Lett.*, vol. 60, no. 18, pp. 2204–2206, 1992.

[14] M. S. Dresselhaus, G. Dresselhaus, and P. C. Eklund, *Science of Fullerenes and Carbon Nanotubes.* Academic Press, 1996.

[15] A. K. Geim and K. S. Novoselov, "The rise of graphene," *Nat. Mater.*, vol. 6, no. 3, pp. 183–191, 2007.

[16] A. J. Van Bommel, J. E. Crombeen, and A. Van Tooren, "LEED and Auger electron observations of the SiC(0001) surface," *Surf. Sci.*, vol. 48, no. 2, pp. 463–472, 1975.

[17] J. W. May, "Platinum surface LEED rings," *Surf. Sci.*, vol. 17, no. 1, pp. 267–270, 1969.

[18] K. S. Novoselov, A. K. Geim, S. V. Morozov, D. Jiang, Y. Zhang, S. V. Dubonos, I. V. Grigorieva, and A. A. Firsov, "Electric field effect in atomically thin carbon films," *Science*, vol. 306, pp. 666–669, October 2004.

[19] P. Avouris, "Graphene: Electronic and photonic properties and devices," *Nano Lett.*, vol. 10, pp. 4285–4294, 2010.

[20] K. S. Kim, Y. Zhao, H. Jang, S. Y. Lee, J. M. Kim, K. S. Kim, J. H. Ahn, P. Kim, J. Y. Choi, and B. H. Hong, "Large-scale pattern growth of graphene films for stretchable transparent electrodes," *Nature*, vol. 457, pp. 706–710, 2009.

[21] A. Reina, X. Jia, J. Ho, D. Nezich, H. Son, V. Bulovic, M. S. Dresselhaus, and J. Kong, "Large area, few-layer graphene films on arbitrary substrates by chemical vapor deposition," *Nano Lett.*, vol. 9, no. 30–35, 2009.

[22] T. W. Ebbesen and P. M. Ajayan, "Large-scale synthesis of carbon nanotubes.," *Nature*, vol. 358, pp. 220–222, 1992.

[23] C. Journet, W. K. Maser, P. Bernier, A. Loiseau, M. L. de la Chapelle, S. Lefrant, P. Deniard, R. Lee, and J. E. Fischer, "Large-scale production of single-walled carbon nanotubes by the electric-arc technique," *Nature*, vol. 388, no. 6644, pp. 756–758, 1997.

[24] T. Guo, P. Nikolaev, A. Thess, D. Colbert, and R. Smalley, "Catalytic growth of single-walled manotubes by laser vaporization," *Chem. Phys. Lett.*, vol. 243, no. 1-2, pp. 49–54, 1995.

[25] M. Endo, K. Takeuchi, S. Igarashi, K. Kobori, M. Shiraishi, and H. W. Kroto, "The production and structure of pyrolytic carbon nanotubes (PCNTs)," *J. Phys. Chem. Solids*, vol. 54, no. 12, pp. 1841 – 1848, 1993.

[26] M. L. Terranova, V. Sessa, and M. Rossi, "The world of carbon nanotubes: An overview of CVD growth methodologies," *Chem. Vapor Depos.*, vol. 12, no. 6, pp. 315–325, 2006.

[27] A. Thess, R. Lee, P. Nikolaev, H. Dai, P. Petit, J. Robert, C. Xu, Y. H. Lee, S. G. Kim, A. G. Rinzler, D. T. Colbert, G. E. Scuseria, D. Tománek, J. E. Fischer, and R. E. Smalley, "Crystalline Ropes of Metallic Carbon Nanotubes," *Science*, vol. 273, no. 5274, pp. 483–487, 1996.

[28] H. Kataura, Y. Kumazawa, Y. Maniwa, Y. Ohtsuka, R. Sen, S. Suzuki, and Y. Achiba, "Diameter control of single-walled carbon nanotubes," *Carbon*, vol. 38, no. 11-12, pp. 1691–1697, 2000.

[29] S. M. Bachilo, L. Balzano, J. E. Herrera, F. Pompeo, D. E. Resasco, and R. B. Weisman, "Narrow (n,m)-distribution of single-walled carbon nanotubes grown using a solid supported catalyst," *J. Am. Chem. Soc.*, vol. 125, no. 37, pp. 11186–11187, 2003.

[30] C. L. Cheung, A. Kurtz, H. Park, and C. M. Lieber, "Diameter-controlled synthesis of carbon nanotubes," *J. Phys. Chem. B*, vol. 106, no. 10, pp. 2429–2433, 2002.

[31] S. Ghosh, S. M. Bachilo, and R. B. Weisman, "Advanced sorting of single-walled carbon nanotubes by nonlinear density-gradient ultracentrifugation," *Nat. Nanotechnol.*, vol. 5, no. 6, pp. 443–450, 2010.

[32] A. R. Harutyunyan, G. Chen, T. M. Paronyan, E. M. Pigos, O. A. Kuznetsov, K. Hewaparakrama, S. M. Kim, D. Zakharov, E. A. Stach, and G. U. Sumanasekera, "Preferential growth of single-walled carbon nanotubes with metallic conductivity," *Science*, vol. 326, no. 5949, pp. 116–120, 2009.

[33] "Hydrogen program goal-setting methodologies report to congress." DOE report, 2006.

[34] G. Sandrock, "A panoramic overview of hydrogen storage alloys from a gas reaction point of view," *J. Alloys Compd*, vol. 293–295, pp. 877–888, 1999.

[35] F. Schüth, B. Bogdanovic, and M. Felderhoff, "Light metal hydrides and complex hydrides for hydrogen storage," *Chem. Commun.*, no. 20, pp. 2249–2258, 2004.

[36] J. L. C. Rowsell and O. M. Yaghi, "Effects of functionalization, catenation, and variation of the metal oxide and organic linking units on the low-pressure hydrogen adsorption properties of metalorganic frameworks," *J. Am. Chem. Soc.*, vol. 128, no. 4, pp. 1304–1315, 2006. PMID: 16433549.

[37] A. K. Singh, A. Sadrzadeh, and B. I. Yakobson, "Metallacarboranes: Toward promising hydrogen storage metal organic frameworks," *J. Am. Chem. Soc.*, vol. 132, no. 40, pp. 14126–14129, 2010.

[38] A. C. Dillon, K. M. Jones, T. A. Bekkedahl, C. H. Kiang, D. S. Bethune, and M. J. Heben, "Storage of hydrogen in single-walled carbon nanotubes," *Nature*, vol. 386, pp. 377–379, 1997.

[39] C. Liu, Y. Y. Fan, M. Liu, H. T. Cong, H. M. Cheng, and M. S. Dresselhaus,

"Nanotubes at room temperature hydrogen storage in single-walled carbon," *Science*, vol. 286, pp. 1127–1129, 1999.

[40] W. C. Conner, G. M. Pajonk, and S. J. Teichner, *Spillover of Sorbed Species*, vol. 34. Orlando, FL: Academic Press, 1986.

[41] K. Kusada, M. Yamauchi, H. Kobayashi, H. Kitagawa, and Y. Kubota, "Hydrogen-storage properties of solid-solution alloys of immiscible neighboring elements with Pd," *J. Am. Chem. Soc.*, vol. 132, no. 45, pp. 15896–15898, 2010.

[42] A. K. Singh, E. S. Penev, and B. I. Yakobson, "Vacancy clusters in graphane as quantum dots," *ACS Nano*, vol. 4, pp. 3510–3514, 2010.

[43] T. Jacob and W. A. Goddard, III, "Adsorption of atomic H and O on the (111) surface of Pt_3Ni alloys," *J. Phys. Chem. B*, vol. 108, pp. 8311–8323, 2004.

[44] S. K. Singh and Q. Xu, "Bimetallic Ni-Pt nanocatalysts for selective decomposition of hydrazine in aqueous solution to hydrogen at room temperature for chemical hydrogen storage," *Inorg. Chem.*, vol. 49, pp. 6148–6152, 2010.

[45] J. O. Sofo, A. S. Chaudhari, and G. D. Barber, "Graphane: A two-dimensional hydrocarbon," *Phys. Rev. B*, vol. 75, p. 153401, 2007.

[46] A. K. Singh and B. I. Yakobson, "Electronics and magnetism of patterned graphene nanoroads," *Nano Lett.*, vol. 9, pp. 1540–1543, 2009.

[47] J. C. Charlier, X. Gonze, and J. P. Michenaud, "First-principles study of graphite monofluoride $(CF)_n$," *Phys. Rev. B*, vol. 47, pp. 16162–16168, 1993.

[48] D. J. Nelson and C. N. Brammer, "Toward consistent terminology for cyclohexane conformers in introductory organic chemistry," *J. Chem. Edu.*, vol. 88, no. 3, pp. 292–294, 2010.

[49] E. Schrödinger, "An undulatory theory of the mechanics of atoms and molecules," *Phys. Rev.*, vol. 28, no. 6, p. 1049, 1926.

[50] M. Springborg, *Methods of Electronic-Structure Calculations.* Wiley Series in Theoretical Chemistry, England: Wiley, 2000.

[51] W. Kohn, "Nobel lecture: Electronic structure of matter-wave functions and density functionals," *Rev. Mod. Phys.*, vol. 71, no. 5, pp. 1253–1266, 1999.

[52] P. Hohenberg and W. Kohn, "Inhomogeneous electron gas," *Phys. Rev.*, vol. 136, pp. B864–B871, 1964.

[53] R. G. Parr and W. Yang, *Density-Functional Theory of Atoms and Molecules.* New York: Oxford University Press, 1989.

[54] W. Kohn and L. J. Sham, "Self-consistent equations including exchange and correlation effects," *Phys. Rev.*, vol. 140, pp. A1133–A1138, 1965.

[55] J. P. Perdew, K. Burke, and M. Ernzerhof, "Generalized gradient approximation made simple," *Phys. Rev. Lett.*, vol. 77, no. 18, pp. 3865–3868, 1996.

[56] J. P. Perdew, K. Burke, and Y. Wang, "Generalized gradient approximation for the exchange-correlation hole of a many-electron system," *Phys. Rev. B*, vol. 54, no. 23, pp. 16533–16539, 1996.

[57] F. Bloch, "Über die quantenmechanik der elektronen in kristallgittern," *Zeitschrift für Physik A Hadrons and Nuclei*, vol. 52, no. 7, pp. 555–600, 1929.

[58] C. Herring, "A new method for calculating wave functions in crystals," *Phys. Rev.*, vol. 57, no. 12, pp. 1169–1177, 1940.

[59] J. C. Phillips and L. Kleinman, "New method for calculating wave functions in crystals and molecules," *Phys. Rev.*, vol. 116, no. 2, pp. 287–294, 1959.

[60] D. Vanderbilt, "Soft self-consistent pseudopotentials in a generalized eigenvalue formalism," *Phys. Rev. B*, vol. 41, no. 11, pp. 7892–7895, 1990.

[61] P. E. Blöchl, "Projector augmented-wave method," *Phys. Rev. B*, vol. 50, no. 24, pp. 17953–17979, 1994.

[62] J. C. Slater, "Atomic shielding constants," *Phys. Rev.*, vol. 36, no. 1, pp. 57–64, 1930.

[63] J. C. Slater and G. F. Koster, "Simplified LCAO method for the periodic potential problem," *Phys. Rev.*, vol. 94, no. 6, pp. 1498–1524, 1954.

[64] D. A. Papaconstantopoulos and M. J. Mehl, "The Slater–Koster tight-binding method: A computationally efficient and accurate approach," *J. Phys.: Condens. Matter*, vol. 15, pp. R413—R440, 2003.

[65] G. Seifert, "Tight-binding density functional theory: An approximate Kohn-Sham DFT scheme," *J. Phys. Chem. A*, vol. 111, pp. 5609–5613, 2007.

[66] D. Frenkel and B. Smit, *Understanding Molecular Simulation: From algorithms to applications.* San Diego: Academic Press, 1996.

[67] L. Verlet, "Computer "experiments" on classical fluids. I. Thermodynamical properties of Lennard-Jones molecules," *Phys. Rev.*, vol. 159, no. 1, pp. 98–103, 1967.

[68] T. J. H. Vlugt, K. Malek, and B. Smit, *Computational Methods in Catalysis and Materials Science*, ch. Molecular Simulation Techniques Using Classical Force Fields, pp. 123–149. Wiley-VCH, 2009.

[69] P. M. Morse, "Diatomic molecules according to the wave mechanics. II. Vibrational levels," *Phys. Rev.*, vol. 34, no. 1, pp. 57–64, 1929.

[70] J. E. Jones, "On the determination of molecular fields. II. From the equation of state of a gas," *Proc. R. Soc. Lon. Ser.-A*, vol. 106, no. 738, pp. 463–477, 1924.

[71] A. Martinez-Limia, J. Zhao, and P. Balbuena, "Molecular dynamics study of the initial stages of catalyzed single-wall carbon nanotubes growth: Force field development," *J. Mol. Model.*, vol. 13, no. 5, pp. 595–600, 2007.

[72] Y. Yamaguchi and S. Maruyama, "A molecular dynamics study on the formation of metallofullerene," *Eur. Phys. J. D*, vol. 9, pp. 385—388, 1999.

[73] A. P. Sutton and J. Chen, "Long-range Finnis-Sinclair potentials," *Phil. Mag. Lett.*, vol. 61, pp. 139–146, 1990.

[74] D. W. Brenner, O. A. Shenderova, J. A. Harrison, S. J. Stuart, B. Ni, and S. B. Sinnott, "A second-generation reactive empirical bond order (REBO) potential energy expression for hydrocarbons," *J. Phys. Condens. Matter.*, vol. 14, pp. 783—802, 2002.

[75] J. Zhao, A. Martinez-Limia, and P. B. Balbuena, "Understanding catalysed growth of single-wall carbon nanotubes," *Nanotechnology*, vol. 16, no. 7, p. S575, 2005.

[76] P. B. Balbuena, J. Zhao, S. Huang, Y. Wang, N. Sakulchaicharoen, and D. E. Resasco, "Role of the catalyst in the growth of single-wall carbon nanotubes," *J. Nanosci. Nanotechnol.*, vol. 6, no. 5, pp. 1247–1258, 2006.

[77] G. W. Crabtree, M. S. Dresselhaus, and M. V. Buchanan, "The hydrogen economy," *Phys. Today*, vol. 57, no. 12, pp. 39–44, 2004.

[78] L. Schlapbach and A. Züttel, "Hydrogen-storage materials for mobile applications," *Nature*, vol. 414, no. 353–358, 2001.

[79] F. Ding, Y. Lin, P. O. Krasnov, and B. I. Yakobson, "Nanotube-derived carbon foam for hydrogen sorption," *J. Chem. Phys.*, vol. 127, pp. 164703–1–164703–6, 2007.

[80] Y. Ye, C. C. Ahn, C. Witham, B. Fultza, J. Liu, A. G. Rinzler, D. Colbert, K. A. Smith, and R. E. Smalley, "Hydrogen adsorption and cohesive energy of single-walled carbon nanotubes," *Appl. Phys. Lett.*, vol. 74, pp. 2307–2309, 1999.

[81] M. Yoon, S. Yang, E. Wang, and Z. Zhang, "Charged fullerenes as high-capacity hydrogen storage media," *Nano Lett.*, vol. 7, pp. 2578–2583, 2007.

[82] O. V. Pupysheva, A. A. Farajian, and B. I. Yakobson, "Fullerene nanocage capacity for hydrogen storage," *Nano Lett.*, vol. 8, pp. 767–774, 2008.

[83] B. Kiran, A. K. Kandalam, and P. Jena, "Hydrogen storage and the 18-electron rule," *J. Chem. Phys.*, vol. 124, pp. 224703–1– 224703–6, 2006.

[84] E. Durgun, Y.-R. Jang, and S. Ciraci, "Hydrogen storage capacity of Ti-doped boron-nitride and B/Be-substituted carbon nanotubes," *Phys Rev. B*, vol. 76,

pp. 073413–1–073413–4, 2007.

[85] Y. Zhao, Y.-H. Kim, A. C. Dillon, M. J. Heben, and S. B. Zhang, "Hydrogen storage in novel organometallic buckyballs," *Phys. Rev. Lett.*, vol. 94, pp. 155504–1—155504–4, 2005.

[86] A. B. Phillips and B. S. Shivaram, "High capacity hydrogen absorption in transition metal-ethylene complexes observed via nanogravimetry," *Phys. Rev. Lett.*, vol. 100, pp. 105505–1—105505–4, 2008.

[87] T. Yildirim, J. Íñiguez, and S. Ciraci, "Molecular and dissociative adsorption of multiple hydrogen molecules on transition metal decorated C_{60}," *Phys Rev. B*, vol. 72, pp. 153403–1–153403–4, 2005.

[88] T. Yildirim and S. Ciraci, "Titanium-decorated carbon nanotubes as a potential high-capacity hydrogen storage medium," *Phys. Rev. Lett.*, vol. 94, pp. 175501–1–175501–4, 2005.

[89] G. J. Kubas, "Molecular hydrogen complexes: Coordination of a CT bond to transition metals," *Acc. Chem. Res.*, vol. 21, pp. 120–128, 1988.

[90] Q. Sun, Q. Wang, P. Jena, and Y. Kawazoe, "Clustering of Ti on a C_{60} surface and its effect on hydrogen storage," *J. Am. Chem. Soc.*, vol. 127, pp. 14582–14583, 2005.

[91] P. O. Krasnov, F. Ding, A. K. Singh, and B. I. Yakobson, "Clustering of Sc on SWNT and reduction of hydrogen uptake: Ab-initio all-electron calculations," *J. Phys. Chem. C*, vol. 111, pp. 17977–17980, 2007.

[92] A. D. Lueking and R. T. Yang, "Hydrogen spillover to enhance hydrogen storage study of the effect of carbon physicochemical properties," *Appl. Catal. A*, vol. 265, pp. 259–268, 2004.

[93] Y. Li and R. T. Yang, "Significantly enhanced hydrogen storage in metal-organic frameworks via spillover," *J. Am. Chem. Soc.*, vol. 128, pp. 726–727, 2005.

[94] R. Zacharia, K. Y. Kim, A. K. M. F. Kibria, and K. S. Nahm, "Enhancement of hydrogen storage capacity of carbon nanotubes via spill-over from vanadium and palladium nanoparticles," *Chem. Phys. Lett.*, vol. 412, pp. 369–375, 2005.

[95] B.-J. Kim, Y.-S. Lee, and S.-J. Park, "Preparation of platinum-decorated porous graphite nanofibers, and their hydrogen storage behaviors," *J. Colloid Interf. Sci.*, vol. 318, pp. 530–533, 2008.

[96] Y.-Y. Liu, J.-L. Zeng, J. Zhang, F. Xu, and L.-X. Sun, "Improved hydrogen storage in the modified metal-organic frameworks by hydrogen spillover effect," *Int. J. Hydrogen Energ.*, vol. 32, pp. 4005–4010, 2007.

[97] J. Lachawiec, A. J., G. Qi, and R. T. Yang, "Hydrogen storage in nanostructured carbons by spillover: Bridge-building enhancement," *Langmuir*, vol. 21, pp. 11418–11424, 2005.

[98] Y. Li and R. T. Yang, "Hydrogen storage in metal-organic frameworks by bridged hydrogen spillover," *J. Am. Chem. Soc.*, vol. 128, pp. 8136–8137, 2006.

[99] A. D. Lueking, H. R. Gutierrez, D. A. Fonseca, D. L. Narayanan, D. Van Essendelft, P. Jain, and C. E. B. Clifford, "Combined hydrogen production and

storage with subsequent carbon crystallization," *J. Am. Chem. Soc.*, vol. 128, pp. 7758–7760, 2006.

[100] Y. Lin, F. Ding, and B. I. Yakobson, "Hydrogen storage by spillover on graphene as a phase nucleation process," *Phys. Rev. B*, vol. 78, p. 041402, 2008.

[101] D. Stojkovic, P. Zhang, P. Lammert, and V. Crespi, "Collective stabilization of hydrogen chemisorption on graphenic surfaces," *Phys. Rev. B*, vol. 68, pp. 195406–1–195406–5, 2003.

[102] C. Zhou, J. Wu, A. Nie, R. C. Forrey, A. Tachibana, and H. Cheng, "On the sequential hydrogen dissociative chemisorption on small platinum clusters: A density functional theory study," *J. Phys. Chem. C*, vol. 111, pp. 12773–12778, 2007.

[103] L. Chen, A. C. Cooper, G. P. Pez, and H. Cheng, "Density functional study of sequential H_2 dissociative chemisorption on a Pt_6 cluster," *J. Phys. Chem. C*, vol. 111, pp. 5514–5519, 2007.

[104] G. Kresse and D. Joubert, "From ultrasoft pseudopotentials to the projector augmented-wave method," *Phys. Rev. B*, vol. 59, no. 3, pp. 1758–1775, 1999.

[105] G. Kresse and J. Furthmüller, "Efficient iterative schemes for ab initio total-energy calculations using a plane-wave basis set," *Phys. Rev. B*, vol. 54, pp. 11169–11186, 1996.

[106] G. Kresse and J. Forthmuller, "Efficiency of ab-initio total energy calculations for metals and semiconductors using a plane-wave basis set," *Comput. Mater. Sci.*, vol. 6, pp. 15 –50, 1996.

[107] G. Kresse and J. Hafner, "Ab initio molecular dynamics for liquid metals," *Phys. Rev. B*, vol. 47, pp. 558—561, 1993.

[108] H. Jónsson, G. Mills, and K. W. Jacobsen, *Nudged Elastic Band Method for Finding Minimum Energy Paths of Transitions*, p. 385. River Edge, NJ: World Scientific, 1998.

[109] J. Moc, D. G. Musaev, and K. Morokuma, "Adsorption of multiple H_2 molecules on Pd_3 and Pd_4 clusters. A density functional study," *J. Phys. Chem. A*, vol. 104, pp. 11606–11614, 2000.

[110] X. Sha, M. T. Knippenberg, A. C. Cooper, G. P. Pez, and H. Cheng, "Dynamics of hydrogen spillover on carbon-based materials," *J. Phys. Chem. C*, vol. 112, pp. 17465–17470, 2008.

[111] S. Glasstone, K. J. Laidler, and H. Eyring, *The Theory of Rate Processes.* New York: McGraw-Hill Book Co, 1941.

[112] D. Li, M. B. Muller, S. Gilje, R. B. Kaner, and G. G. Wallace, "Processable aqueous dispersions of graphene nanosheets," *Nat. Nanotechnol.*, vol. 3, pp. 101–105, 2008.

[113] S. Gilje, S. Han, M. Wang, K. L. Wang, and R. B. Kaner, "A chemical route to graphene for device applications," *Nano Lett.*, vol. 7, pp. 339–3398, 2007.

[114] M. Y. Han, B. Ozyilmaz, Y. Zhang, and P. Kim, "Energy band-gap engineering of graphene nanoribbons," *Phys. Rev. Lett.*, vol. 98, p. 206805, 2007.

[115] Z. Chen, Y. M. Lin, M. J. Rooks, and P. Avouris, "Graphene nano-ribbon electronics," *Physica E*, vol. 40, pp. 228–232, 2007.

[116] L. Ci, Z. Xu, L. Wang, W. Gao, F. Ding, K. Kelly, B. I. Yakobson, and P. M. Ajayan, "Controlled nanocutting of graphene," *Nano Res.*, vol. 1, pp. 116–122, 2008.

[117] L. G. Cançado, M. A. Pimenta, B. R. A. Neves, G. Medeiros-Ribeiro, T. Enoki, Y. Kobayashi, K. Takai, K. I. Fukui, M. S. Dresselhaus, R. Saito, and A. Jorio, "Anisotropy of the Raman spectra of nanographite ribbons," *Phys. Rev. Lett.*, vol. 93, p. 047403, 2004.

[118] Y. W. Son, M. L. Cohen, and S. G. Louie, "Energy gaps in graphene nanoribbons," *Phys. Rev. Lett.*, vol. 97, p. 216803, 2006.

[119] M. Ezawa, "Peculiar width dependence of the electronic properties of carbon nanoribbons," *Phys. Rev. B*, vol. 73, p. 045432, 2006.

[120] M. Ezawa, "Metallic graphene nanodisks: Electronic and magnetic properties," *Phys. Rev. B*, vol. 76, p. 245415, 2007.

[121] M. Ezawa, "Graphene nanoribbon and graphene nanodisk," *Physica E*, vol. 40, pp. 1421–1423, 2008.

[122] S. S. Datta, D. R. Strachan, S. M. Khamis, and A. T. C. Johnson, "Crystallographic etching of few-layer graphene," *Nano Lett.*, vol. 8, pp. 1912–1915, 2008.

[123] J. Campos-Delgado, J. M. Romo-Herrera, X. Jia, D. A. Cullen, H. Muramatsu, Y. A. Kim, T. Hayashi, Z. Ren, D. J. Smith, Y. Okuno, T. Ohba, H. Kanoh, K. Kaneko, M. Endo, H. Terrones, M. S. Dresselhaus, and M. Terrones, "Bulk production of a new form of sp^2 carbon: crystalline graphene nanoribbons," *Nano Lett.*, vol. 8, no. 9, pp. 2773–2778, 2008.

[124] D. V. Kosynkin, A. L. Higginbotham, A. Sinitskii, J. R. Lomeda, A. Dimiev, B. K. Price, and J. M. Tour, "Longitudinal unzipping of carbon nanotubes to form graphene nanoribbons," *Nature*, vol. 458, pp. 872–876, 2009.

[125] L. Jiao, L. Zhang, X. Wang, G. Diankov, and H. Dai, "Narrow graphene nanoribbons from carbon nanotubes," *Nature*, vol. 458, pp. 877–880, 2009.

[126] J. Cai, P. Ruffieux, R. Jaafar, M. Bieri, T. Braun, S. Blankenburg, M. Muoth, A. P. Seitsonen, M. Saleh, X. Feng, K. Mullen, and R. Fasel, "Atomically precise bottom-up fabrication of graphene nanoribbons," *Nature*, vol. 466, no. 7305, pp. 470–473, 2010.

[127] M. H. F. Sluiter and Y. Kawazoe, "Cluster expansion method for adsorption: Application to hydrogen chemisorption on graphene," *Phys. Rev. B*, vol. 68, p. 085410, 2003.

[128] R. Balog, B. Jorgensen, L. Nilsson, M. Andersen, E. Rienks, M. Bianchi, M. Fanetti, E. Laegsgaard, A. Baraldi, S. Lizzit, Z. Sljivancanin, F. Besenbacher, B. Hammer, T. G. Pedersen, P. Hofmann, and L. Hornekaer, "Bandgap opening in graphene induced by patterned hydrogen adsorption," *Nat. Mater.*, vol. 9, no. 4, pp. 315–319, 2010.

[129] D. C. Elias, R. R. Nair, T. M. G. Mohiuddin, S. V. Morozov, P. Blake, M. P. Halsall, A. C. Ferrari, D. W. Boukhvalov, M. I. Katsnelson, A. K. Geim, and K. S. Novoselov, "Control of graphene's properties by reversible hydrogenation: Evidence for graphane," *Science*, vol. 323, no. 5914, pp. 610–613, 2009.

[130] S. Ryu, M. Y. Han, J. Maultzsch, T. F. Heinz, P. Kim, M. L. Steigerwald, and L. E. Brus, "Reversible basal plane hydrogenation of graphene," *Nano Lett.*,

vol. 8, pp. 4597–4602, 2008.

[131] L. B. Ebert, J. I. Brauman, and R. A. Huggins, "Carbon monofluoride. evidence for a structure containing an infinite array of cyclohexane boats," *J. Am. Chem. Soc.*, vol. 96, pp. 7841–7842, 1974.

[132] Y. Kita, N. Watanabe, and Y. Fujii, "Chemical composition and crystal structure of graphite fluoride," *J. Am. Chem. Soc.*, vol. 101, pp. 3832–3841, 1979.

[133] T. Mallouk and N. Bartlett, "Reversible intercalation of graphite by fluorine: A new bifluoride, $C_{12}HF_2$, and graphite fluorides, CF ($5> x >2$)," *J. Chem. Soc., Chem. Commun.*, pp. 103–105, 1983.

[134] T. Nakajima, N. Watanabe, I. Kameda, and M. Endo, "Preparation and electrical conductivity of fluorine-graphite fiber intercalation compound," *Carbon*, vol. 24, pp. 343–351, 1986.

[135] A. M. Panich, "Nuclear magnetic resonance study of fluorine–graphite intercalation compounds and graphite fluorides," *Synthetic Met.*, vol. 100, pp. 169–185, 1999.

[136] H. Touhara, K. Kadono, Y. Fujii, and N. Watanabe, "On the structure of graphite fluoride," *Z. Anorg. Allg. Chem.*, vol. 544, pp. 7–20, 1987.

[137] N. Watanabe, "Characteristics and applications of graphite fluoride," *Physica B & C*, vol. 105, pp. 17–21, 1981.

[138] W. Rüdorff and G. Rüdorff, "Zur konstitution des kohlenstoff-monofluorids," *Z. Anorg. Chem.*, vol. 253, pp. 281–296, 1947.

[139] R. J. Lagow, R. B. Badachhape, J. L. Wood, and J. L. Margrave, "Some new synthetic approaches to graphite–fluorine chemistry," *J. Chem. Soc., Dalton Trans.*, no. 1268–1273, 1974.

[140] V. K. Mahajan, R. B. Badachhape, and J. L. Margrave, "X-ray powder diffraction study of poly(carbon monofluoride), $CF_{1.12}$," *Inorg. Nucl. Chem. Lett.*, vol. 10, pp. 1103–1109, 1974.

[141] T. Nakajima, *Fluorine–Carbon and Fluoride–Carbon Materials: Chemistry, Physics, and Applications*, ch. Synthesis, structure, and physicochemical properties of fluorine-graphite intercalation compounds. New York: Marcel Dekker, 1995.

[142] M. S. Dresselhaus, M. Endo, and J. P. Issi, *Fluorine–Carbon and Fluoride–Carbon Materials: Chemistry, Physics, and Applications*, ch. Physical properties of fluorine- and fluoride-graphite intercalation compounds. New York: Marcel Dekker, 1995.

[143] K. N. Kudin, G. E. Scuseria, and B. I. Yakobson, "C_2F, BN, and C nanoshell elasticity from ab initio computations," *Phys. Rev. B*, vol. 64, p. 235406, 2001.

[144] E. T. Mickelson, C. B. Huffman, A. G. Rinzler, R. E. Smalley, R. H. Hauge, and J. L. Margrave, "Fluorination of single-wall carbon nanotubes," *Chem. Phys. Lett.*, vol. 296, pp. 188–194, 1998.

[145] S. Osuna, M. Torrent-Sucarrat, M. Sola, P. Geerlings, C. P. Ewels, and G. V. Lier, "Reaction mechanisms for graphene and carbon nanotube fluorination," *J. Phys. Chem. C*, vol. 114, pp. 3340–3345, 2010.

[146] J. L. Bahr and J. M. Tour, "Covalent chemistry of single-wall carbon nanotubes," *J. Mater. Chem.*, vol. 12, pp. 1952–1958, 2002.

[147] Y. P. Sun, K. Fu, Y. Lin, and W. Huang, "Functionalized carbon nanotubes: Properties and applications," *Acc. Chem. Res.*, vol. 35, pp. 1096–1104, 2002.

[148] K. N. Kudin, H. F. Bettinger, and G. E. Scuseria, "Fluorinated single-wall carbon nanotubes," *Phys. Rev. B*, vol. 63, p. 045413, 2001.

[149] S. H. Cheng, K. Zou, F. Okino, H. R. Gutierrez, A. Gupta, N. Shen, P. C. Eklund, J. O. Sofo, and J. Zhu, "Reversible fluorination of graphene: Evidence of a two-dimensional wide bandgap semiconductor," *Phys. Rev. B*, vol. 81, p. 205435, 2010.

[150] J. T. Robinson, J. S. Burgess, C. E. Junkermeier, S. C. Badescu, T. L. Reinecke, F. K. Perkins, M. K. Zalalutdniov, J. W. Baldwin, J. C. Culbertson, P. E. Sheehan, and E. S. Snow, "Properties of fluorinated graphene films," *Nano Lett.*, vol. 10, pp. 3001–3005, 2010.

[151] C. Köhler and T. Frauenheim, "Molecular dynamics simulations of CF_x (x = 2, 3) molecules at Si_3N_4 and SiO_2 surfaces," *Surf. Sci.*, vol. 600, pp. 453–460, 2006.

[152] B. Aradi, B. Hourahine, and T. Frauenheim, "DFTB$^+$, a sparse matrix-based implementation of the DFTB method.," *J. Phys. Chem. A*, vol. 111, pp. 5678–5684, 2007.

[153] S. Purser, P. R. Moore, S. Swallow, and V. Gouverneur, "Fluorine in medicinal chemistry," *Chem. Soc. Rev.*, vol. 37, pp. 320–330, 2008.

[154] D. O'Hagan, "Understanding organofluorine chemistry. An introduction to the C–F bond," *Chem. Soc. Rev.*, vol. 37, pp. 308–319, 2008.

[155] D. M. Lemal, "Perspective on fluorocarbon chemistry," *J. Org. Chem.*, vol. 69, pp. 1—11, 2004.

[156] L. A. Artyukhov, V. I.; Chernozatonskii, "Structure and layer interaction in carbon monofluoride and graphane: A comparative computational study," *J. Phys. Chem. A*, vol. 114, pp. 5389–5396, 2010.

[157] M. J. S. Dewar and R. C. Dougherty, *The PMO Theory of Organic Chemistry.* New York: Plenum, 1975.

[158] K. N. Kudin, "Zigzag graphene nanoribbons with saturated edges," *ACS Nano*, vol. 2, pp. 516–522, 2008.

[159] P. B. Chernozatonskii, L. A.; Sorokin, "Nanoengineering structures on graphene with adsorbed hydrogen "lines"," *J. Phys. Chem. C*, vol. 114, pp. 3225–3229, 2010.

[160] B. Trauzettel, D. V. Bulaev, D. Loss, and G. Burkard, "Spin qubits in graphene quantum dots," *Nat. Phys.*, vol. 3, pp. 192–196, 2007.

[161] P. Recher and B. Trauzettel, "Quantum dots and spin qubits in graphene," *Nanotechnology*, vol. 21, p. 302001, 2010.

[162] L. A. Ponomarenko, F. Schedin, M. I. Katsnelson, R. Yang, E. W. Hill, K. S. Novoselov, and A. K. Geim, "Chaotic dirac billiard in graphene quantum dots," *Science*, vol. 320, no. 5874, pp. 356–358, 2008.

[163] A. Matulis and F. M. Peeters, "Quasibound states of quantum dots in single and bilayer graphene," *Phys. Rev. B*, vol. 77, p. 115423, 2008.

[164] S. Lebegue, M. Klintenberg, O. Eriksson, and M. I. Katsnelson, "Accurate electronic band gap of pure and functionalized graphane from GW calculations," *Phys. Rev. B*, vol. 79, p. 245117, 2009.

[165] P. M. Ajayan and B. I. Yakobson, "Material science: Oxygen breaks into carbon world," *Nature*, vol. 441, pp. 818–819, 2006.

[166] M. Z. S. Flores, P. A. S. Autreto, S. B. Legoas, and D. S. Galvao, "Graphene to graphane: A theoretical study," *Nanotechnology*, vol. 20, p. 465704, 2009.

[167] R. R. Nair, W. Ren, R. Jalil, I. Riaz, V. G. Kravets, L. Britnell, P. Blake, F. Schedin, A. S. Mayorov, S. Yuan, M. I. Katsnelson, H.-M. Cheng, W. Strupinski, L. G. Bulusheva, A. V. Okotrub, I. V. Grigorieva, A. N. Grigorenko, K. S. Novoselov, and A. K. Geim, "Fluorographene: A two-dimensional counterpart of teflon," *Small*, vol. 6, no. 24, pp. 2877–2884, 2010.

[168] L. X. Zheng, M. J. O'Connell, S. K. Doorn, X. Z. Liao, Y. H. Zhao, E. A. Akhadov, M. A. Hoffbauer, B. J. Roop, Q. X. Jia, R. C. Dye, D. E. Peterson, S. M. Huang, J. Liu, and Y. T. Zhu, "Ultralong single-wall carbon nanotubes," *Nat. Mater.*, vol. 3, no. 10, pp. 673–676, 2004.

[169] Z. Yang, X. Chen, H. Nie, K. Zhang, W. Li, B. Yi, and L. Xu, "Direct synthesis of ultralong carbon nanotube bundles by spray pyrolysis and investigation of growth mechanism," *Nanotechnology*, vol. 19, no. 8, p. 085606, 2008.

[170] M. Cantoro, S. Hofmann, S. Pisana, V. Scardaci, A. Parvez, C. Ducati, A. C. Ferrari, A. M. Blackburn, K.-Y. Wang, and J. Robertson, "Catalytic chemical

vapor deposition of single-wall carbon nanotubes at low temperatures," *Nano Letters*, vol. 6, no. 6, pp. 1107–1112, 2006.

[171] E. J. Bae, Y.-S. Min, D. Kang, J.-H. Ko, and W. Park, "Low-temperature growth of single-walled carbon nanotubes by plasma enhanced chemical vapor deposition," *Chem. Mater.*, vol. 17, no. 20, pp. 5141–5145, 2005.

[172] H. Liao and J. H. Hafner, "Low-temperature single-wall carbon nanotube synthesis by thermal chemical vapor deposition," *J. Phys. Chem. B*, vol. 108, no. 22, pp. 6941–6943, 2004.

[173] S. Maruyama, R. Kojima, Y. Miyauchi, S. Chiashi, and M. Kohno, "Low-temperature synthesis of high-purity single-walled carbon nanotubes from alcohol," *Chem. Phys. Lett.*, vol. 360, no. 3-4, pp. 229–234, 2002.

[174] S. Helveg, C. López-Cartes, J. Sehested, P. L. Hansen, B. S. Clausen, J. R. Rostrup-Nielsen, F. Abild-Pedersen, and J. K. Nørskov, "Atomic-scale imaging of carbon nanofibre growth," *Nature*, vol. 427, no. 6973, pp. 426–429, 2004.

[175] J. A. Rodríguez-Manzo, M. Terrones, H. Terrones, H. W. Kroto, L. Sun, and F. Banhart, "In situ nucleation of carbon nanotubes by the injection of carbon atoms into metal particles," *Nat. Nanotechnol.*, vol. 2, no. 5, pp. 307–311, 2007.

[176] H. Yoshida, S. Takeda, T. Uchiyama, H. Kohno, and Y. Homma, "Atomic-scale in-situ observation of carbon nanotube growth from solid state iron carbide nanoparticles," *Nano Lett.*, vol. 8, no. 7, pp. 2082–2086, 2008.

[177] Y. Shibuta and S. Maruyama, "Molecular dynamics simulation of formation process of single-walled carbon nanotubes by CCVD method," *Chem. Phys. Lett.*, vol. 382, no. 3-4, pp. 381–386, 2003.

[178] F. Ding, K. Bolton, and A. Rosén, "Nucleation and growth of single-walled carbon nanotubes: A molecular dynamics study," *J. Phys. Chem. B*, vol. 108, no. 45, pp. 17369–17377, 2004.

[179] F. Ding, A. R. Harutyunyan, and B. I. Yakobson, "Dislocation theory of chirality-controlled nanotube growth," *P. Natl. Acad. Sci. USA*, vol. 106, no. 8, pp. 2506–2509, 2009.

[180] J.-Y. Raty, F. Gygi, and G. Galli, "Growth of carbon nanotubes on metal nanoparticles: A microscopic mechanism from ab initio molecular dynamics simulations," *Phys. Rev. Lett.*, vol. 95, no. 9, p. 096103, 2005.

[181] X. Fan, R. Buczko, A. A. Puretzky, D. B. Geohegan, J. Y. Howe, S. T. Pantelides, and S. J. Pennycook, "Nucleation of single-walled carbon nanotubes," *Phys. Rev. Lett.*, vol. 90, no. 14, p. 145501, 2003.

[182] J. Gavillet, A. Loiseau, C. Journet, F. Willaime, F. Ducastelle, and J.-C. Charlier, "Root-growth mechanism for single-wall carbon nanotubes," *Phys. Rev. Lett.*, vol. 87, no. 27, p. 275504, 2001.

[183] Y. Ohta, Y. Okamoto, S. Irle, and K. Morokuma, "Rapid growth of a single-walled carbon nanotube on an iron cluster: Density-functional tight-binding molecular dynamics simulations," *ACS Nano*, vol. 2, no. 7, pp. 1437–1444, 2008.

[184] Y. Ohta, Y. Okamoto, S. Irle, and K. Morokuma, "Temperature dependence of iron-catalyzed continued single-walled carbon nanotube growth rates: Density functional tight-binding molecular dynamics simulations," *J. Phys. Chem. C*, vol. 113, no. 1, pp. 159–169, 2009.

[185] H. Amara, C. Bichara, and F. Ducastelle, "Formation of carbon nanostructures on nickel surfaces: A tight-binding grand canonical Monte Carlo study," *Phys. Rev. B*, vol. 73, no. 11, p. 113404, 2006.

[186] J.-C. Charlier, H. Amara, and P. Lambin, "Catalytically assisted tip growth mechanism for single-wall carbon nanotubes," *ACS Nano*, vol. 1, no. 3, pp. 202–207, 2007.

[187] F. Ding, A. Rosén, E. E. B. Campbell, L. K. L. Falk, and K. Bolton, "Graphitic encapsulation of catalyst particles in carbon nanotube production," *J. Phys. Chem. B*, vol. 110, no. 15, pp. 7666–7670, 2006.

[188] R. S. Wagner and W. C. Ellis, "Vapor-liquid-solid mechanism of single crystal growth," *Appl. Phys. Lett.*, vol. 4, no. 5, pp. 89–90, 1964.

[189] R. T. K. Baker, M. A. Barber, P. S. Harris, F. S. Feates, and R. J. Waite, "Nucleation and growth of carbon deposits from the nickel catalyzed decomposition of acetylene," *J. Catal.*, vol. 26, no. 1, pp. 51–62, 1972.

[190] Y. Saito, "Nanoparticles and filled nanocapsules," *Carbon*, vol. 33, no. 7, pp. 979–988, 1995.

[191] J. H. Hafner, M. J. Bronikowski, B. R. Azamian, P. Nikolaev, A. G. Rinzler, D. T. Colbert, K. A. Smith, and R. E. Smalley, "Catalytic growth of single-wall carbon nanotubes from metal particles," *Chem. Phys. Lett.*, vol. 296, no. 1-2, pp. 195–202, 1998.

[192] H. Kanzow and A. Ding, "Formation mechanism of single-wall carbon nanotubes on liquid-metal particles," *Phys. Rev. B*, vol. 60, no. 15, pp. 11180–11186, 1999.

[193] H. Kanzow, C. Lenski, and A. Ding, "Single-wall carbon nanotube diameter distributions calculated from experimental parameters," *Phys. Rev. B*, vol. 63, no. 12, p. 125402, 2001.

[194] W. Zhu, H. Duan, and K. Bolton, "Diameter and chirality changes of single-walled carbon nanotubes during growth: An ab-initio study," *J. Nanosci. Nanotechnol.*, vol. 9, no. 2, pp. 1222–1225, 2009.

[195] F. Ding, P. Larsson, J. A. Larsson, R. Ahuja, H. Duan, A. Rosén, and K. Bolton, "The importance of strong carbon-metal adhesion for catalytic nucleation of single-walled carbon nanotubes," *Nano Lett.*, vol. 8, no. 2, pp. 463–468, 2008.

[196] G. Bertoni, L. Calmels, A. Altibelli, and V. Serin, "First-principles calculation of the electronic structure and EELS spectra at the graphene/Ni(111) interface," *Phys. Rev. B*, vol. 71, no. 7, p. 075402, 2005.

[197] F. Ding, A. Rosén, and K. Bolton, "Dependence of SWNT growth mechanism on temperature and catalyst particle size: Bulk versus surface diffusion," *Carbon*, vol. 43, no. 10, pp. 2215–2217, 2005.

[198] F. Ding, A. Rosén, and K. Bolton, "The role of the catalytic particle temperature gradient for SWNT growth from small particles," *Chem. Phys. Lett.*, vol. 393, no. 4-6, pp. 309–313, 2004.

[199] M. Methfessel and A. T. Paxton, "High-precision sampling for Brillouin-zone integration in metals," *Phys. Rev. B*, vol. 40, no. 6, pp. 3616–3621, 1989.

[200] Y. Gamo, A. Nagashima, M. Wakabayashi, M. Terai, and C. Oshima, "Atomic structure of monolayer graphite formed on Ni(111)," *Surf. Sci.*, vol. 374, no. 1-3, pp. 61–64, 1997.

[201] H. Kawanowa, H. Ozawa, T. Yazaki, Y. Gotoh, and R. Souda, "Structure analysis of monolayer graphite on Ni(111) surface by Li^+-impact collision ion scattering spectroscopy," *Jpn. J. Appl. Phys.*, vol. 41, no. Part 1, No. 10, pp. 6149–6152, 2002.

[202] R. Rosei, M. De Crescenzi, F. Sette, C. Quaresima, A. Savoia, and P. Perfetti, "Structure of graphitic carbon on Ni(111): A surface extended-energy-loss fine-structure study," *Phys. Rev. B*, vol. 28, no. 2, pp. 1161–1164, 1983.

[203] H. Dai, A. G. Rinzler, P. Nikolaev, A. Thess, D. T. Colbert, and R. E. Smalley, "Single-wall nanotubes produced by metal-catalyzed disproportionation of carbon monoxide," *Chem. Phys. Lett.*, vol. 260, no. 3-4, pp. 471–475, 1996.

[204] D. Ciuparu, Y. Chen, S. Lim, G. L. Haller, and L. Pfefferle, "Uniform-diameter single-walled carbon nanotubes catalytically grown in cobalt-incorporated MCM-41," *J. Phys. Chem. B*, vol. 108, no. 2, pp. 503–507, 2004.

[205] M. J. Bronikowski, P. A. Willis, D. T. Colbert, K. A. Smith, and R. E. Smalley, "Gas-phase production of carbon single-walled nanotubes from carbon monoxide via the HiPco process: A parametric study," *J. Vac. Sci. Technol. A*, vol. 19, no. 4, pp. 1800–1805, 2001.

[206] V. L. Kuznetsov, A. N. Usoltseva, A. L. Chuvilin, E. D. Obraztsova, and J.-M. Bonard, "Thermodynamic analysis of nucleation of carbon deposits on metal particles and its implications for the growth of carbon nanotubes," *Phys. Rev. B*, vol. 64, no. 23, p. 235401, 2001.

[207] L. Alvarez, T. Guillard, J. L. Sauvajol, G. Flamant, and D. Laplaze, "Growth mechanisms and diameter evolution of single wall carbon nanotubes," *Chem.*

Phys. Lett., vol. 342, no. 1-2, pp. 7–14, 2001.

[208] A. R. Harutyunyan, T. Tokune, and E. Mora, "Liquid as a required catalyst phase for carbon single-walled nanotube growth," *Appl. Phys. Lett.*, vol. 87, no. 5, p. 051919, 2005.

[209] E. Mora, J. M. Pigos, F. Ding, B. I. Yakobson, and A. R. Harutyunyan, "Low-temperature single-wall carbon nanotubes synthesis: Feedstock decomposition limited growth," *J. Am. Chem. Soc.*, vol. 130, no. 36, pp. 11840–11841, 2008.

[210] S. H. Yang, W. H. Shin, J. W. Lee, S. Y. Kim, S. I. Woo, and J. K. Kang, "Interaction of a transition metal atom with intrinsic defects in single-walled carbon nanotubes," *J. Phys. Chem. B*, vol. 110, no. 28, pp. 13941–13946, 2006.

[211] E. Mora and A. R. Harutyunyan, "Study of single-walled carbon nanotubes growth via the catalyst lifetime," *J. Phys. Chem. C*, vol. 112, no. 13, pp. 4805–4812, 2008.

[212] C. A. Crouse, B. Maruyama, R. Colorado Jr., T. Back, and A. R. Barron, "Growth, new growth, and amplification of carbon nanotubes as a function of catalyst composition," *J. Am. Chem. Soc.*, vol. 130, no. 25, pp. 7946–7954, 2008.

[213] G. E. Begtrup, W. Gannett, J. C. Meyer, T. D. Yuzvinsky, E. Ertekin, J. C. Grossman, and A. Zettl, "Facets of nanotube synthesis: High-resolution transmission electron microscopy study and density functional theory calculations," *Phys. Rev. B*, vol. 79, no. 20, p. 205409, 2009.

[214] S. Hofmann, R. Sharma, C. Ducati, G. Du, C. Mattevi, C. Cepek, M. Cantoro, S. Pisana, A. Parvez, F. Cervantes-Sodi, A. C. Ferrari, R. Dunin-Borkowski,

S. Lizzit, L. Petaccia, A. Goldoni, and J. Robertson, "In situ observations of catalyst dynamics during surface-bound carbon nanotube nucleation," *Nano Letters*, vol. 7, no. 3, pp. 602–608, 2007.

[215] M. Moseler, F. Cervantes-Sodi, S. Hofmann, G. Csányi, and A. C. Ferrari, "Dynamic catalyst restructuring during carbon nanotube growth," *ACS Nano*, vol. 4, no. 12, pp. 7587–7595, 2010.

[216] A. C. T. van Duin, S. Dasgupta, F. Lorant, and W. A. Goddard, "ReaxFF: a reactive force field for hydrocarbons," *J. Phys. Chem. A*, vol. 105, no. 41, pp. 9396–9409, 2001.

[217] J. E. Mueller, A. C. T. van Duin, and W. A. Goddard, "Application of the ReaxFF reactive force field to reactive dynamics of hydrocarbon chemisorption and decomposition," *J. Phys. Chem. C*, vol. 114, no. 12, pp. 5675–5685, 2010.

[218] E. C. Neyts, Y. Shibuta, A. C. T. van Duin, and A. Bogaerts, "Catalyzed growth of carbon nanotube with definable chirality by hybrid molecular dynamics-force biased monte carlo simulations," *ACS Nano*, vol. 4, no. 11, pp. 6665–6672, 2010.

[219] S. Plimpton, "Fast parallel algorithms for short-range molecular dynamics," *J. Comput. Phys.*, vol. 117, no. 1, pp. 1 – 19, 1995.

[220] R. Ferrando, J. Jellinek, and R. L. Johnston, "Nanoalloys: From theory to applications of alloy clusters and nanoparticles," *Chem. Rev.*, vol. 108, no. 3, pp. 845–910, 2008.

[221] W.-H. Chiang and R. Mohan Sankaran, "Linking catalyst composition to chirality distributions of as-grown single-walled carbon nanotubes by tuning Ni_xFe_{1-x} nanoparticles," *Nat. Mater.*, vol. 8, no. 11, pp. 882–886, 2009.

[222] J. Jellinek and E. B. Krissinel, "Ni_nAl_m alloy clusters: Analysis of structural forms and their energy ordering," *Chem. Phys. Lett.*, vol. 258, no. 1-2, pp. 283–292, 1996.

[223] C. Song, Q. Ge, and L. Wang, "DFT studies of Pt/Au bimetallic clusters and their interactions with the co molecule," *J. Phys. Chem. B*, vol. 109, pp. 22341–22350, 2005.

[224] C. P. Deck and K. Vecchio, "Prediction of carbon nanotube growth success by the analysis of carbon-catalyst binary phase diagrams," *Carbon*, vol. 44, no. 2, pp. 267–275, 2006.

[225] W. Zhou, Z. Han, J. Wang, Y. Zhang, Z. Jin, X. Sun, Y. Zhang, C. Yan, and Y. Li, "Copper catalyzing growth of single-walled carbon nanotubes on substrates," *Nano Lett.*, vol. 6, no. 12, pp. 2987–2990, 2006.

[226] A. W. Orbaek, A. C. Owens, C. A. Crouse, and A. R. Barron. Personal communication.

[227] J. C. Charlier and S. Iijima, *Carbon Nanotubes: Synthesis, Structure, Properties and Applications*, vol. 80 of *Springer Series in Topics in Applied Physics*, ch. Growth Mechanisms. Berlin: Springer-Verlag, 2001.

[228] J. Shelton, H. Patil, and J. Blakely, "Equilibrium segregation of carbon to a nickel (111) surface: A surface phase transition," *Surf. Sci.*, vol. 43, no. 2, pp. 493–520, 1974.

[229] L. C. Isett and J. M. Blakely, "Binding of carbon atoms at a stepped-Ni surface," *J. Vac. Sci. Technol.*, vol. 12, no. 1, pp. 237–241, 1975.

[230] L. C. Isett and J. M. Blakely, "Binding energies of carbon to Ni(100) from equilibrium segregation studies," *Surf. Sci.*, vol. 47, no. 2, pp. 645–649, 1975.

[231] L. Isett and J. Blakely, "Segregation isosteres for carbon at the (100) surface of nickel," *Surf. Sci.*, vol. 58, no. 2, pp. 397–414, 1976.

[232] A. Takeuchi and H. Wise, "Thermodynamic properties of surface carbon on metals. 1. Nickel," *J. Phys. Chem.*, vol. 87, no. 26, pp. 5372–5376, 1983.

[233] O. V. Yazyev and A. Pasquarello, "Effect of metal elements in catalytic growth of carbon nanotubes," *Phys. Rev. Lett.*, vol. 100, no. 15, p. 156102, 2008.

[234] Q.-M. Zhang, J. C. Wells, X. G. Gong, and Z. Zhang, "Adsorption of a carbon atom on the ni_{38} magic cluster and three low-index nickel surfaces: A comparative first-principles study," *Phys. Rev. B*, vol. 69, no. 20, p. 205413, 2004.

[235] S.-G. Wang, X.-Y. Liao, D.-B. Cao, Y.-W. Li, J. Wang, and H. Jiao, "Formation of carbon species on Ni(111): Structure and stability," *J. Phys. Chem. C*, vol. 111, no. 29, pp. 10894–10903, 2007.

[236] Y.-H. Shin and S. Hong, "Carbon diffusion around the edge region of nickel nanoparticles," *Appl. Phys. Lett.*, vol. 92, no. 4, p. 043103, 2008.

[237] S. Hong, Y.-H. Shin, and J. Ihm, "Crystal shape of a nickel particle related to carbon nanotube growth," *Jpn. J. Appl. Phys.*, vol. 41, no. 10, pp. 6142–6144, 2002.

[238] W. T. Geng, A. J. Freeman, and R. Q. Wu, "Magnetism at high-index transition-metal surfaces and the effect of metalloid impurities: Ni(210)," *Phys. Rev. B*, vol. 63, no. 6, p. 064427, 2001.

[239] S. P. Chen, D. J. Srolovitz, and A. F. Voter, "Computer simulation on surfaces and [001] symmetric tilt grain boundaries in Ni, Al, and Ni_3Al," *J. Mater. Res.*, vol. 4, no. 1, pp. 62–77, 1989.

[240] T. S. Rahman, A. Kara, and S. Durukanoglu, "Structural relaxations, vibrational dynamics and thermodynamics of vicinal surfaces," *J. Phys.: Condens. Matter.*, vol. 15, pp. S3197–S3226, 2003.

[241] A. M. Rodríguez, G. Bozzolo, and J. Ferrante, "Multilayer relaxation and surface energies of fcc and bcc metals using equivalent crystal theory," *Surf. Sci.*, vol. 289, pp. 100–126, 1993.

[242] J. E. Demuth, P. M. Marcus, and D. W. Jepsen, "Analysis of low-energy-electron-diffraction intensity spectra for (001), (110), and (111) nickel," *Phys. Rev. B*, vol. 11, no. 4, pp. 1460–1474, 1975.

[243] J. W. M. Frenken, J. F. van der Veen, and G. Allan, "Relation between surface relaxation and surface force constants in clean and oxygen-covered Ni(001)," *Phys. Rev. Lett.*, vol. 51, no. 20, pp. 1876–1879, 1983.

[244] D. L. Adams, L. E. Petersen, and C. S. Sorensen, "Oscillatory relaxation of the Ni(110) surface: a LEED study," *J. Phys. C: Solid State Phys.*, vol. 18, no. 8, pp. 1753–1766, 1985.

[245] Y. Gauthier, R. Baudoing, Y. Joly, C. Gaubert, and J. Rundgren, "Multilayer relaxation of Ni(110) analysed by LEED and metric distances," *J. Phys. C: Solid State Phys.*, vol. 17, no. 25, pp. 4547–4558, 1984.

[246] M. L. Xu and S. Y. Tong, "Multilayer relaxation for the clean Ni(110) surface," *Phys. Rev. B*, vol. 31, no. 10, pp. 6332–6336, 1985.

[247] D. Adams, W. Moore, and K. Mitchell, "Multilayer relaxation of the Ni(311) surface: A new LEED analysis," *Surf. Sci.*, vol. 149, no. 2-3, pp. 407–422, 1985.

[248] J. Sokolov, H. Shih, U. Bardi, F. Jona, and P. Marcus, "New relaxation phenomena in the outer atomic layers of Fe{211}," *Solid State Commun.*, vol. 48, no. 9, pp. 739 – 741, 1983.

[249] P. Blónski and A. Kiejna, "Structural, electronic, and magnetic properties of bcc iron surfaces," *Surf. Sci.*, vol. 601, no. 1, pp. 123–133, 2007.

[250] J. C. Boettger, "Nonconvergence of surface energies obtained from thin-film calculations," *Phys. Rev. B*, vol. 49, no. 23, pp. 16798–16800, 1994.

[251] V. Fiorentini and M. Methfessel, "Extracting convergent surface energies from slab calculations," *J. Phys. Condens. Matter.*, vol. 8, no. 36, pp. 6525–6529, 1996.

[252] A. R. Roosen, R. P. McCormack, and W. C. Carter, "Wulffman: A tool for the calculation and display of crystal shapes," *Comput. Mater. Sci.*, vol. 11, pp. 16–26, 1998.

[253] S. Levy, T. Munzer, and M. e. a. Phillips, "Geomview: 3d visualization software."

[254] J.-S. Hong, W. Jo, K.-J. Ko, N. M. Hwang, and D.-Y. Kim, "Equilibrium shape of nickel crystal," *Philos. Mag.*, vol. 89, no. 32, pp. 2989–2999, 2009.

[255] M. Moors, H. Amara, T. Visart de Bocarmé, C. Bichara, F. Ducastelle, N. Kruse, and J.-C. Charlier, "Early stages in the nucleation process of carbon nanotubes," *ACS Nano*, vol. 3, no. 3, pp. 511–516, 2009.

[256] J. Lahiri, T. Miller, L. Adamska, I. I. Oleynik, and M. Batzill, "Graphene growth on Ni(111) by transformation of a surface carbide," *Nano Lett.*, vol. 11, no. 2, pp. 518–522, 2011.

[257] G. Kalibaeva, R. Vuilleumier, S. Meloni, A. Alavi, G. Ciccotti, and R. Rosei, "Ab initio simulation of carbon clustering on an ni(111) surface: a model of the poisoning of nickel-based catalysts," *J. Phys. Chem. B*, vol. 110, no. 8, pp. 3638–3646, 2006.

[258] C. Klink, I. Stensgaard, F. Besenbacher, and E. Lægsgaard, "Carbidic carbon on Ni(110): An STM study," *Surf. Sci.*, vol. 360, no. 1-3, pp. 171–179, 1996.

[259] F. Besenbacher, P. T. Sprunger, L. Ruan, L. Olesen, I. Stensgaard, and E. Lægsgaard, "Direct observations of changes in surface structures by scanning tunneling microscopy," *Top. Catal.*, vol. 1, no. 3-4, pp. 325–341, 1994.

[260] M. Vanin, J. J. Mortensen, A. K. Kelkkanen, J. M. Garcia-Lastra, K. S. Thygesen, and K. W. Jacobsen, "Graphene on metals: A van der Waals density functional study," *Phys. Rev. B*, vol. 81, no. 8, p. 081408, 2010.

[261] L. Wang and R. T. Yang, "Hydrogen storage properties of carbons doped with ruthenium, platinum, and nickel nanoparticles," *J. Phys. Chem. C*, vol. 112, pp. 12486–12494, 2008.

[262] E. J. Duplock, M. Scheffler, and P. J. D. Linda, "Hallmark of perfect graphene," *Phys. Rev. Lett.*, vol. 92, pp. 225502–1–225502–4, 2004.